Nonlinearities between GABAB receptor-mediated inhibition and T-type calcium channel activity bidirectionally regulate thalamic oscillations

Adam Lu
Hsinchu City, Taiwan

Bachelor of Science, Johns Hopkins University, 2011
Master of Science, Johns Hopkins University, 2011

A Dissertation presented to the Graduate Faculty
of the University of Virginia in Candidacy for the Degree of
Doctor of Philosophy

Neuroscience Graduate Program

University of Virginia
July, 2020

Abstract

Absence seizures result from 3-5 Hz generalized thalamocortical oscillations that depend on highly regulated inhibitory neurotransmission in the thalamus. Efficient reuptake of the inhibitory neurotransmitter GABA is essential, and reuptake failure worsens seizures. Here, we show that blocking GABA transporters (GATs) in acute brain slices containing key parts of the thalamocortical seizure network modulates epileptiform activity. As expected, we found that blocking either GAT1 or GAT3 prolonged oscillations. However, blocking both GATs unexpectedly suppressed oscillations. Integrating experimental observations into single-neuron and network-level computational models shows how a non-linear dependence of T-type calcium channel opening on $GABA_B$ receptor activity regulates network oscillations. Receptor activity that is either too brief or too protracted fails to sufficiently open T-type channels necessary for sustaining oscillations. Only within a narrow range does prolonging $GABA_B$ receptor activity promote channel opening and intensify oscillations. These results have implications for therapeutics that modulate GABA transporters.

Chapter 1: Introduction and Background

In this chapter, I will first explain the unmet clinical needs in the study of epilepsy, and more specifically, absence epilepsy. I then discuss the clinical features, animal models and neural correlates of absence seizures. Next, I lay out the anatomy and physiology of the thalamocortical network that is thought to generate the oscillations that underlie absence seizures. I discuss how the intra-thalamic and the thalamocortical network sustain normal or epileptiform thalamic oscillations in detail, exploring the effects of intrinsic ion channels and receptors. I then turn to computational models of thalamocortical neurons and thalamic/thalamocortical networks and how they have contributed to the understanding of the pathophysiology of absence seizures. Finally, I delineate the research goals I've set out to achieve.

Epilepsy: Definition, significance and heterogeneity

Epilepsy is a disease involving recurrent unprovoked seizures[1]. A seizure is a transient display of abnormal behavior due to excessive or hypersynchronous neural activity in the brain[2]. This hypersynchronous activity results in large amplitude spikes on human electroencephalography (EEG), which is the gold standard for a seizure diagnosis. A seizure is unprovoked if it does not immediately follow a specific medication or physical maneuver such as flashing lights[2]. Clinically, a person is diagnosed with epilepsy if at least two unprovoked seizures occur greater than 24 hours apart, or if one unprovoked seizure occurs and the recurrent risk is at least 60%, or if other symptoms lead to a diagnosis of an epilepsy syndrome[2].

Why is epilepsy important? Being the 4th most common neurological disorder, epilepsy affects 470,000 children and 3 million adults in the United States, and 65 million people across the world[3,4]. People with epilepsy have a mortality rate 1.6 to 3 times higher than normal[5]. Furthermore, a third of the epilepsy cases are not adequately controlled by medications[1]. Clearly, there is unmet clinical need for developing new treatments for epilepsy.

Epilepsy is, however, not a single disease. First of all, seizures can be generalized (starts in both hemispheres in EEG) or focal (starts in a particular area of the brain in EEG), aware (patient conscious) or impaired-awareness (unconscious during at least part of the seizure), motor (change in muscle activity) or non-motor (change in cognition, emotion, senses, autonomic activity or behavioral arrest)[6,7]. Second, many different types of epilepsy syndromes (certain types and features of seizures occurring together) have been described, some with known and distinct genetic causes such as Angelman Syndrome (duplication or deletion of chromosome 15q11-13) and Dravet Syndrome (mutation in the sodium channel SCN1A)[8]. Third, there are many different causes of epilepsy. For instance, newborns can develop epilepsy through maternal drug use and adults can develop epilepsy through head trauma or stroke[9]. In fact, 6 out of 10 cases of epilepsy have an unknown cause[1]. In this proposal, we will focus on a specific type of epilepsy called absence epilepsy.

Absence epilepsy: Classification, significance and etiology

Absence epilepsy is characterized by typical absence seizures (TAS), which are brief (3-30 seconds, usually < 10 seconds), generalized-onset (must have stereotypical >2.5 Hz spike-wave discharges bilaterally in EEG) seizures associated with a transient loss

of consciousness[10]. Simple TAS is non-motor and associated with a cessation of movement, whereas complex TAS can be associated with slight movements such as eyelid fluttering and hand/face automatisms[10]. When generalized-onset seizures have a longer duration (10-30 seconds), lower spike-wave frequency (< 2.5 Hz), a more gradual onset and termination, an incomplete loss of consciousness and an increased likelihood to be accompanied by movements, they are called atypical absence seizures[10,11]. The International League Against Epilepsy (ILAE) currently classifies cases with typical absence seizures into four epilepsy syndromes, all seen in school-age children: childhood absence epilepsy (CAE, or pyknolepsy), juvenile absence epilepsy (JAE), juvenile myoclonic epilepsy (JME) and epilepsy with myoclonic absences[12]. Some major differences are: the age of onset is 3-11 years old (most often 5-8 years old), 9-13 years old, 5-16 years old and 1-12 years old, respectively; the mean duration of seizures is about 10 seconds for CAE vs. 10-45 seconds for JAE and 10-60 seconds for myoclonic absences; CAE can be more easily controlled than JAE with medications (90% vs. 37% in one study); children often grow out of the seizures for CAE (1 year medication-free remission rate 65-82%) whereas the other syndromes are often life-long conditions[12–17].

Absence epilepsy is a debilitating condition. Except for JME in which seizures usually occur only after awakening, children with absence epilepsy may have up to 100 seizures a day[13,14]. Children also often have cognitive and linguistic impairment such as reading disabilities and ADHD at diagnosis, and in one study 35% of CAE patients continued to have attentional deficits even after treatment[18,19]. Furthermore, roughly 40% (range 8-69%) of children with typical absence seizures at diagnosis eventually develop generalized tonic-clonic seizures, which most likely occur 5-10 years after the onset of absence seizures[18,19]. Prognosis is worse when there is development of myoclonic seizures, late onset

of seizures (> 8 years), abnormal inter-ictal EEG, multiple spikes per spike-wave and focal abnormalities[15,16,18].

The three most common drugs used to treat absence epilepsy are ethosuximide (blocks calcium currents (mainly T-type) and reduces a persistent sodium current and a calcium-activated potassium current[20,21]), valproic acid (raises brain level of GABA and affects sodium and calcium channels[18]) and lamotrigine (blocker of voltage-gated sodium channels[18]). In a 2010 double-blind, randomized, controlled clinical trial on CAE patients, the 16-20 week and 12-month failure rate were 47% and 55% for ethosuximide, 42% and 56% for valproic acid, and 71% and 79% for lamotrigine[22,23]. Furthermore, the group treated with valproic acid experienced the highest rate of adverse events such as attentional dysfunction at both time points. In a follow-up, randomized, controlled clinical trial, the three drugs exhibited similar relative failure rates and adverse event rates as a second medication[24]. Therefore, ethosuximide is the currently preferred drug of choice for either first or second monotherapy[25].

Nevertheless, these studies suggest that up to a quarter of CAE patients do not respond to either the first or second treatment. Furthermore, even if seizures were adequately controlled by medications, the cognitive, behavioral and psychiatric comorbidities that are either pre-existing or medication-induced often overwhelms the effects of the seizures themselves[25,26]. In the aforementioned randomized control trial, attention deficits occur in 36% of CAE patients and persisted even when seizure freedom was attained[27]. When formally assessed, more than 60% of patients had a psychiatric diagnosis[28]. A case-control study showed that although young adults with absence epilepsy have a higher terminal remission rate (57% vs 28 %) than those with juvenile rheumatoid arthritis

(a non-neurologic chronic disease), those with absence epilepsy actually had poorer psychosocial outcomes[29]. Therefore, there is great unmet clinical need to develop new effective treatments with minimal side effects.

There are strong genetic links to all four types of absence epilepsy. A positive family history of epilepsy was found in 15-44% of CAE cases, and the monozygotic twin concordance rate for CAE was 75% (84% show spike-wave discharges on EEG)[18,30]. So far, the human genes implicated in CAE are as follows:

Name of Gene	Identity of Protein
GABRG2[31,32]	the γ2 subunit of synaptic $GABA_A$ receptors
GABRA1[33]	the α1 subunit of synaptic $GABA_A$ receptors of cortical and TC neurons
GABRB3[34–37]	the β3 subunit of synaptic $GABA_A$ receptors of RT neurons
CACNA1A[38,39]	α1A subunit of presynaptic P/Q-type $Ca_V2.1$ channels
CACNA1G[40]	α1G subunit of T-type $Ca_V3.1$ channels
CACNA1H[41–43]	α1H subunit of T-type $Ca_V3.2$ channels
CACNG3[44]	γ3 auxiliary subunit of voltage-gated calcium channels
CLCN2[45]	chloride channel
JRK/JH8[46]	JRK jerky homolog
LGI4[47]	leucine-rich, glioma inactivated 4
SLC2A1[48,49]	Glut1 glucose transporter
INHA[50]	inhibin alpha subunit

From the table, one can see that susceptibility genes for pure absence seizures mostly consists of subunits of $GABA_A$ receptors and calcium channels. However, most of these mutations are found in only a few patients (so the mode of inheritance remains largely unidentified) or a few families, or in only certain populations, and thus absence epilepsy is likely a polygenic disease[18,51]. Note that a genetic variant of the $Ca_V3.2$ T-type calcium channel was associated with a lack of treatment response to ethosuximide[52], suggesting that ethosuximide treats seizures primarily through blocking T-type calcium channels.

Absence seizures: EEG features

What are some distinguishing features of absence seizures? The EEG shows bilateral, synchronous symmetric spike-wave discharges (SWD) of about 3 Hz (> 2.5 Hz, typically 3-4.5 Hz) that start and end abruptly[12,18] (see Figure 1). The spike-wave discharges are stereotyped and the majority show one or two spikes per wave[18]. In between seizures, the EEG shows mostly normal background activity, although sometimes focal epileptiform discharges in frontal, temporal and parietal areas and abnormal intermittent bilateral delta (2.5-4 Hz) activity in the occipital lobe can be recorded[18]. Both spike-wave discharges and the posterior delta activity can be enhanced by hyperventilation and drowsiness[18]. In fact, both forced hyperventilation and total sleep deprivation are common techniques to test for absence seizures clinically. Notably, the shortness of the seizure durations and the abruptness of termination is so far largely unexplained.

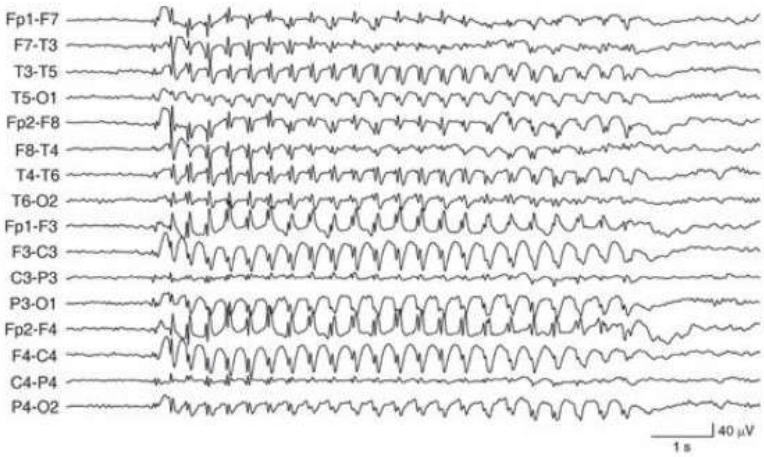

Figure 1. An example of a spike-wave discharge on human EEG[53]

Animal models for absence seizures

There are many animal models available for studying absence seizures. These are

classified into five groups: pharmacological models in which systemic injection of a drug induces absence seizures, monogenic inbred mouse models presenting with spontaneous absence seizures and additional neurological abnormalities, transgenic mouse models that display absence seizures, transgenic mouse models that display full or partial resistance to pharmacologically-induced SWDs and polygenic inbred rat models that seem to display spontaneous absence seizures without other abnormalities. These are summarized as follows:

Pharmacological	FGPE model: Intramuscular injection of penicillin in cats GHB model: Systemic injection of γ-hydroxybutyric acid (or the prodrug γ-butyrolactone, GBL) in rats, mice, cats or monkeys[53,54] PTZ model: Systemic injection of low-dose pentylenetetrazol in rats[55]
Monogenic inbred	*tottering* mice (*tg*, a P601L missense mutation in the α1A subunit of $Ca_V2.1$ channels) also has abnormal movements and postures[56,57] *leaner* mice (tg^{la}, a different mutation in the α1A subunit of $Ca_V2.1$ channels) also shows slow cerebellar degeneration[57] *ducky* mice (*du*, a mutation in the α2δ subunit of $Ca_V2.1$ channels) also shows ataxic gait and paroxysmal dyskinesia[58] *lethargic* mice (*lh*, a mutation in the β4 subunit of $Ca_V2.1$ channels) also has ataxia and lethargic behavior[59] *stargazer* mice (*stg*, a mutation in the γ2 subunit of $Ca_V2.1$ channels) also has ataxia and head-tossing[60]
Transgenic with absence seizures	$Ca_V3.1$ overexpression mouse[61] TRIP8b knockout mouse[62] $GABA_A$ β3 subunit knockout mouse (also has Angelman syndrome-like symptoms)[63] $GABA_A$ γ2 subunit R43Q mutation mouse[64] Succinic semialdehyde dehydrogenase knockout mouse (often cause SUDEP)[65] GABA transporter 1 knockout mouse (also has schizophrenia-like symptoms)[66,67] GluA4 knockout mouse[68]

Transgenic resistant to absence seizures	$Ca_V3.1$ knockout mouse[69] $Ca_V3.3$ knockout mouse[70] (spindle-resistant) $GABA_A$ α3 subunit knockout mouse[71] $GABA_A$ δ subunit knockout mouse[66]
Polygenic inbred	GAERS (genetic absence epilepsy rats from Strasbourg) rats WAG/Rij (Wistar albino Glaxo/Rijswijk) rats

Due to evidence for strong genetic predisposition in absence epilepsy as described above and the lack of chronicity of seizures in the pharmacological models, genetic animal models have been favored[72]. Furthermore, since polygenic inbred rat models seem to exhibit an isolated phenotype of typical absence seizures, GAERS rats and WAG/Rij rats have been the most widely used animal models of absence seizures to date.

What are the similarities and differences of the animal models with human absence epilepsy? Whereas most patients with CAE remit by their late teens, seizures in all genetic absence models continue for the entire life span. In fact, for all strains, there is a monotonous increase in both number and duration of seizures with age[72]. In GAERS rats, seizures begin appearing at 40-120 days of age. WAG/Rij rats have 300-400 seizures a day at six months of age[72]. Seizures in rats most commonly occur during passive wakefulness (drowsiness) and light slow wave sleep (stage II sleep), occur rarely in REM sleep, and prevail in transitional states (e.g., awakening), all consistent with studies in humans[73]. On EEG, both GAERS and WAG/Rij rats have bilaterally symmetric SWDs generalized over the entire cortex that start and end abruptly with durations of 1-30 seconds, comparable to those of humans[72,74]. As in human absence seizures, SWDs are accompanied by behavioral arrest, but also sometimes accompanied by slight motor movements such as facial myoclonic jerks, vibrissae twitching, accelerated breathing, head tilting or eye twitching[72,74]. However, the frequency of rodent SWDs is 7-11 Hz, higher than those of humans[72,74]. In fact, there appears to be a negative correlation of SWD frequency with body size, as the

FGPE model (cats) exhibits SWDs of ~4.5 Hz, whereas only in primates could 3 Hz SWDs be pharmacologically induced[53,74]. Thus, the higher frequency in animal models may merely reflect the smaller size of the neural networks involved. Pharmacologically, only anti-absence drugs such as ethosuximide, valproic acid and trimethadione decreases the number of SWDs in rats, whereas other anti-convulsants such as phenytoin, carbamazepine, tiagabine and vigabatrin do the opposite, consistent with their respective effects on human absence seizures[72,74]. Therefore, many of the available rat models seem to have both face validity (similar EEG/behavioral manifestations) and predictive validity (similar outcomes to treatments).

Neural correlates of absence seizures

Which brain areas are activated during absence seizures? Simultaneous fMRI-EEG recordings showed increased BOLD signals in the thalamus, frontal cortex, primary visual, auditory, somatosensory, and motor cortex, cerebellum and decreased BOLD signals in the lateral and medial parietal cortex and basal ganglia during SWDs[75,76]. In WAG/Rij rats, fMRI shows specific activation of somatosensory cortex, but not the occipital cortex[77]. Therefore, it seems that networks for normal attention (thalamus-frontal cortex) and sensory processing (thalamus-primary cortices) are hijacked during seizures to result in the loss of consciousness observed. Furthermore, in an fMRI-EEG study, the change in BOLD signals in these regions was associated with impaired performance of an attention task[75]. However, during SWDs, visually-evoked event-related potentials in humans and whisker-evoked event-related potentials in GAERS rats are preserved, showing that at least some sensory processing is still possible during seizures[78].

Which brain areas are necessary for absence seizures? In a study done in GAERS

rats, ablation of the cortex suppressed SWDs recorded in the thalamus, and large lesions of the lateral thalamus suppressed SWDs recorded in the cortex, suggesting that both the cortex and the thalamus are involved in the generation of SWDs[79].

Do absence seizures begin in the thalamus or in the cortex? Initially, SWDs were thought to be initiated in subcortical structures, due to a common midline subcortical pacemaker[80]. Early field recordings in inbred Wistar rats showed that lateral thalamic activity (but not the midline thalamus) preceded cortical activity in SWDs, suggesting that the thalamus offers a driving force for seizures[81]. However, subsequent research has showed stronger support for the "cortical focus theory," in which SWDs are thought to be initiated in the cortex. In barbiturate-anesthetized cats, local injection of bicuculline (a $GABA_A$ receptor antagonist) in the cortex induced 4 Hz spike-wave activity throughout the cortices bilaterally while the thalamus remained in the spindling state[82]. This still held true after removing one half of the thalamus, supporting the idea that the cortical network is sufficient for SWD generation[82]. However, the spike-wave activity induced was preceded by runs of 10-20 Hz spikes, spread gradually from a focus, and did not have behavioral correlates since the animal was anesthetized. Therefore, the relationship of this pure-cortical SWD to typical absence seizures is unclear. In WAG/Rij rats, nonlinear correlation analysis of multisite field recordings showed that activity in the perioral region of the somatosensory cortex preceded activity in the thalamus by a mean time of 8.1 ms during the first 500 ms of an absence seizure[83]. In GAERS rats, field recordings showed that facial somatosensory activity preceded either the motor cortex or the thalamus during seizures, and further pinpointed layer 5/6 neurons as the initiators of epileptic discharges[84]. Furthermore, intracellular recordings showed that spontaneous 9-11 Hz oscillations at this cortical focus precede seizures[84]. Intracortical microinfusion of ethosuximide or topical

application of tetradotoxin (a sodium channel blocker that abolishes action potentials) in the somatosensory cortex, but not in the motor cortex, immediately ceased SWDs in GAERS rats, showing that the seizure initiation site is cortical-area specific, at least for rodent models[85,86]. Therefore, there is ample evidence to support the cortical focus theory of SWD generation. However, in humans, beamformer analysis using synthetic aperture magnetometry (SAM) in an MEG-EEG study showed that activity 50 ms prior to the start of seizures can be located in both the frontal cortex and the thalamus[87]. Therefore, the role that the thalamus plays in absence seizure generation still warrants further investigation.

Nevertheless, the thalamus is essential at least for the maintenance of SWDs. In callosotomized GAERS rats, lesioning the reticular thalamic (RT) nucleus with ibotenic acid (a neurotoxin) disrupts ipsilateral SWDs[88]. In PTZ treated rats, bilateral lesions of RT suppressed SWDs[89]. In intact WAG/Rij rats, a complete ipsilateral lesion of the right RT nucleus with ibotenic acid decreased the number of SWDs to less than 10%, whereas a total ipsilateral thalamic lesion abolished SWDs completely[90]. These results pinpoint the RT nucleus as an essential structure in the generation and or maintenance of SWDs. Granger causality analysis on field recordings of WAG/Rij rats showed that during SWDs, activity in the thalamus predicted activity in the cortex to a much greater extent than the other way around, suggesting that the thalamus drives each cycle of SWDs[91]. In a study done on fentanyl-anaesthetized WAG/Rij rats, simultaneous field recordings in different areas of the thalamus and cortex showed that the spike component of SWDs was phase-locked to activity in the specific thalamic relay nuclei (ventroposterior lateral (VPL), ventroposterior medial (VPM), ventrolateral (VL)), the mediodorsal (MD) nucleus, the RT nucleus and the cortex[92]. At each spike, the specific relay nuclei activity preceded both RT and cortical

activity[92]. A similar study done on fentanyl-anaesthetized GAERS rats confirmed that whereas cortical activity preceded thalamic activity at the onset of SWDs, relay nuclei activity preceded RT and cortical activity at each spike component of an SWD[93]. Therefore, while the cortex might contain the focus that initiate seizures, the thalamocortical (TC) relay neurons might be responsible for maintaining seizures by initiating subsequent cycles of oscillations. On the other hand, the wave component of SWDs in fentanyl-anaesthetized WAG/Rij rats and GAERS rats were phase-locked to activity in the centrolateral/paracentral nucleus and the anteroventral/ventrolateral nucleus of the thalamus, respectively, indicating that non-relay nuclei of the thalamus might also play a role in the maintenance of SWDs[92,93].

In summary, a thalamocortical network involving the cortex, the reticular thalamic nucleus and the thalamocortical relay nuclei appears to be responsible for the generation of SWDs. The same thalamocortical network is thought to be responsible for spindle oscillations during normal stage II sleep and the cortical slow wave oscillations during normal stage IV sleep[94]. We next explore the anatomy and physiology of thalamocortical oscillations and the possible pathophysiology of spike-wave discharges.

Projections between the thalamus and the cortex

How does the thalamus influence the cortex? Thalamocortical projections arise from TC neurons in the thalamocortical relay nuclei. Specific thalamocortical relay nuclei such as the VPL, VPM, VL, the lateral geniculate nucleus (LGN) and nuclei in the anterior nucleus relay information from subcortical structures to the cortex, whereas higher-order thalamocortical relay nuclei relay information from cortical neurons to other cortical neurons[95]. These are all glutamatergic projections that predominantly project to layer IV of

the cortex[96], except for the layer IV-deficient motor cortex (in which case the projections end in layers II/III and V)[97]. Different parts of the thalamus project to different parts of the cortex, and so there is a parallel, topographic organization of thalamocortical columns[98].

How does the cortex influence the thalamus? Corticothalamic projections arise from pyramidal neurons in cortical layers V and VI[99]. Those arising from layer VI cortex project, often bilaterally, to specific thalamocortical relay nuclei and give off collaterals to the RT nucleus (or the perigeniculate (PGN) nucleus if coming from the visual cortex), which contains GABAergic neurons projecting to the thalamocortical relay nuclei; those arising from layer V cortex project to higher-order thalamocortical relay nuclei and do not give off collaterals to the reticular thalamic nucleus[95]. Corticothalamic projections are glutamatergic[100], accounts for 25-31% of all synapses that TC neurons receive[101–103], and accounts for 50-65% of all synapses that RT neurons receive[104]. Different parts of the cortex project to different parts of the thalamus, preserving the parallel, topographic organization of thalamocortical columns, with low convergence and divergence[105]. Corticothalamic projections outnumber thalamocortical feedback by an order of magnitude[106]. Extracellular single unit recordings in the ventrobasal nucleus (VB, the area containing somatosensory relay nuclei in rodents) of anaesthetized rats showed that corticothalamic axons could be activated from the contralateral cortex and elicits a clear excitation followed by inhibition[107]. Here, the inhibitory responses are thought to be mediated through RT because no interneurons are found in the VB nucleus[100]. In fact, by sending a strong excitation to both TC and RT neurons, corticothalamic projections result in both direct excitation (cortex to TC) and feedforward inhibition (cortex to RT then to TC), respectively, at the TC neurons.

Projections between RT/PGN neurons and TC neurons within the thalamus

What about projections among nuclei within the thalamus? Studies in cats and rats using horse-radish peroxidase (HRP) staining showed that at least 60-80% of thalamocortical projections give off collaterals to RT neurons (or to PGN neurons if coming from lateral geniculate neurons), but not collaterals to other TC neurons[108,109]. Being collaterals of thalamocortical axons, these TC-RT connections are glutamatergic. Are these connections convergent? First of all, TC neurons greatly outnumber PGN or RT neurons[110]. In electron microscopy studies, PGN neurons are densely innervated by terminals from TC neurons, suggesting convergence of TC-RT connections[110,111]. In support of this, in ferret thalamic slices, the average amplitude of excitatory post-synaptic currents (EPSCs) from TC neurons recorded in PGN neurons were 5-8 times larger during spindle waves than that generated by a burst of a single TC neuron[110]. Based on this finding, the same study estimated that 20-40 TC neurons innervate a single PGN neuron[110]. What about divergence? In HRP staining studies, TC-RT connections typically do not bifurcate extensively nor give rise to dense synaptic arborization, suggesting that TC-RT connections are not divergent[108,112,113]. In support of this, simultaneous recording of nearby RT neurons (whether electrically coupled or not) in mouse thalamic slices showed very little synchrony in the EPSCs recorded[114]. Therefore, these TC-RT connections are excitatory, convergent but not divergent, with neighboring RT neurons receiving sparse non-overlapping input from many TC neurons[114].

On the other hand, there are also GABAergic projections from RT neurons to TC neurons, called RT-TC connections. Biocytin labelling studies in rat thalamic slices have shown that individual RT neurons can give rise to diffuse axonal arborizations, suggesting high convergence and divergence of RT-TC connections[115,116]. In support of convergence,

in ferret thalamic slices, the average amplitude of inhibitory post-synaptic currents (IPSCs) from PGN neurons recorded in TC neurons were ~4 times larger during spindle waves than that generated by a burst of a single PGN neuron. Based on this finding, the same study estimated that 10-20 PGN neurons innervate a single TC neuron[110]. In support of divergence, simultaneous recordings of nearby TC neurons in mouse thalamic slices showed a strong covariation of IPSCs evoked by activation of RT-TC connections (indirectly through optogenetically activating cholinergic input to RT)[114]. Based on morphology, the ferret study estimated that a single PGN neuron innervates 100-170 TC neurons[110]. Therefore, RT-TC connections are inhibitory, convergent and divergent. Despite the divergence, biocytin labelling studies also showed that most RT-TC connections project to a single nucleus of the anterior, dorsal, intralaminar, posterior, or ventral thalamus, with distinct sectors of RT projecting to distinct nuclei, further preserving the parallel, topographic organization of thalamocortical columns[116]. By transmitting the excitatory signal from cortical neurons, and by reciprocating the excitatory signal from TC neurons, these connections play a role in feedforward inhibition and feedback inhibition of the thalamus, respectively[117]. A biocytin-labelling study in intact rat brains showed that RT-TC connections largely project in a somatotopic manner, supporting the principle of reciprocity between RT neurons and TC neurons along the same radial axis[118]. However, not all RT neurons send axons back to the TC neurons that excite them, so a TC neuron firing can cause a polysynaptic IPSP on a nearby TC neuron through RT neurons, which is termed lateral inhibition[119].

Connections among RT/PGN neurons

GABAergic RT-TC connections have been found to give off collaterals to nearby RT neurons, in cats[120,121], rats[104,115,122] and monkey[123]. In acute mouse brain slices cut in an

angle (35° tilt from coronal) that preserved thalamocortical circuitry, electrical stimulation of cortical layer VI elicited, in RT neurons, di- or polysynaptic IPSCs that were sensitive to both bicuculline (a $GABA_A$ receptor blocker) or a combination of CNQX (an AMPA receptor blocker) and APV (an NMDA receptor blocker)[124]. Antidromic stimulation of RT axons in VB also evoked IPSCs in RT neurons[125]. In ferret thalamic slices, local application of glutamate in PGN or RT elicited IPSPs with a reversal potential of -77 mV or -72 mV that were abolished by bicuculline or picrotoxin, respectively[126,127], indicating that intra-RT GABAergic connections are mediated mostly through $GABA_A$ receptors. However, three pieces of evidence have called the existence of intra-RT inhibition into question: (1) paired recordings revealed very little IPSPs elicited by neighboring RT neurons[128,129]; (2) optogenetic stimulation of corticothalamic axons failed to evoke disynaptic IPSCs in RT neurons[130]; (3) optogenetic stimulation of RT neurons failed to evoke IPSCs in other RT neurons[131]. As discussed later, the plane of slice preparation might have been the cause of the discrepancy among findings[132].

On the other hand, *in situ* hybridization studies showed that expression of connexin-36 (a gap junctional protein) was high in the RT nucleus but absent in the VB nucleus[133] and the expression of pannexin-1 (another potential gap junctional protein) was also much higher in the RT nucleus than the rest of the thalamus, supporting the observation that electrical connections are a unique property for GABAergic neurons[134]. Paired recordings of nearby RT neurons revealed electrical coupling that were present in control mice but not in connexin-36 knockout mice, strongly supporting that functional electrical connections (gap junctions) exist between RT neurons[128].

Do intra-RT GABAergic or electrical connections play a more important physiolog-

ical role? In acute rat thalamic slices, local stimulation of RT neurons via glutamate uncaging elicited more IPSCs than spikelets (62% vs 17%), indicating that GABAergic chemical connections might predominate over electrical connections[135]. A similar study confirmed this finding and further showed that GABAergic chemical connections are predominant in the anteroposterior (horizontal) plane, whereas electrical connections are predominant in the dorsoventral (vertical) plane[132]. Nevertheless, as explained later, both intra-RT electrical and GABAergic connections seem to play a role in absence seizures.

Summary of the basic anatomical circuitry for thalamocortical oscillations

In summary, there are non-divergent excitatory connections from TC neurons to RT neurons, divergent inhibitory connections from RT neurons back to TC neurons, intra-RT GABAergic connections and intra-RT electrical synapses, forming the basic intra-thalamic circuit. This circuit, in addition to thalamocortical projections and corticothalamic projections, forms the core of the basic thalamocortical circuit (see Figure 2). Later on, we will discuss how the basic intra-thalamic circuit could drive spindle-like oscillations or SWD-like oscillations in the basic thalamocortical circuit.

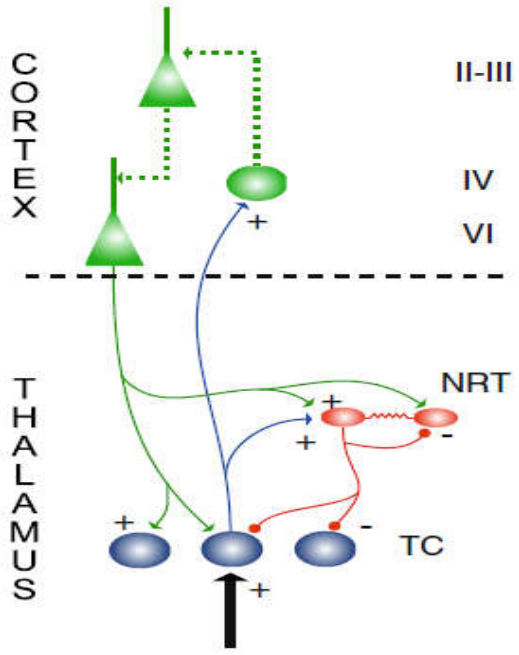

Figure 2. The basic thalamocortical circuit[143]

Pathophysiology of absence seizures—introduction

How does the basic thalamocortical circuit lead to sustained oscillations over time? What is different in the circuitry to produce aberrant SWDs as opposed to normal spindle oscillations? To answer this, we will first discuss in turn the distinctive properties of RT neurons, TC neurons, the corticothalamic projections, the RT-TC GABAergic connections and the intra-RT connections (both GABAergic and electrical).

RT neurons: Electrophysiology, channels involved and their significance

What are the electrophysiological properties of RT neurons? Intracellular recordings in rat thalamic slices showed that at the resting membrane potential (about -56 mV), RT neurons exhibit tonic firing, in which a depolarizing input would elicit isolated action potentials (spikes) that are followed by a rapid spike after-hyperpolarization potential (SAHP)[136]. At membrane potentials more negative than -60 mV, RT neurons gradually switch to a burst firing mode, in which a depolarizing input would elicit a burst of spikes superimposed on a slow depolarizing potential called a low-threshold spike (LTS)[136]. Thereafter, upon release from hyperpolarization, RT neurons would generate a post-inhibitory rebound LTS, or a post-inhibitory rebound burst if the LTS reaches the threshold for sodium spikes (action potentials). In cats, extracellular unit recordings of RT neurons displayed tonic firing when the animal was awake and burst firing when the animal was asleep[137,138]. In sleeping cats, bursts consisted of 4-9 spikes at 80-180 Hz and were long in duration (50-1500 ms)[137,138]. In both rats and sleeping cats, spikes within a burst in RT neurons follow an accelerando-decelerando firing pattern, in which the duration of successive inter-spike intervals first decreased than increased[136–138]. In rat thalamic slices, the bursts were followed by a pronounced hyperpolarization that lasted 80-120 seconds,

termed a burst after-hyperpolarization potential (BAHP)[136]. When the RT neuron was depolarized a voltage between -85 and -60 mV from a hyperpolarized potential of -90 mV, an oscillation of burst-BAHP complexes at around 6-8 Hz occurs[136]. Therefore, RT neuron may intrinsically oscillate. Similar oscillations were found in intracellular recordings of guinea pig thalamic slices[139]. In fact, in anaesthetized cats, intracellular recordings in rostral RT found that RT neurons intrinsically oscillate at 7-12 Hz, with such spindle waves riding on the peaks of a slow 0.1-0.2 Hz oscillation[140]. When the RT nucleus was isolated from the rest of the thalamus, 7-16 Hz spindle waves that recur with a rhythm of 0.1-0.3 Hz could still be recorded, suggesting that RT neurons can function as an intrinsic pacemaker on its own[141]. Notably, there is also heterogeneity among RT neurons and regional differences between the dorsal and ventral parts of the RT nucleus. Intracellular recordings in rat thalamic slices showed that while most neurons (82%) in the ventral RT nucleus fire typical bursts, those in dorsal RT nucleus fire impoverished bursts (35%) or single spikes (56%)[142].

What channels on RT neurons give rise to its intrinsic oscillatory behavior? It is thought that a hyperpolarization of the membrane potential would de-inactivate a T-type calcium current (I_{Ts}) that underlie the post-inhibitory rebound LTS, and the subsequent increase in intracellular [Ca^{2+}] would activate an after-hyperpolarization current (I_{ahp}) that hyperpolarizes the membrane potential (BAHP) and starts the next cycle of the oscillation[139]. We will now discuss these two currents in detail:

- **T-type calcium channels (T channels)**

  T-type calcium currents (I_{Ts}) are conducted by calcium channels that are transiently activated upon depolarization, inactivated at relatively depolarized potentials

and de-inactivated at relatively hyperpolarized potentials[143]. It is thought that T currents are responsible for the post-inhibitory rebound LTSs. Upon hyperpolarization of the membrane potential, T-type calcium channels are de-inactivated, so subsequent depolarization would activate I_T and result in a long-duration depolarization[144]. In rat and guinea pig thalamic slices, LTS persists in RT neurons after application of TTX (a sodium channel blocker), albeit without overriding sodium spikes[136,139]. A similar finding was demonstrate in anaesthetized cats after application of QX314 (also a sodium channel blocker)[140]. Therefore, the LTS is thought to be calcium-dependent. In transgenic mice ($Ca_V3.3$ knockout, see later) with T channels selectively deficient in RT neurons, RT neurons showed an impaired ability to produce rebound spikes and depolarizations from hyperpolarized potentials failed to induce oscillations. These mice also showed an impaired ability to form spindle oscillations during non-REM sleep[70]. Therefore, T channels are necessary for both LTS generation and the intrinsic pacemaker behavior of RT neurons[70].

Using *in situ* hybridization in rats, RT neurons were found to express both $Ca_V3.2$ and $Ca_V3.3$ calcium channels[145]. Electrophysiological measurements of currents induced by heterologous expression of these channels in HEK-293 cells showed that $Ca_V3.3$ channels activate and inactivate about three times slower than $Ca_V3.2$ channels[146]. In rat thalamic slices, T currents recorded in the dendrites had a slower inactivation time course than those recorded in the soma, indicating that $Ca_V3.2$ channels might be expressed more in the soma and $Ca_V3.3$ channels expressed more in the dendrites[147].

Which of $Ca_V3.2$ and $Ca_V3.3$ is more important in setting the electrophysiological properties of RT? In rat thalamic slices, the T currents in RT neurons were

found to have a much slower decay time constant and a more depolarized activation range than T currents of TC neurons (discussed later), suggesting that the slower-activating/inactivating $Ca_V3.3$ channels might play a more dominant role than $Ca_V3.2$ channels[70,143]. In a study in rat thalamic slices that simultaneously recorded RT neurons intracellularly and measured calcium dynamics with two-photon laser scanning microscopy, injection of a depolarizing current in the soma elicited a 4-fold increase in calcium response in the distal dendrites relative to the soma, supporting a dominance of distally-expressed $Ca_V3.3$ channels[144]. Finally, in a transgenic $Ca_V3.3$ knockout mouse, T current density was much decreased in RT neurons compared to wild type mice, further supporting the dominance of $Ca_V3.3$ channels[70].

What is the significance of $Ca_V3.2$ and $Ca_V3.3$ channels in absence seizures? Even though $Ca_V3.3$ channels seemed to be more dominant electrophysiologically, it is a mutation in Cav3.2 channels that has been linked to childhood absence epilepsy genetically (in a cohort of Han Chinese patients)[41]. Intracellular recordings of rat thalamic slices showed that T current density of RT neurons was larger in both WAG/Rij rats and GAERS rats than in non-epileptic control rats[148,149]. Using *in situ* hybridization, GAERS rats were found to have a higher expression of $Ca_V3.2$ channels in RT neurons than non-epileptic control rats[150]. Using RT-PCR, WAG/Rij rats were found to have a higher expression of both $Ca_V3.2$ and $Ca_V3.3$ channels in RT neurons than non-epileptic control rats[149]. In thalamic slices of GAERS rats, high affinity T channel blockers Z941 and Z944 attenuated burst firing in RT neurons[151]. Furthermore, *in vivo* administration of these drugs suppressed absence seizures in GAERS rats by 85-90%[151]. These results demonstrate a role of RT neuronal T channel hyperactivity in the generation of SWDs.

- **Small conductance calcium-activated potassium channels (SK channels)**

Small conductance calcium-activated potassium channels open on activation by low concentrations of Ca^{2+}, resulting in an efflux of K^+ ions and a hyperpolarization of the membrane potential[152]. It is independent of voltage and gated solely by intracellular calcium levels[153]. In hippocampal neurons, a similar after-hyperpolarization current was found to be sensitive to Ba^{2+} (a potassium channel blocker), Mn^{2+} (a calcium channel blocker) and EGTA (a calcium chelator), but not to TTX (a sodium channel blocker) or to intracellular Cl^- iontophoresis (which abolishes the chloride gradient)[154,155]. Immunohistochemical studies in both mouse and rats showed that the thalamic reticular nucleus expressed a high density of $K_{Ca}2.2$ (SK2) subunits as well as a lower density of $K_{Ca}2.1$ (SK1) and $K_{Ca}2.3$ (SK3) subunits[156]. Therefore, SK channels are thought to be responsible for the after-hyperpolarization current (I_{ahp}) that follow bursts of action potentials and thus for generating the BAHP. Indeed, in rat thalamic slices, BAHP of RT neurons were abolished with application of Cd^{2+} (a calcium channel blocker) and apamin (an SK channel blocker), but not with 8-Br cyclic AMP (a blocker for a different type of calcium-dependent potassium channel)[136,157].

Notably, in rat thalamic slices, application of bicuculline (a known $GABA_A$ receptor blocker) suppressed BAHP and reduced the amplitude of I_{ahp} in RT neurons[157], indicating that SK channels are also partially blocked by bicuculline. Also in rat thalamic slices, stimulation of corticothalamic fibers induce spindle-like oscillations that are transformed to prolonged 3 Hz epileptiform oscillations upon bath application of bicuculline[158]. Such bicuculline-induced epileptiform oscillations could not be reproduced with application of picrotoxin (a specific $GABA_A$ antagonist) or apamin (a spe-

cific SK channel blocker), but could be reproduced with application of picrotoxin combined with subnanomolar concentrations of apamin (which partially blocks SK channels), demonstrating that both intra-RT inhibition (discussed later) and SK channels are important in preventing epileptiform oscillations[158].

How could activation of SK channels prevent seizures? In rat thalamic slices, application of apamin increases the duration of post-inhibitory rebound bursts of RT neurons and abolishes the BAHP[157]. In RT neurons, but not in TC neurons (which lack SK channels), application of an increasing concentration of apamin increased the spike frequency under a depolarizing stimulus and increased the duration of post-inhibitory rebound bursts[158]. Therefore, I_{ahp} seems to be important in limiting the burst durations of RT neurons. As further explained later, an increase in RT burst duration would prolong IPSCs on TC neurons, activate $GABA_B$ IPSPs, increase synchrony and lead to slower and stronger epileptiform oscillations[158].

TC neurons: Electrophysiology, channels involved and their significance

What are the electrophysiological properties of TC neurons? In guinea pig thalamic slices, just like RT neurons, TC neurons exhibit tonic firing at depolarized potentials (> -60 mV), burst firing at hyperpolarized potentials (< -65 mV), and post-inhibitory calcium-dependent rebound LTSs or bursts that were sensitive to Co^{2+} (a calcium channel blocker)[159]. In sleeping cats, bursts consisted of 2-7 spikes at 250-400 Hz, with a shorter duration than that of RT neurons[137,160]. In contrast to the accelerando-decelerando firing pattern, there was a progressive increase in the duration of successive inter-spike intervals[137,160]. In cats, just like for RT neurons, extracellular unit recordings of TC neurons displayed tonic firing when the animal was awake and burst firing when the animal was asleep[160]. In cat and rat

thalamic slices bathed in low [Mg^{2+}] (0.5-0.8 mM) and high [Ca^{2+}] (2-4 mM), 50-60% of TC neurons also became intrinsic pacemakers at a resting potential of -80 mV to -55 mV: periodic, large amplitude (10-30 mV) LTSs lasting 80-350 ms and occurring at 0.5-3 Hz were generated, with single spikes or bursts consisted of 2-7 spikes at 250-400 Hz riding on top of each LTS[161]. These pacemaker oscillations were also found in slices that lack LGN (cats) or RT (rats)[161].

What channels on TC neurons give rise to its intrinsic oscillatory behavior? It is thought that a hyperpolarization of the membrane potential would de-inactivate a T-type calcium current (I_T) and activate a hyperpolarization-activated nonspecific cationic current (I_h). I_h would slowly depolarize the membrane potential until I_T gets activated and generates a post-inhibitory rebound LTS, causing an inactivation of I_T and deactivation of I_h, and the further return to hyperpolarized potentials would start the next cycle of the oscillation[162]. We will now discuss these two currents in detail:

- **T-type calcium channels (T channels)**

  The T-type calcium currents (I_T) in TC neurons have similar electrophysiological properties as the T currents found in RT neurons, but with a faster decay time constant and a more hyperpolarized activation range[143]. In transgenic mice ($Ca_V3.1$ knockout, see later) with T channels absent from TC neurons, TC neurons no longer exhibit burst firing upon hyperpolarization[69]. In rat thalamic slices, bath application of U-92032 (a T channel blocker) reduced the maximum slope of LTS in TC neurons by 90%[163]. Bath application of 1-octanol or Ni^{2+} (both T channel blockers) reversibly blocked the intrinsic pacemaker oscillations described earlier[164]. These results demonstrate that I_T in TC neurons play a similar role as I_{Ts} in RT neurons in the generation of post-inhibitory rebound LTSs and intrinsic pacemaker oscillations.

Using *in situ* hybridization in rats, TC neurons were found to express $Ca_V3.1$ calcium channels, which is also expressed in cortical neurons[145]. Electrophysiological measurements of currents induced by heterologous expression in HEK-293 cells showed that $Ca_V3.1$ channels activate and inactivate about 1.5 and 5 times faster than $Ca_V3.2$ and $Ca_V3.3$ channels, respectively[146].

What is the significance of $Ca_V3.1$ channels in absence seizures? Genetic mutations in $Ca_V3.1$ channels have been linked to human absence seizures[40]. T currents in HEK-293 cells with heterologous expression of mutant versions of Cav3.1 have slightly faster inactivation time constants[40]. Using *in situ* hybridization, GAERS rats were found to have a higher expression of $Ca_V3.1$ channels in TC neurons than non-epileptic control rats[150]. Similarly, using RT-PCR, WAG/Rij rats were found to have a higher expression of $Ca_V3.1$ channels in TC neurons than non-epileptic control rats[149]. Intracellular recordings of thalamic slices showed that T current density of TC neurons was larger in WAG/Rij rats than in non-epileptic control rats[149]. In support of this, $GABA_B$ agonists (GHB and baclofen) could induce SWDs in wild-type mice (more on this later) but not in $Ca_V3.1$ knockout mouse[69]. Conversely, transgenic mice that over-expressed Cav3.1 channels showed frequent bilateral cortical SWDs[61]. In rat thalamic slices, bath application of U-92032 (a T channel blocker) suppressed bicuculline-induced slow oscillations (see before). These results demonstrate a role of TC neuron T channel hyperactivity in the generation of SWDs.

- **Hyperpolarization-activated nonspecific cation channels (HCN channels)**

In guinea pig and cat thalamic slices, voltage clamping TC neurons at hyperpolarized potentials (<-60 mV, with half activation at -75 mV) activated an inward current carried by Na^+ and K^+ ions that reversed at -43 mV and showed a slow activation

time constant (200-700 ms) at hyperpolarized potentials (<-60 mV) and no inactivation with time[162]. This current was termed a hyperpolarization-activated nonspecific cationic current, or h current (I_h) for short. In non-oscillating TC neurons, I_h is thought to contribute to setting the resting membrane potential to a much more depolarized value (-70 to -60 mV) than the potassium reversal potential (-105 mV)[162]. In oscillating TC neurons, I_h is thought to underlie the depolarizing sag phase of each cycle of oscillation[162]. Finally, since it deactivates slowly, I_h is thought to underlie the afterdepolarization (ADP) in TC neurons (see later) that play a key role in the waning phase of spindle oscillations[161,165]. In support of this, in ferret thalamic slices, the ADP was abolished after local application of Cs^+ (an HCN channel blocker)[166].

In cardiac pacemaker cells, patch recordings showed that cyclic adenosine monophosphate (cAMP) cause a depolarizing shift of the activation curve of I_h[167]. This was replicated in guinea pig sensory neurons with I_h having the same sensitivity to many different cyclic nucleotides[168]. Therefore, the channel responsible for I_h was termed hyperpolarization-activated cyclic nucleotide-gated channels, or HCN channels for short. In mice, *in situ* hybridization showed strong expression of HCN2 and HCN4 channels in TC neurons, which are both known to be slow activating and cAMP sensitive[169]. In TC neurons of rat thalamic slices, increasing the intracellular pH to 7.5 and decreasing the intracellular pH to 6.7 caused a depolarizing shift of 4-5 mV and a hyperpolarizing shift of 2-3 mV of the activation curve of I_h, respectively[170]. In first-order relay nuclei, the amplitude of I_h can also be increased by application of norepinephrine or serotonin, possibly through an increase in cAMP[171,172]. Note however that in higher-order relay nuclei, serotonin hyperpolarizes TC neurons instead of enhancing I_h (which would depolarize the resting membrane potential)[172].

What is the significance of HCN channels in absence seizures? Since I_h is responsible for the ADP in spindles, it may be critical for terminating individual spindles. In support of this, in ferret thalamic slices, bath application of Cs^+ resulted in a progressive shortening of the spindle wave refractory period and a lengthening of the duration of individual spindle waves[166]. In a computational model of the basic thalamic network (see later), reducing I_h led to sustained oscillations[173]. Since SWDs are thought to be generated from a similar network circuitry as spindle oscillations (see later), persistent activation of I_h may also cause TC neurons to progressively lose the ability to generate thalamocortical oscillations. In support of this, the transgenic tetratricopeptide-containing Rab8b-interacting protein (TRIP8b) knockout mice (TRIP8b is an auxiliary subunit of HCN channels), which had significantly reduced HCN channel expression in cortical and TC neurons, exhibited ethosuximide-sensitive SWDs[62].

Corticothalamic projections: Electrophysiology and receptors involved

What are the functional consequences of corticothalamic projections? Recall that corticothalamic projections can result in both monosynaptic, direct excitation and disynaptic (through the RT nucleus), feedforward inhibition at the TC neurons. In a study done in rat brain slices, electrical stimulation of corticothalamic fibers evoked 57% pure excitatory response, 27% pure inhibitory response and 16% mixed response in thalamic neurons of the VB nucleus[174]. The excitatory post-synaptic potentials (EPSCs) were predominantly slow rising, showed nonlinear voltage dependence and were blocked by the NMDA receptor antagonist 2-amino-5-phosphonovaleric acid (APV), although a minority had faster kinetics and were blocked by the AMPA receptor antagonist 6-cyano-7 nitroquinoxaline-2,3-

dione (CNQX)[174]. The pure inhibitory response could be separated into a bicuculline-sensitive early phase that had a reversal potential of -95 mV and a CGP-55845A-sensitive late phase that had a reversal potential of -113 mV[174]. In summary, this experiment showed that TC neurons have AMPA, NMDA, $GABA_A$ and $GABA_B$ receptors that could respond to corticothalamic input.

So which one is stronger, direct excitation or feedforward inhibition? In mice, electrical stimulation of corticothalamic fibers evoked excitatory post-synaptic conductances (EPSCs) that were 2.4 times larger in RT neurons than in TC neurons, and the quantal size of EPSCs was 2.6 times greater[175]. Thus it seems that normally, feedforward inhibition via the RT nucleus predominates. As explained later, this would allow the feedforward inhibition to generate post-inhibitory rebound bursts in TC neurons, which would further excite cortical neurons through thalamocortical projections, allowing thalamocortical oscillations such as spindles and SWDs to occur. However, in anaesthetized mice, *in vivo* optogenetic stimulation of layer VI cortical neurons (*Ntsr1-Cre*) only transiently hyperpolarized VB neurons, followed by a prolonged depolarization of the resting membrane potential (which, as explained later, would switch VB neurons from a bursting mode to a tonic firing mode)[176]. Intracellular recordings in TC neurons under optogenetic stimulation of layer VI cortical neurons showed that the sparse corticothalamic input suppressed TC activity, but short bouts of corticothalamic input enhanced TC activity[177]. Therefore, the balance between direct excitation and feedforward inhibition appears to be dynamically regulated in a frequency-dependent manner. Interestingly, the corticothalamic stimulation frequency that optimally evoked burst responses in thalamic neurons was 3-6 Hz, comparable to the oscillation frequency of SWDs[174].

What happens when feedforward inhibition is decreased? GluA4 AMPA receptor

subunits were found to be 3.7 times more numerous on RT neurons than on TC neurons, offering a possible explanation to the larger EPSC amplitude from cortex to RT neurons compared with that of cortex to TC neurons[175]. Indeed, in GluA4 knockout mice, optogenetic stimulation of cortical neurons evoked fewer EPSCs, with a reduced amplitude and slower decay, in RT neurons[178]. However, the EPSCs evoked in TC neurons after cortical stimulation and the EPSCs evoked in RT neurons after TC stimulation in GluA4 knockout mice were no different from those of control mice, indicating that GluA4 subunits are normally present in cortex to RT synapses only, and that cortex to RT synaptic strength is selectively decreased in these mice[178]. Therefore, in GluA4 knockout mice, direct excitation predominates over feedforward inhibition, which is confirmed by a hyperactivation of TC neurons by cortical inputs[178]. Interestingly, these mice exhibit SWDs with behavioral arrest characteristic of absence seizures, likely due to the unmasking of direct corticothalamic excitations[68,178]. This suggests that feedforward inhibition is necessary for maintaining normal thalamic activity.

How else can corticothalamic projections be modulated? A study of a large Australian family strongly linked an R43Q mutation in the $GABA_A$ receptor γ2 subunit to absence epilepsy and febrile seizures[31]. Expressing the R43Q γ2 subunit mutant in human embryonic kidney 293-T cells showed that the mutation traps $GABA_A$ receptors in the endoplasmic reticulum to prevent surface expression[179]. A transgenic mouse model harboring the γ2 subunit R43Q mutation displayed ethosuximide-sensitive absence seizures[64]. Importantly, patch clamp recordings in acute brain slices of these mice showed a reduced amplitude of miniature IPSCs in cortical neurons, but not in RT or TC neurons[64]. Therefore, reduced cortical inhibition may play an important role in absence seizures by disinhibiting corticothalamic feedback.

Intra-RT connections: Electrophysiology, receptors involved and their significance

How can intra-RT connections be modulated? Recall that there are both GABAergic and electrical connections among RT neurons. As discussed before, electrical connections are mediated through connexin-36 containing gap junctions. For the GABAergic connections, immunohistochemical staining studies have shown that RT neurons express synaptic α3β3γ2 $GABA_A$ receptors[180]. We will discuss the properties and significance of these in turn:

- **Gap junctions (connexin-36)**

  Gap junctions are channels of 1.2 nm diameter that are comprised of 12 identical subunits of connexins (connexin-36 for the gap junctions in RT neurons), one on each connecting neuronal membrane[128,181]. Bridging the membranes of neighboring neurons, gap junctions are thought to quickly transmit changes in membrane potential from one neuron to another and synchronize activity. The presence of gap junctions has thus been hypothesized to increase network synchrony. In fact, in rat thalamic slices, simultaneous recordings in RT neurons showed that ACPD (a metabotropic glutamate receptor agonist)-induced 10 Hz subthreshold rhythms were synchronized between pairs of electrically-coupled RT neurons, but not between non-electrically-coupled pairs[182].

  In *lethargic* mice, intracerebroventricular injection of carbenoxolone also decreased the number and total duration of SWDs[183]. In WAG/Rij rats, bilateral injection of carbenoxolone (a gap junction blocker) into RT and VPL (but not in VPM) decreased the number and total duration of SWDs[183]. In rats treated with AY9944 (a cholesterol

synthesis inhibitor that induces atypical absence seizures with 7-8 Hz SWDs chronically), injecting carbenoxolone or 18-α-glycyrrhetinic acid (both gap junction blockers) in the RT nucleus suppressed SWDs[184]. In GAERS rats, injection of mefloquine (a specific blocker of connexin-36) in RT, but not in VB decreased the total duration of SWDs[185]. These results support a role for intra-RT electrical connections in the generation of absence seizures. Nevertheless, there is a short-term suppression of electrical coupling among RT neurons with repetitive stimulation in GAERs rats, but not in non-epileptic controls[185], suggesting the some compensatory mechanism is at play to limit the effect of gap junctions in synchronizing the network.

- **Synaptic $GABA_A$ receptors (α3β3γ2)**

$GABA_A$ receptors are ionotropic receptors that are permeable to chloride and bicarbonate anions[186]. Upon release of GABA in the synapse, activation of synaptic $GABA_A$ receptors induces a fast, phasic IPSC[187]. $GABA_A$ receptors are composed of two α subunits, two β subunits and a variable fifth subunit, most commonly a γ subunit[188]. There are many different variants of each subunit and they are differentially expressed in different regions of the brain[188]. In the thalamus, the α3 subunit and β3 subunit are almost exclusively expressed in the RT nucleus[188].

What is the functional significance of RT neuronal $GABA_A$ receptors in thalamic oscillations *in vitro*? The reversal potential of $GABA_A$ receptors is often above the resting membrane potential of RT neurons, so activation of $GABA_A$ receptors in RT neurons is often *depolarizing*[189]. Nevertheless, in ferret thalamic slices, bath application of bicuculline (a $GABA_A$ receptor blocker) slowed spindle oscillations to 2-4 Hz, increased the number of action potentials per burst in PGN neurons during spindle oscillations from a maximum of 13 to a maximum of 60, increased rebound burst

firing in TC neurons, and increased the amplitude and duration of the EPSP barrages arriving from TC neurons[190–192]. Local application of bicuculline in PGN had a similar effect. In rat thalamic slices, local application of bicuculline in RT, but *not in VB*, slowed and synchronized oscillations[193]. In thalamic slices of transgenic $GABA_A$ β3 subunit knockout mice, whose RT neurons show a decreased amplitude and duration of spontaneous and evoked IPSCs, the oscillations evoked by stimulating corticothalamic fibers were much more synchronous compared to those of control mice[194]. In rat thalamic slices, local application of picrotoxin (a $GABA_A$ receptor blocker) in RT, which generated similar slowed paroxysmal oscillations, increased the burst probability of RT neurons, but not the number of spikes per burst[195]. These results suggest that intra-RT GABAergic connections are probably still inhibitory (which is true as long as the reversal potential is below the activation threshold of LTSs) and is important in limiting RT burst probability.

Conversely, in rat thalamic slices, bath application of clonazepam (a $GABA_A$ receptor agonist) reduced the number of bursts (but not spikes per burst) in RT neurons and shortened the duration of evoked spindle-like oscillations[196]. This still held true when clonazepam was applied in thalamic slices of mice with an α1(H101R) mutation, which rendered the synaptic $GABA_A$ receptor on TC neurons benzodiazepine-insensitive and allowed clonazepam to activate $GABA_A$ receptors on RT neurons selectively[196]. Furthermore, simultaneous intracellular recordings of RT neurons and extracellular recordings of TC neurons showed that clonazepam desynchronized the relative timing of RT bursts to TC neuronal activity[195]. These results further support that intra-RT GABAergic connections are important for limiting RT neuronal syn-

chrony and burst duration, limiting the intensity of recurrent excitation from TC neurons and desynchronizing the thalamic network (see later).

What is the significance of intra-RT inhibition in absence seizures *in vivo*? Single-nucleotide polymorphisms that reduce expression of the $GABA_A$ receptor β3 subunit (note the β3 subunit is specific to RT neurons and not TC neurons) expression, one of which is possibly due to a reduced binding of neuron-specific transcription factor N-Oct-3, are associated with childhood absence epilepsy[34,35]. In GAERS rats, injecting γ-vinyl GABA or muscimol (both $GABA_AR$ agonists) in the RT nucleus suppressed SWDs[197]. The transgenic $GABA_A$ β3 subunit knockout mice mentioned previously display an Angelman syndrome phenotype whose absence seizures are aggravated by carbamazepine, THIP and baclofen (all pro-SWD drugs), and whose interictal spiking and clonic jerks can be suppressed by ethosuximide (an anti-SWD drug)[63]. Conversely, transgenic $GABA_A$ α3 subunit knockout (note the α3 subunit is also specific to RT neurons and not TC neurons) mice, whose RT neurons have a paradoxical, compensatory increase in the $GABA_A$ IPSP amplitudes, showed *in vitro*, a reduced duration of thalamic oscillations evoked by electrically shocking corticothalamic fibers and *in vivo*, a reduced duration and amplitude of γ-butyrolactone (GBL)-induced SWDs[71]. Therefore, intra-RT inhibition appears important for limiting SWDs.

The α3β3γ2 $GABA_A$ receptor is also regulated by diazepam binding inhibitor (DBI), an endogenous benzodiazepine (endozepine). Both *nm1054* mice, in which the DBI gene is knocked out, and *α3(H126R)* mice, in which the $GABA_A$ receptor is rendered insensitive to benzodiazepines, exhibit spontaneous SWDs[198]. DBI comes from astrocytes, as poisoning of glial cells with fluorocitrate reduces the spontaneous IPSC duration in RT neurons, an effect that is absent in *nm1054* mice and *α3(H126R)*

mice[199]. In fact, *in vivo* application of fluorocitrate caused seizures in mice[200]. Therefore, the astrocytic provision of DBI play an important role in enhancing intra-RT inhibition and limiting network synchrony, as discussed above.

RT-TC connections: Electrophysiology, receptors involved and their significance

How can RT-TC GABAergic inhibition be modulated? Immunohistochemical staining studies have shown that TC neurons express synaptic α1β2γ2 $GABA_A$ receptors, extrasynaptic α4β2δ $GABA_A$ receptors and $GABA_B$ receptors[188,201,202]. Similar to that in intra-RT synapses, the concentration of GABA in RT-TC synapses can also be modulated by GABA transporters 1 and 3 expressed in astrocytes surrounding the TC neurons[203]. We will discuss these receptors and transporters in turn:

- **Synaptic $GABA_A$ receptors** (**α1β2γ2**)

  γ2 subunit-containing $GABA_A$ receptors are preferentially located in the synapses[204] and drive fast, "phasic" IPSCs in TC neurons[180,205]. In $GABA_AR$ γ2 floxed mice, focal deletion of synaptic $GABA_A$ receptors from somatosensory TC neurons blocked spontaneous IPSCs as well as monophasic IPSCs evoked by electrical stimulation in the RT nucleus under glutamate receptor blockade[205]. However, burst IPSCs could still be evoked when the glutamate receptor blockade was removed and the TC neurons were patched with high intracellular $[Cl^-]$[205]. In fact, slow cortical oscillations and spindle oscillations persisted in these mice[205]. Furthermore, in thalamic slices of mice with an α3(H126R) mutation, which rendered the synaptic $GABA_A$ receptor on RT neurons benzodiazepine-insensitive, bath application of clonazepam (a $GABA_A$ receptor agonist that now activates only synaptic $GABA_A$ receptors on TC neurons) did not affect spindle-like oscillations evoked by corticothalamic stimulation[196]. These results

suggest that synaptic $GABA_A$ receptors are not essential for the generation of thalamocortical oscillations and that spindle oscillations are likely to be more dependent on the benzodiazepine-insensitive extrasynaptic $GABA_A$ receptors, as discussed next.

- **Extrasynaptic $GABA_A$ receptors (α4β2δ)**

δ subunit-containing $GABA_A$ receptors are expressed in the extrasynaptic or perisynaptic membrane[206–208]. δ subunit-containing $GABA_A$ receptors also have an affinity for GABA 50 times higher than other $GABA_A$ receptors, and they do not desensitize upon the prolonged presence of an agonist, both properties that increase the effectiveness of extrasynaptic activation[209]. Due to the presence of the α4 subunit, extrasynaptic $GABA_A$ receptors in TC neurons are insensitive to benzodiazepines[201,210,211]. In particular, they are activated by neurosteroids, THIP and blocked by Zn^{2+} and gabazine[201,211].

Extrasynaptic $GABA_A$ receptors are thought to be activated by GABA spillover from synapses during periods of intense synaptic release such as RT burst firing, generating a "tonically" active inhibitory current, sensitive to bicuculline, in TC neurons[201,207,211]. Notably, this tonic inhibitory current is absent in RT neurons, which do not express α4 or δ subunits based on histochemical studies[188,201]. This tonic current could influence the excitability and firing mode of TC neurons by regulating their membrane potential[117]. On the other hand, whole cell recordings in acute thalamic slices of transgenic $GABA_AR$ α4 subunit knockout mice showed that, in addition to reduced tonic inhibition, there is also a reduced $GABA_A$ IPSC duration in TC neurons upon RT burst firing[212]. Application of DS2 (an agonist of δ subunit-containing $GABA_A$

receptors) increased $GABA_A$ IPSC duration wild-type mice but not in $GABA_AR$ α4 subunit knockout mice[212]. Therefore, extrasynaptic $GABA_A$ receptors are responsible for the prolongation of phasic IPSPs as well.

What is the significance of extrasynaptic $GABA_A$ receptors? In GAERS rats, injecting γ-vinyl GABA or muscimol (both $GABA_AR$ agonists) in the VB nucleus increased the total duration of SWDs[197]. In transgenic $GABA_AR$ δ subunit knockout mouse, there is reduced tonic inhibition in TC neurons and reduced sensitivity to GBL-induced SWDs[66]. In normal rats, intrathalamic administration of THIP by reverse microdialysis induced ethosuximide-sensitive SWDs[66]. Therefore, extrasynaptic $GABA_A$ receptors are both necessary and sufficient for the generation of SWDs.

- **$GABA_B$ receptors**

$GABA_B$ receptors are metabotropic, G-protein-coupled receptors (GPCRs)[213]. Double immunolabelling with GAD (glutamate decarboxylase, a presynaptic marker for GABAergic synapses) in TC neurons showed that $GABA_B$ receptors are primarily localized extrasynaptically[202,214]. Postsynaptically, $GABA_B$ receptors activates potassium channels such as the Kir3 channel and induce slow IPSCs[213]. In rat thalamic slices, extracellular stimulation of RT neurons evoke a biphasic IPSCs in TC neurons: the fast, $GABA_A$-mediated component was picrotoxin-sensitive, outwardly-rectifying, Cl^- dependent with a reversal potential of about -94 mV and lasted <100 ms; the slow $GABA_B$-mediated component was CGP-35348-sensitive, had a linear conductance, had a reversal potential of about -103 mV and lasted about 300 ms[215].

When do $GABA_B$ receptors in TC neurons get activated? Similar to extrasynaptic $GABA_AR$-mediated IPSCs, $GABA_BR$-mediated IPSCs often require strong stimuli that presumably promote GABA spillover[216–218]. This increase in GABA spillover could

occur during RT neuronal bursting, when the high frequency of GABA release saturates the GABA transporters that normally recycle GABA from the extracellular space, and can be exacerbated by GABA transporter blockade. Indeed, in ferret thalamic slices bathed in bicuculline (a $GABA_A$ receptor blocker), an increase in the stimulation of PGN neurons via local application of glutamate resulted in an increase in the amplitude of CGP-35348-sensitive IPSPs in TC neurons[219]. Therefore, increased GABA spillover could increase the amplitude of $GABA_BR$-mediated IPSCs. Note, however, that increased GABA spillover could also increase the duration of $GABA_BR$-mediated IPSCs without affecting the amplitude, as discussed later[220].

What is the role of $GABA_B$ receptors in thalamic oscillations *in vitro*? In ferret thalamic slices, bath application of saclofen (a $GABA_B$ receptor agonist) did not affect normal spindle oscillations[191,192]. However, local (with a micropipette) or bath application of saclofen completely abolished the bicuculline-induced paroxysmal oscillations discussed previously[191,192], suggesting that $GABA_B$ receptors participate in slow, SWD-like oscillations, but not in normal spindle oscillations. Similarly, in rat thalamic slices, local application of bicuculline in RT, which slowed and synchronized oscillations, increased the amplitude of both $GABA_A$ and $GABA_B$ IPSPs, but *more prominently the latter*, in TC neurons[193]. Conversely, bath application of clonazepam (a $GABA_A$ receptor agonist), which decreased the total duration of oscillations and desynchronized RT neuronal activity, reduced the amplitude of RT-TC $GABA_B$ IPSPs (but not $GABA_A$ IPSPs)[193]. These results indicate that blocking or enhancing intra-RT inhibition could bias RT-TC IPSPs towards a $GABA_BR$-mediated or $GABA_AR$-mediated profile, respectively, and that the former profile is more likely to generate slow, synchronized, SWD-like oscillations. In support of this, in rat thalamic slices, application

of CGP-35348 (after which only $GABA_AR$-mediated IPSCs remain) sped up spindle-like oscillations and but did not affect synchrony, whereas application of picrotoxin (after which only $GABA_BR$-mediated IPSCs remain) slowed oscillations and increased synchrony[221]. Therefore, a major difference between slow, SWD-like oscillations versus normal spindle-like oscillations seems to be a differential activation of $GABA_B$ versus $GABA_A$ receptors. Biasing the RT-TC IPSP towards a $GABA_BR$-mediated profile seems to facilitate the synchronization of thalamocortical oscillations and would potentially exacerbate SWDs[222].

What about the role of $GABA_B$ receptors in SWDs *in vivo*? in GAERS rats, bilateral injections of baclofen (a $GABA_B$ receptor agonist) into the VB or RT nucleus of the thalamus increased spontaneous SWDs in a dose-dependent fashion, whereas injections of CGP35348 (a $GABA_B$ receptor antagonist) into the same sites decreased spontaneous SWDs dose-dependently[223]. Intraperitoneal administration of baclofen in GAERS rats also increased spontaneous SWDs dose-dependently[223]. In normal rats, bilateral injections of baclofen into the VB or RT nucleus of the thalamus generated spontaneous SWDs[223]. These results strongly support a role of $GABA_B$ receptors in the generation or maintenance of SWDs.

However, in WAG/Rij rats, microiontophoretic application of CGP55485A (a $GABA_B$ receptor antagonist) did not significantly alter TC neuronal firing during spontaneous SWDs, arguing against a predominant role $GABA_B$ receptors play in the generation of SWDs[224]. Instead, microiontophoretic application of bicuculline (a $GABA_A$ receptor antagonist) significantly increased the magnitude of TC neuronal firing during spontaneous SWDs, and this increase could be attenuated by further application of CGP55485A[224]. In non-epileptic rats, infusion of bicuculline (a $GABA_A$ receptor

blocker, although also an SK channel blocker as discussed before) directly into the thalamus resulted in 3-Hz synchronous cortical oscillations that was abolished by infusion of CGP35348[225]. Taken together, these results suggest that $GABA_B$ receptors are recruited during SWDs *only after $GABA_A$ receptor inhibition*.

- **GABA transporters 1 and 3**

In the brain, GABA transporters are located on both astrocytes (GAT 1 and GAT 3) and neuronal presynaptic terminals (GAT 1), and serve to clear or reuptake GABA from the synaptic cleft, respectively. One might argue that blockade of GAT 1 in neuronal presynaptic terminals decreases the available pool of GABA for future releases, causing a reduction in GABA inhibition. However, picrotoxin (a $GABA_A$ antagonist)-induced tonic currents were increased and spontaneous IPSCs were prolonged in prefrontal cortical slices of GAT 1 knockout mice[67]. Gabazine (an extrasynaptic $GABA_A$ antagonist)-sensitive tonic currents were also increased in TC neurons of GAT 1 knockout mice[66]. Furthermore, these mice showed increased schizophrenia-like symptoms that were reversed with application of picrotoxin[67]. These results demonstrate that GAT 1 blockade indeed results in an increase in extracellular GABA.

In fact, as opposed to most parts of the brain[226], immunostaining in the thalamus showed strong expression of GABA transporter 1 (GAT 1) and GABA transporter 3 (GAT 3) in astrocytes, but not in neurons[227], speaking against the presence of GATs in neuronal presynaptic terminals. Furthermore, GAT 3 was expressed more robustly than GAT 1 throughout the thalamus[227]. Therefore, the GABA concentration at both RT-TC and intra-RT synapses seems to be regulated by astrocytic GAT1 and GAT3.

What are the functional consequences of GAT 1 and GAT 3 blockade? Under

$GABA_B$ receptor blockade, application of nicopetic acid (a non-selective blocker of GAT 1 and GAT 3) increased the RT-TC IPSC duration in wild-type mice, but not in $GABA_AR$ α4 subunit knockout mice, showing that $GABA_A$ IPSCs could be prolonged by increased GABA spillover and the consequent activation of extrasynaptic $GABA_A$ receptors[212].

Conversely, by bathing an acute thalamic slice in a solution of glutamate and $GABA_A$ receptor blockers, one can isolate the $GABA_B$-mediated IPSCs during GAT 1 and/or GAT 3 blockade. In rat thalamic slices, Beenhakker and Huguenard electrically stimulated RT neurons and recorded the evoked $GABA_B$ IPSCs in a voltage-clamped TC neuron of the VB nucleus[220]. Perfusing locally in VB with a GAT 1 blocker, a GAT 3 blocker, or both, the maximum amplitude and decay time constants of the evoked $GABA_B$ IPSCs were found to change significantly. As shown in Figure 3, GAT 1 blockade increased the IPSC amplitude, but not the duration; GAT 3 blockade increased the IPSC amplitude even more, and also increased the duration[220]. Interestingly, dual GAT 1 and GAT 3 blockade increased the IPSC duration significantly, but the average IPSC amplitude was not affected[220].

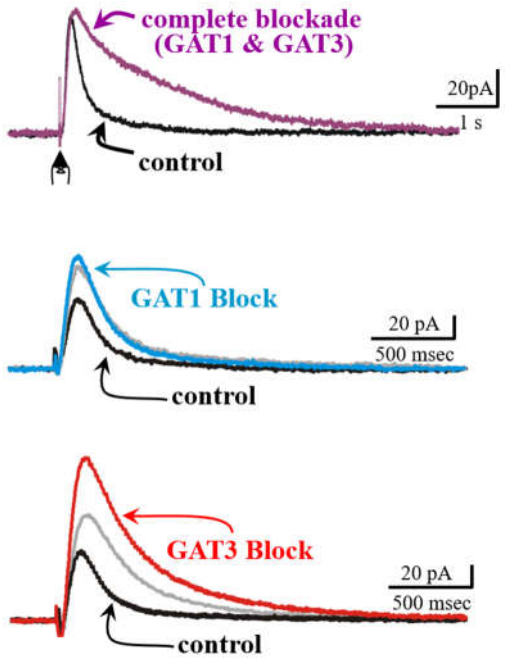

Figure 3. $GABA_B$ IPSCs corresponding to GAT 1 & 3 blockades[220]

To explain such differences, Beenhakker and Huguenard co-stained GAT 1

and GAT 3 particles with either gephyrin (a post-synaptic $GABA_A$ receptor scaffolding protein that serves as a postsynaptic marker for GABAergic synapses) or VGAT (vesicular GABA transporter that serves as a presynaptic marker for GABAergic synapses) particles[220]. They found that, in the thalamus but not in the cortex, GAT 3 expression decayed less spatially from either gephyrin or VGAT particles, demonstrating that GAT 3 is localized farther away from GABAergic synapses than GAT 1.

Beenhakker and Huguenard therefore hypothesized that blocking GAT 3 allowed GABA to diffuse to a greater extent extrasynaptically and resulted in a prolonged recruitment of $GABA_B$ receptors, leading to an increase in IPSC decay time. They supported this hypothesis with a computational model of an RT-TC synapse, along with the surrounding extrasynaptic membrane, that included the spatial distribution of $GABA_B$ receptors, GAT 1 and GAT 3 as observed from immunohistochemical stains. In their simulations, partial GAT 3 blockade that yielded the same amplitude reduction in $GABA_B$ receptor recruitment as complete GAT 1 blockade was shown to preserve an increase in duration, showing that the IPSC amplitude and duration can be independently modulated by differential blockade of GAT 1 versus GAT 3. In summary, GABA transporters 1 and 3 on astrocytes differentially shape the amplitude and decay time of $GABA_B$ IPSCs.

What is the significance of GABA transporters in absence seizures? In humans, the GABA transporter 1 (GAT 1) specific blocker tiagabine, clinically used to treat focal seizures, exacerbates absence seizures and non-convulsive status epilepticus, both generalized forms of epilepsy[228,229]. In rats, GAT 1 expression was found to decrease in the hippocampus 24 hours after pilocarpine (a cholinergic agonist that induces recurrent seizures) administration[230]. In WAG/Rij rats, tiagabine increased in

a dose-dependent way both the number and mean duration of SWDs[231]. In transgenic GAT 1 knockout mice, ethosuximide-sensitive spontaneous SWDs of 4.7-5.7 Hz were observed[66]. Similarly, intrathalamic application of NO-711 (a GAT 1 blocker) by reverse microdialysis in normal Wistar rats induced ethosuximide-sensitive SWDs of 5.0-15.3 Hz[66]. These results suggest that GAT 1 is responsible for limiting the number and duration of SWDs, presumably by limiting the activation of extrasynaptic $GABA_A$ receptors or $GABA_B$ receptors. In fact, in rat thalamic slices, blocking glutamine uptake into neurons, which consequently blocked GABA synthesis in RT neurons, reduced the duration of paroxysmal oscillations[232]. Taken together, these results suggest that the amount of extracellular GABA and the extent of GABA spillover is important in controlling SWDs.

Thalamocortical oscillations

Now I will explain how the basic thalamocortical circuit interact with the distinctive properties of the thalamic neurons to produce normal spindle oscillations and aberrant SWDs.

- Sleep spindles in early slow-wave sleep

  The sleep spindle is an intermittent, waxing and waning 7-15 Hz oscillation that lasts 1-3 s, occurring once every 5-20 s[117]. Sleep spindles are normal rhythms observed on EEG during the early stages of sleep, especially stage II non-REM sleep[233]. Spindle oscillations persisted in the thalamus even after decortication, but did not persist in the cortex after removal of the thalamus[234–237]. Therefore, spindle oscillations are thought to be generated by intra-thalamic networks. In cats, disconnecting TC neurons from RT input abolished spindle oscillations[238], whereas 7-16 Hz spindle

oscillations could still be observed in RT/PGN neurons disconnected from both cortical and thalamic inputs[141]. In sleeping mice, brief (20 ms) optogenetic activation of RT neurons switched TC neuronal activity from tonic to bursting mode, which was sustained for hundreds of milliseconds after stimulation[239]. Burst probability of TC neurons peaked 100-200 ms after stimulation, consistent with the bursts being post-inhibitory rebound bursts[239]. The brief activation of RT neurons also evoked spindles on cortical EEG during NREM sleep, rarely during waking periods and not during REM sleep[239]. These results demonstrated that spindle rhythms are causally paced by RT/PGN neurons during NREM sleep.

In ferret thalamic slices, spontaneous spindle oscillations of 2-4 s duration have been observed to form every 5-20 s[191]. Each spindle consists of RT-TC IPSPs at 6-10 Hz, rebound bursts in TC neurons after every 2nd-4th IPSP, and is followed by a slow and small (1-2.5 mV) afterdepolarization[166]. Simultaneous intracellular recordings of PGN and TC neurons revealed that PGN burst firing was synchronous with a barrage of IPSPs at 6-10 Hz recorded in TC neurons[192]. The IPSPs, through the removal of T channel inactivation (see before), resulted in the generation of rebound calcium-dependent LTSs at 0.5-4 Hz, which were synchronous with peaks of spindle waves in local field recordings[192]. The rebound LTSs of TC neurons often had overriding sodium spikes that were synchronous with a barrage of 3-6 EPSPs at 250-350 Hz recorded in PGN neurons[191]. These EPSPs in PGN neurons then activated an LTS with overriding sodium spikes (12-20) at up to 700 Hz, which started a new oscillation cycle[190]. Comparison with field recordings showed that PGN neurons fire bursts at every 1-2 cycles of a spindle oscillation, whereas TC neurons fire bursts at every 2-3 cycles[190,192]. These spindles were abolished by local (around TC neurons) or bath application of

bicuculline (a $GABA_A$ receptor blocker) or CNQX (an AMPA receptor blocker), but not by saclofen (a $GABA_B$ receptor blocker) or APV (an NMDA receptor blocker). Therefore, IPSPs and EPSPs in spindle oscillations are primarily mediated by $GABA_A$ and AMPA receptors, respectively.

Similar spindle-like oscillations in RT and TC neurons can be evoked in mouse or rat thalamic slices by electrical stimulation of corticothalamic fibers in the internal capsule[221,240]. These oscillations also occur spontaneously in slices of juvenile rats (peak at P12)[221]. After corticothalamic stimulation, recurrent EPSPs in RT neurons were abolished by bath application of bicuculline (a $GABA_A$ receptor blocker), but not by saclofen (a $GABA_B$ receptor blocker)[240]. Conversely, recurrent IPSPs in TC neurons were abolished by bath application of CNQX (an AMPA receptor blocker) and APV (an NMDA receptor blocker)[240]. Indeed, application of either picrotoxin (a $GABA_A$ receptor blocker) or combined CNQX and APV abolished oscillations completely[221]. Therefore, spindle oscillations are generated through reciprocal connections between RT/PGN and TC neurons and the interactions between $GABA_A$R-mediated IPSPs, T-type calcium channels and AMPAR and NMDAR-mediated EPSPs.

How do spindle oscillations propagate? Through divergent TC-RT connections, spindle oscillations can also propagate laterally *in vitro*[241]. Spindle oscillations also propagate to the cortex through thalamocortical projections[242]. In barbiturate-anaesthetized cats, intracellular recordings of cortical neurons in the primary somatosensory cortex showed rhythmic (7-14 Hz) EPSPs that were in phase with spindle waves on EEG[242]. Spindles occurred in phase among TC, RT and cortical neurons, suggesting that corticothalamic feedback in turn drives further thalamic spindles[242]. Simultane-

ous field recordings revealed that spindle oscillations were synchronized across different cortical regions and thalamic regions, even after transection of intracortical synapses via a deep coronal cut[243]. Upon decortication, the thalamic oscillations became less organized. These results support an important role for corticothalamic feedback in maintaining spindle coherence across regions.

However, in naturally sleeping mice, cortical spindles evoked by optogenetic stimulation of RT neurons were not in phase with thalamic activity, suggesting that in non-anaesthetized animals spindle oscillations may not be synchronized across regions[239]. Consistent with this, simultaneous intra-cortical depth EEG recordings in neurosurgical patients showed that spindles are not synchronized across brain regions and may propagate across typical paths[244]. Therefore, sleep spindles are most likely localized thalamocortical oscillations.

- Spike-wave discharges (SWD) or absence seizures

Spike-wave discharges are abnormal, generalized, large amplitude oscillations of 3-6 Hz (6-10 Hz in rodents), lasting 2-30 s, observed on human EEG during absence seizures[117]. In WAG/Rij rats, the mean duration of SWDs is about 5 s at 6 months of age, and the number of SWDs is about 15-20 an hour[245]. As opposed to spindles, which are mostly local rhythms, SWDs are generalized and synchronized across both hemispheres.

As discussed previously, in ferret or rat thalamic slices, bath application of bicuculline (a $GABA_A$ receptor blocker) could transform spindles into paroxysmal 2-4 Hz oscillations, which were followed by a prolonged and small (1-4 mV) afterdepolarization[166]. However, when CGP-35348 (a $GABA_B$ receptor blocker) was also present in the bath solution, local application of bicuculline at both the PGN and the dorsal

LGN (dLGN, where TC neurons reside) suppressed oscillations completely, supporting an essential role of $GABA_B$ IPSPs in the paroxysmal oscillations[219]. Interestingly, both the effects of bicuculline at both the PGN and the dorsal LGN were necessary to transform spindles into paroxysmal oscillations[219]. When bicuculline was applied in the dLGN only, RT inhibition was still intact and the resulting $GABA_B$ IPSP amplitudes were too small. When bicuculline was applied in the PGN only, spindle oscillations were still intact because the shorter $GABA_A$ IPSPs were still present to override any $GABA_B$ IPSP[219]. Therefore, the slow, synchronous oscillations observed in bicuculline treatment likely resulted from a bias of the RT-TC IPSP towards a $GABA_B$R-mediated profile through a combination of two factors: (1) blockade of $GABA_A$ receptors on TC neurons (2) blockade of $GABA_A$ receptors on RT neurons, which suppressed intra-RT inhibition, increased RT burst activity, facilitated GABA spillover and increased activation of $GABA_B$ receptors on TC neurons.

Based on the fact that spindles can be transformed into paroxysmal oscillations of the same frequency as SWDs *in vitro*, and the observation that there is rapid transition from normal to epileptiform activity in absence seizures, many have hypothesized that SWDs may hijack the same circuitry that generates sleep spindles[94]. However, how the transition from normal to abnormal occurs is not fully understood. A magnetic resonance spectroscopy study on an absence epilepsy patient with unilateral spike-wave discharges found increased GABA levels in the hemisphere with SWDs, supporting a role of GABA regulation (by GABA transporters for instance) in absence seizures[246]. Nevertheless, any of the projections, connections, receptors and intrinsic currents in the basic thalamocortical circuit discussed above could potentially be altered to induce the spindle-to-seizure transition. Therefore, there is a need

for computational models to help us understand experimental results, distinguish among different hypotheses, identify important factors and predict effects of potential treatments.

Computational models: Rationale and potential pitfalls

To provide support for hypotheses on the pathophysiology of absence seizures, computational models can be built to try to reproduce features of the SWDs that have been observed experimentally. There are many ways such a computational model can be useful, such as: (1) By reproducing an experimental phenomenon through known equations and parameters, one can determine which parts of a system is *sufficient* for the phenomenon observed; (2) By modifying equations or parameters and analyzing the effect on the experimental phenomenon (sensitivity analysis), one can identify the parts of a system that is *necessary* for the phenomenon observed; (3) By modifying equations or parameters, one can also predict expected outcomes of future experiments or predict the effects of potential treatments.

What are the potential pitfalls to computational modelling? Most experimental phenomena likely involve many more factors than are incorporated in a computational model. Oversimplification may lead to inaccuracy and a wrong interpretation of the experimental phenomenon. On the other hand, inclusion of too many parameters may lead to degeneracy and blur the effect each individual parameter has on the phenomenon.

Computational models of channels and receptors

Channels and receptors are modelled with equations that govern the current *I* (the

output variable) generated by the channel or receptor over time. The current is dependent on the membrane potential *V* (a global state variable) and is usually modelled with either Ohm's law (linear dependence) or the Goldman-Hodgkin-Katz (GHK) current equation (nonlinear dependence, inward or outward-rectifying). The conductance is often modelled with Hodgin and Huxley-type kinetics that include activation and/or inactivation gating variables (multiplicative factors to the maximal conductance) that are voltage dependent and decay with time. As examples, we will discuss how currents of T-type calcium channels (T currents), hyperpolarization-activated nonspecific cation channels (h currents) and $GABA_B$ receptors have been modelled:

- **T-type calcium current (T current)**

  The T-type calcium current (I_T) is often modelled with the GHK current equation and the conductance is with 2 activation gates and 1 inactivation gate (m^2h). The GHK current equation is used because T channels are strongly inward-rectifying and because intracellular $[Ca^{2+}]$ is normally so small that it may be drastically altered with activity. The T current is given by:

$$I_{\mathrm{T}} = I_{\mathrm{Ca}} = \bar{P}_{\mathrm{Ca}} m^2 h G(V, [\mathrm{Ca}]_o, [\mathrm{Ca}]_i)$$

$$G(V, [\mathrm{Ca}]_o, [\mathrm{Ca}]_i) = \frac{Z^2 F^2 V}{RT} \frac{[\mathrm{Ca}]_i - [\mathrm{Ca}]_o e^{-ZFV/RT}}{1 - e^{-ZFV/RT}}$$

  where P_{Ca} is the maximum permeability, $Z = +2$ is the valence of calcium, F is the Faraday's constant, R is the universal gas constant, and T is the temperature of the experiment.

  The intracellular $[Ca^{2+}]$ is modelled to be activity-dependent by first order kinetics, in which calcium accumulates in a submembranal shell-like compartment with depth d and is extruded by a calcium exporter with time constant τ_r:

$$\frac{d[\mathrm{Ca}]_i}{dt} = -\frac{I_{\mathrm{Ca}}}{2Fd} + \frac{([\mathrm{Ca}]_\infty - [\mathrm{Ca}]_i)}{\tau_r}$$

where *F* is Faraday's constant and $[Ca^{2+}]_\infty$ is the steady-state calcium concentration.

The activation variable *m(t, V)* and inactivation variable *h(t, V)* are governed by first order kinetics with the steady state values $m_\infty(V)$, $h_\infty(V)$ and the time constants $\tau_m(V)$, $\tau_h(V)$:

$$\frac{dm}{dt} = \frac{m_\infty - m}{\tau_m}, \quad \frac{dh}{dt} = \frac{h_\infty - h}{\tau_h}$$

The voltage dependence of the steady state values and time constants of activation and inactivation gating variables are fitted to values obtained from two-step voltage clamp experiments, and the resulting curves from one study using rat TC neurons are given below[247]:

$$m_\infty = \frac{1}{1 + e^{(V+57-shift_m)/(-6.2slope_m)}},$$

$$h_\infty = \frac{1}{1 + e^{(V+81-shift_h)/(4.0slope_h)}}$$

$$\tau_m = \frac{1}{\Phi_m slope_m}(0.612 + \frac{1}{e^{(V+132-shift_m)/-16.7} + e^{(V+16.8-shift_m)/18.2}})$$

$$\text{For } V - shift_h < -80\,\mathrm{mV},$$

$$\tau_h = \frac{1}{\Phi_h slope_h} e^{(V+467-shift_h)/66.6}, \quad \Phi_m = Q_{10,m}^{(T-23)/10}$$

$$\text{For } V - shift_h \geq -80\,\mathrm{mV},$$

$$\tau_h = \frac{1}{\Phi_h slope_h}(28 + e^{(V+22-shift_h)/(-10.5)}),$$

$$\Phi_h = Q_{10,h}^{(T-23)/10}$$

where $Q_{10,m}$ = 3.6 and $Q_{10,h}$ =2.5 are temperature correction factors determined from experiments that measured the temperature-dependence of activation and inactivation time constants[248], and $shift_m$, $shift_h$, $slope_m$, $slope_h$ are parameters that can shift the voltages of half-activation ($V_{1/2}$) and the slope of voltage dependence (1/k) when the model is used to fit new experimental data, as these parameters may potentially change across species or across different neuronal types.

- **Hyperpolarization-activated nonspecific cationic current (h current)**

The h current (I_h) is permeable to both sodium and potassium ions with a permeability ratio of about K^+:Na^+ = 3:1-4:1[249]. Based on physiological concentrations of sodium and potassium, the GHK voltage equation yields a reversal potential of about -24 to -32 mV. The h current is often modelled with Ohm's law and the conductance is modelled with 1 activation gate, since it doesn't inactivate:

$$I_{\mathrm{h}} = \bar{g}_{\mathrm{h}} m (V - E_{\mathrm{h}})$$

where g_h is the maximum conductance and the activation variable $m(t, V)$ is governed by first order kinetics with the steady state value $m_\infty(V)$ and the time constants $\tau_m(V)$:

$$\frac{dm}{dt} = \frac{m_\infty - m}{\tau_m}, \quad m_\infty = \frac{1}{1 + e^{(V+82-shift_m)/5.5}}$$

$$\tau_m = \frac{1}{\Phi_m(0.0008 + (3.5 \times 10^{-6})e^{-0.05787(V-shift_m)} + e^{-1.87+0.0701(V-shift_m)})}$$

$$\Phi_m = Q_{10,m}^{(T-34)/10}$$

Here, the curves were fitted to experimental data from a study using mouse TC neurons[250], and $Q_{10,m}$ = 4.0[169].

- **$GABA_B$ receptors**

There are many ways for modelling $GABA_B$ receptors. Since $GABA_B$ receptors activate potassium channels, experimental measurements for the reversal potential ranged from E_{rev} = -117 mV to -103 mV for TC neurons[215,251]. The modelling of $GABA_B$ receptors can be simplified by using the stereotypical IPSP conductance profiles that were experimentally recorded by Beenhakker and Huguenard under different pharmacological conditions[220]. The $GABA_B$ IPSP current (I_{GABAB}) is governed by Ohm's law:

$$I_{\mathrm{GABA_B}} = g_{\mathrm{GABA_B}}(V - E_{\mathrm{rev}})$$

and the conductance g_{GABAB} is governed by an equation of the form

$$g_{\mathrm{GABA_B}} = A(1 - R_{\mathrm{on}})^p(wR_{\mathrm{off,fast}} + (1-w)R_{\mathrm{off,slow}})$$

where A is the maximum amplitude, R_{on}, $R_{off,fast}$, $R_{off,slow}$ are the rise, fast decay and slow decay variables, p is the cooperativity, and w is the weight for the fast decay variable. These variables are governed by first-order kinetics and are updated whenever a synaptic event arrives:

$$\frac{dR_{\mathrm{off,fast}}}{dt} = \frac{-R_{\mathrm{off,fast}}}{T_{\mathrm{off,fast}}/\Phi}, \quad \frac{dR_{\mathrm{off,slow}}}{dt} = \frac{-R_{\mathrm{off,slow}}}{T_{\mathrm{off,slow}}/\Phi},$$

$$\frac{dR_{\mathrm{on}}}{dt} = \frac{-R_{\mathrm{on}}}{T_{\mathrm{on}}/\Phi}$$

$$R_{\mathrm{off,fast}} = R_{\mathrm{off,fast}} + \frac{weight}{N_{\mathrm{inputs}}},$$

$$R_{\mathrm{off,slow}} = R_{\mathrm{off,slow}} + \frac{weight}{N_{\mathrm{inputs}}} R_{\mathrm{on}} = R_{\mathrm{on}} + \frac{weight}{N_{\mathrm{inputs}}}$$

What have we learned from modelling channels or receptors? Let's take GABA synaptic transmission as an example. A model of GABA synaptic transmission that incorporated GABA release, diffusion and reuptake assumed a nonlinear activation profile for $GABA_B$ receptors based on cooperative binding of 4 G proteins[252]. When placing this model receptor in a model TC neuron (see later) innervated by 5 RT neurons (convergence), this model successfully reproduced the experimental finding that low intensity RT bursting (for instance during spindle oscillations) evoked a $GABA_A$R-dominated IPSP, whereas high intensity RT bursting (for instance during SWDs) evoked a $GABA_B$R-dominated IPSP[252]. This model demonstrated that activation of $GABA_B$ receptors is likely cooperative (may involve 4 intermediates binding together) and that GABA spillover in the synapses is indeed important for activating $GABA_B$ receptors and biasing the RT-TC IPSP profile towards $GABA_B$-mediated IPSPs. Another modelling study of the GABAergic synapse that demonstrated the effect of GAT blockers on GABAB IPSP profiles was discussed previously[220].

Computational models of neurons

Neurons are modelled with equations that govern the voltage (the output variable) generated by various intrinsic and extrinsic currents over time. The plasma membrane is modelled as a capacitor that can be charged by various parallel currents. Soma, dendrites and axons of neurons can be broken up into cylindrical compartments that are parallel RC circuits linked together by resistors (for axial resistance). The compartmentalization could be as complicated as a detailed multi-compartment model generated from morphological reconstruction of biocytin-filled real neurons and as simple as a single-compartment model. Each compartment could also be divided into sections (with a computing node in each section) so that the spatial variation over a compartment could be modelled and the

cable equation could be more closely approximated. The actual number of compartments and computing nodes used will depend on the level of detail needed for the particular experimental phenomenon to be modelled. For instance, in a three-compartment model with a configuration given by soma-dend1-dend2, the governing differential equation for the voltage in the dend1 compartment would be given by:

$$\begin{aligned} & C_m \frac{dV_{\mathrm{dend1}}}{dt} \\ & = -g_{\mathrm{L}}(V_{\mathrm{dend1}} - E_{\mathrm{L}}) - I_{\mathrm{T}} - I_{\mathrm{h}} - I_{\mathrm{A}} - I_{\mathrm{Kir}} - I_{\mathrm{NaP}} \\ & - \frac{V_{\mathrm{dend1}} - V_{\mathrm{soma}}}{R_a(L_{\mathrm{soma}}/(\pi d_{\mathrm{soma}}^2) + L_{\mathrm{dend1}}/(\pi d_{\mathrm{dend1}}^2))} \\ & - \frac{V_{\mathrm{dend1}} - V_{\mathrm{dend2}}}{R_a(L_{\mathrm{dend1}}/(\pi d_{\mathrm{dend1}}^2) + L_{\mathrm{dend2}}/(\pi d_{\mathrm{dend2}}^2))} - I_{\mathrm{GABA_B}} \end{aligned}$$

where C_m is the specific membrane capacitance, R_a is the axial resistivity, g_L is the leak channel conductance, E_L is the leak channel reversal potential, and I_T, I_h, I_A, I_{Kir}, I_{NaP}, I_{GABAB} are intrinsic currents present in the dend1 compartment.

What have we learned from single neuron models? I will discuss two examples:

(1) A single-compartment model of a TC neuron that included seven intrinsic conductances quantified the relative contribution of each channel to the resting membrane potential[250]. The model reproduced the behavior of TC neurons such as a switch from a tonic firing mode to an oscillatory bursting mode as the membrane potential hyperpolarizes[250]. Through sensitivity analysis, the model also determined many possible parameter alterations (e.g., increasing the permeability of T channels or decreasing the conductance of A-type potassium channels) that could allow such a switch to occur[250].

(2) Comparison of a detailed model, a 3-compartment model and a single-compartment model of an RT neuron demonstrated that a dendritic distribution of T channels is

necessary to reproduce the characteristic accelerando-decelerando firing pattern[253]. A higher T channel density in distal versus proximal dendrites was also necessary to reconcile the differences of RT neuron response to a hyperpolarizing current *in vivo* versus *in vitro* and to reproduce the all-or-none bursting property of RT neurons[253]. This model thus predicted a distal distribution of T channels in RT neurons, which was later confirmed by further experiments[144,147]. Similar model comparison for a TC neuron also demonstrated that a distal distribution of T channels is necessary to recapitulate the much decreased T current amplitude and lack of bursting in dissociated TC neurons[254]. Indeed, using calcium imaging and simultaneous soma and dendritic electrical recordings, a high contribution of T currents in dendrites versus soma has been experimentally confirmed[255–257].

Computational models of networks

Networks are modelled by linking the membrane potentials of each presynaptic model neuron to currents injected into the post-synaptic model neuron upon the initiation of synaptic events, which are simply modelled to be dependent on a certain activation threshold.

What intra-thalamic network models have been established and what have we learned from these models? A two-layer, one-dimensional network model of single-compartment TC and RT neurons that incorporated the basic thalamic circuit and intrinsic currents discussed above (I_T, I_h in TC neurons, I_{Ts} and I_{ahp} in RT neurons) successfully reproduced both spindle oscillations and bicuculline-induced paroxysmal oscillations that propagated as observed *in vitro*[173]. The model gave great support to the hypothesized mechanisms of spindle generation (interaction between the circuitry and T currents) and the

differential activation of $GABA_A$ versus $GABA_B$ receptors in spindles versus paroxysmal oscillations, as discussed above[173]. The waning phase of the spindle wave was also successfully reproduced by assuming an activity-dependent upregulation of I_h[173]. A similar intra-thalamic network model independently reproduced propagating spindle oscillations, but also reproduced the lack of change in spindle oscillations upon $GABA_B$ receptor blockade and the persistence of intrinsic oscillations in the isolated RT nucleus *in vitro*[258]. Finally, an intra-thalamic network model that selectively knocked-out or reduced intra-RT GABAergic connections showed an increased duration and synchrony of oscillations, supporting a role for intra-RT inhibition in the desynchronization of network activity[195,259].

What thalamocortical network models have been established and what have we learned from these models? A four-layer, one-dimensional network model of single-compartment cortical pyramidal neurons, cortical interneurons, TC neurons, and RT neurons that incorporated the basic thalamocortical circuit and intrinsic currents successfully generated patterns of synchronous oscillations similar to spindle oscillations observed *in vivo*[260]. Similar to the intra-thalamic network model, I_h was essential in the thalamocortical model for setting the refractory period[260]. A follow-up modelling study using the same network generated ~4 Hz synchronous oscillations by blocking $GABA_A$ inhibition in the thalamus and generated ~3 Hz highly synchronous oscillations by blocking $GABA_A$ inhibition in the cortex[261]. Local field potentials were also modelled, and spike-and-wave complexes could be reproduced from summing the post-synaptic currents of cortical neurons after introducing bursts of spikes in cortical neurons[261]. Sensitivity analysis revealed that the “spike component” came from EPSPs mediated through AMPA/NMDA receptors and that the “wave component” came from IPSPs mediated through $GABA_A$ receptors (early

upward deflection) and $GABA_B$ receptors (late downward deflection)[261]. Strengthened corticothalamic input at 3 Hz, but not at 10 Hz, could entrain a two-by-two thalamic network to produce oscillations[261]. A gradual reduction of intracortical inhibition in the model gradually transformed spindle waves to spike-and-wave complexes (slowing the period and increasing the amplitude of field potentials)[261]. Therefore, the model supported the cortical focus theory of SWD generation in which a strengthened corticothalamic feedback increased RT bursting, inducing $GABA_B$ receptor-mediated IPSPs in TC neurons, prolonging and strengthening the RT-TC IPSPs. The prolongation of RT-TC IPSPs prolongs the oscillation period to ~300 ms (3 Hz), whereas the strengthening of RT-TC IPSP increases rebound bursting in TC neurons, which then initiates the next oscillation cycle by providing strong thalamocortical excitation back to cortical neurons[261].

Research goals

In summary, prior research has pinpointed the intra-thalamic network as the core circuitry that maintains absence seizures. Through experimental and computational approaches, a shift from $GABA_A$ to $GABA_B$ receptor-mediated inhibition appears to be responsible for the pathological shift from spindles to spike-wave discharges on EEG, or from spindle-like oscillations to paroxysmal epileptiform oscillations in acute thalamic slices. Each oscillation cycle appears to be initiated by thalamocortical rebound bursting mediated by T-type calcium channels. Early electrophysiological studies using current steps and ramps have established some links between the amplitude or rate of inhibition with T-type calcium channel activation[159,262,263]. Nevertheless, the temporal interplay between *physiological* forms of inhibition (such as $GABA_B$ receptor-mediated IPSCs) and T-type calcium channel activation has not been well understood.

I therefore set out to answer the following research questions: (1) To determine the influence of distinct physiological forms of inhibition on network-level oscillations; (2) To determine the influence of distinct physiological forms of inhibition on thalamocortical rebound bursting; (3) To understand mechanistically how physiological forms of inhibition control rebound bursting.

Chapter 2: Nonlinearities between inhibition and T-type calcium channel activity bidirectionally regulate thalamic oscillations

Introduction

Neural circuits rely on a combination of intrinsic cellular properties and synaptic connections to generate large-scale electrical oscillations that drive behavior[264–267]. Following membrane hyperpolarization, such as that produced by synaptic inhibition, cortically-projecting neurons of the thalamus [i.e. thalamocortical (TC) neurons] produce brief bursts of action potentials[159], a cellular property that maintains both sleep-related and seizure-related oscillations[268,267,94]. Several studies have shown that CaV3.1 T-type calcium channels (T channels) sustain post-inhibitory rebound bursts in thalamocortical neurons by producing a relatively prolonged calcium-dependent, low-threshold spike[69,269,163]. These channels require membrane depolarization to open and hyperpolarization to recover[248]. Hyperpolarization-dependent recovery involves the removal of T channel inactivation (i.e. *de-inactivation*). As T channels are largely inactivated at resting membrane potentials, membrane hyperpolarization is necessary for robust rebound bursting[159,248]. While controlled voltage-clamp experiments have informed our understanding of how neuronal membrane potential dynamics can affect T channel opening[263], we still know little regarding channel behavior during physiological forms of synaptic inhibition.

Reticular thalamic (RT) neurons serve as the main source of inhibitory, GABAergic

input to thalamocortical neurons, especially in rodents[270,116]. Thalamocortical neurons express synaptic $\alpha_1\beta_2\gamma_2$ $GABA_A$ receptors, and two types of extrasynaptic receptors: $GABA_A$ ($\alpha_4\beta_2\delta$) and $GABA_B$[188,202,201]. Studies have shown that modulation of *synaptic* $GABA_A$ receptors between RT and TC neurons has little effect on thalamocortical oscillations[196,205]. In contrast, *extrasynaptic* receptors have been implicated in thalamocortical seizures, both for $GABA_A$[66] and $GABA_B$[223,271,272] receptors. Prior experimental and computational work has demonstrated that a shift from $GABA_A$ receptor-mediated to $GABA_B$ receptor-mediated inhibition at the RT-TC synapse transforms oscillations from a 10 Hz, sparse, spindle-like activity to a 3 Hz, hyper-synchronized, seizure-like state[191,173,261,273].

GABA transporters (GATs) powerfully control the activation of $GABA_B$ receptors[220]. GAT1 and GAT3 represent the primary GABA transporters expressed in the brain and normally recycle GABA from the extrasynaptic space, thereby regulating GABA spillover from the synapse and the activation of extrasynaptic $GABA_A$ and $GABA_B$ receptors[66,218]. In the thalamus, the more abundant transporter, GAT3, is localized farther away from synapses than GAT1[227,220]. Consequently, specific GAT1 blockade results only in an increase in the amplitude of the $GABA_B$ IPSC, reflecting increases in GABA concentration near the synapse. In contrast, specific GAT3 blockade results in an increase in both amplitude and decay of the $GABA_B$-mediated inhibitory post-synaptic current ($GABA_B$ IPSC), as GABA is allowed to diffuse far from the synapse where there is an abundance of $GABA_B$ receptors[220]. On the other hand, dual GAT1 and GAT3 blockade results in a roughly 10-fold increase in the decay time constant and a 5-fold increase in the area under the curve of the $GABA_B$ IPSC. These findings were replicated in a diffusion-based computational model[220].

In this study, we investigate the consequences of physiologically-relevant $GABA_B$

receptor-mediated inhibition observed during different combinations of GABA transporter blockade: control, GAT1 blockade, GAT3 blockade and dual GAT1+GAT3 blockade[220]. As absence seizures are dependent on $GABA_B$ receptor signaling, we hypothesized that GAT blockade would regulate both thalamocortical neuron rebound bursting and network-level thalamic oscillations. We examine the effects of different $GABA_B$ receptor activation waveforms on both absence-seizure-like thalamic oscillations and single thalamocortical neuron responses. We first use pharmacological manipulations to demonstrate that individual GAT1 or GAT3 blockade prolongs seizure-like oscillations, but that dual GAT1+GAT3 blockade surprisingly abolishes oscillations. Next, we apply physiological $GABA_B$ IPSC waveforms corresponding to each pharmacological condition to single thalamocortical neurons with dynamic clamp and demonstrate that individual GAT1 or GAT3 blockade increases rebound burst probability, but that dual GAT1+GAT3 blockade suppresses it. We then build computational model neurons to explore how the differential $GABA_B$ IPSC modulation affects TC responses and discover that differential T channel gating dynamics are responsible for those differences. Finally, we build computational model thalamic networks to determine how the differential effects of GAT blockade influence thalamic oscillations and to probe for pro- and anti-epileptic mechanisms. Through these experimental and computational approaches, we identify how $GABA_B$-mediated inhibition across both voltage and time dimensions regulates T channel activity and seizure-like oscillations.

Results

Thalamic oscillations

To evaluate the contribution of GABA transporters to thalamic network activity in the context of $GABA_B$ receptor-mediated inhibition, we used a standard, acute rat brain

slice model in which electrical oscillations are evoked by extracellular stimulation of the synaptic inputs to the reticular thalamic nucleus in the presence of the $GABA_A$ receptor blocker bicuculline[215,221,274]. We evoked oscillations at intervals producing no rundown [once per minute[221]] and monitored neuronal activity with extracellular multiunit electrodes placed within the ventrobasal complex of the thalamus. By detecting evoked bursts, we found that oscillations last between 2-13 seconds at baseline (Figure 1A). The autocorrelogram of binned spike times revealed pronounced secondary peaks at multiples of approximately 500 ms (Figure 1A). After recording evoked oscillations for 20 minutes under baseline conditions, we then applied one of four experimental solutions to the perfusate (Figure 1B). Experimental solutions consisted of: (1) a control solution identical to the baseline solution, (2) 4 μM NO-711, a specific GAT1 blocker[275], (3) 100 μM SNAP-5114, a specific GAT3 blocker[276], or (4) a combination of 4 μM NO-711 and 100 μM SNAP-5114. These blocker concentrations achieve full GAT blockade[220]. Experimental solutions were applied for 40 minutes, and then washed out over another 20 minutes.

When individually applied, either GAT1 or GAT3 blockade prolonged oscillations (Figure 1C), consistent with the absence seizure exacerbation seen with a clinically used GAT1 blocker, tiagabine [228,229,277]. We measured the duration of each evoked oscillation, then computed the average duration of the last 5 stable oscillations in baseline and experimental solutions (Figure 1D). Relative to baseline, individual GAT1 or GAT3 blockade increased oscillation duration by 36% ($n = 8$ slices from 5 animals, $p = 0.0027$) and 99%, ($n = 7$ slices from 5 animals, $p = 0.0076$), respectively. We also evaluated the effects of individual GAT1 or GAT3 blockade on the period of evoked oscillations (Figure 1E). Relative to baseline, GAT1 or GAT3 blockade increased the oscillation period by 13% ($n = 8$ slices from 5 animals, $p = 0.0021$) and 32% ($n = 7$ slices from 5 animals, $p = 0.0050$), respectively.

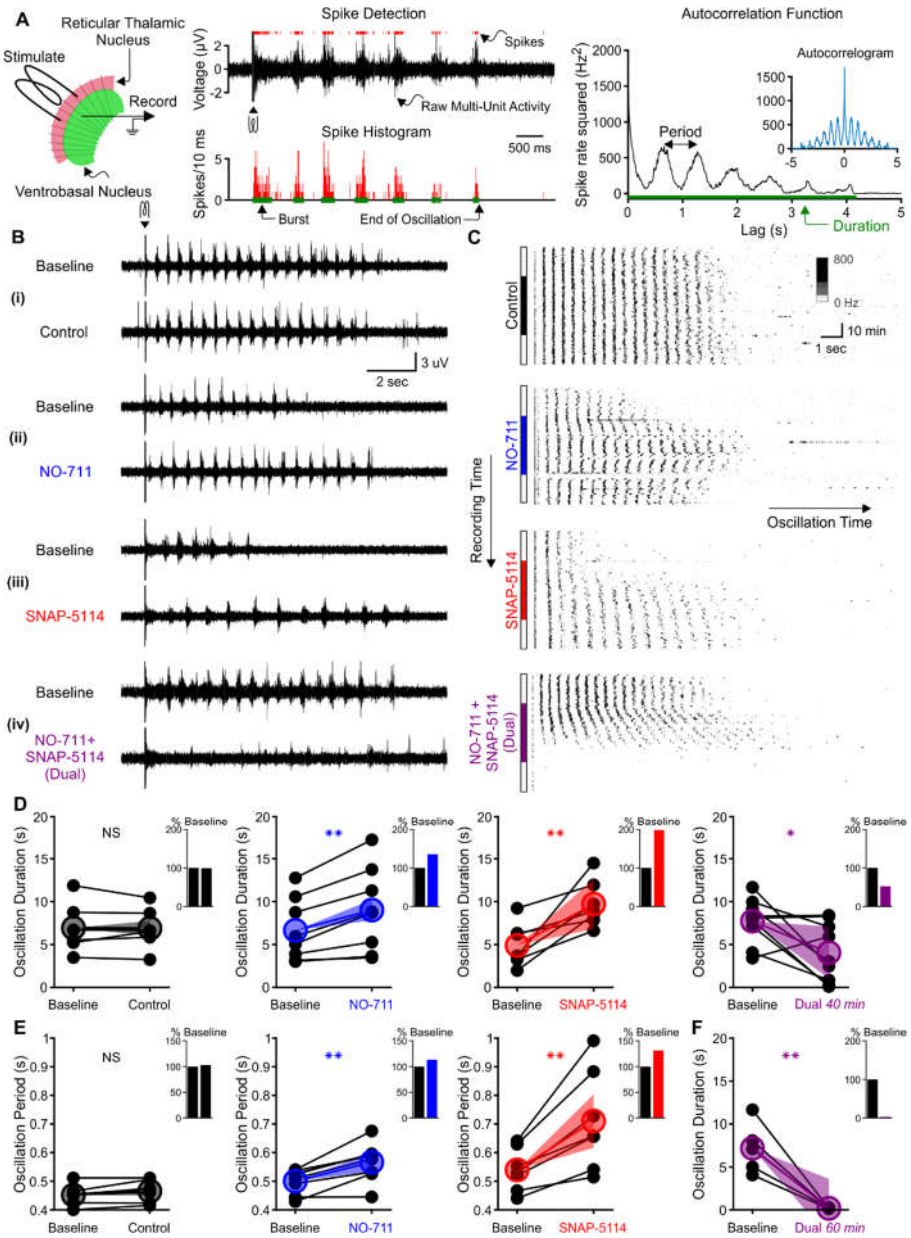

Figure 1. Individual GAT1 or GAT3 blockade strengthens thalamic oscillations, but dual GAT1+GAT3 blockade abolishes oscillations.
(**A**) Slice recording setup and sample analysis. Acute thalamic slices were bathed in bicuculline to block $GABA_A$ receptors. A brief voltage stimulus (0.5 ms, 10 V) was applied with a bipolar electrode placed in either the reticular thalamic nucleus or the adjacent internal capsule to evoke epileptiform oscillations recorded extracellularly in the ventrobasal complex. Spikes were detected, binned, and grouped into bursts. The oscillation duration was measured from the spike histogram and the oscillation period was computed from the autocorrelation function of binned spikes. (**B**) Example evoked epileptiform oscillations at baseline and 40 minutes after perfusing with (i) control (no drug added), (ii) 4 μM NO-711 (GAT1 blocker), (iii) 100 μM SNAP-5114 (GAT3 blocker) or (iv) dual 4 μM NO-711+100 μM SNAP-5114. (**C**) Example PSTHs over the entire course of a single control, GAT1-, GAT3-, and dual-block experiment. Oscillations were evoked every 60 seconds, but only the first 17 seconds after stimulation are shown. Drugs were perfused for 40 minutes after 20 minutes of baseline, followed by 20 minutes of washout. (**D-F**) Oscillation measures for all slices. Colored circles denote the mean value, colored lines denote the mean change; and shaded areas denote the 95% confidence intervals for the mean change. (**D**) Oscillation duration did not change following control perfusion, but increased following NO-711 or SNAP-5114 perfusion. Dual NO-711+SNAP-5114 perfusion reduced oscillation duration (* $p < 0.05$, ** $p < 0.01$, paired-sample *t*-test). Inset shows mean change relative to baseline. (**E**) Oscillation period did not change following control perfusion and lengthened following NO-711 or SNAP-5114 perfusion (** $p < 0.01$, paired-sample *t*-test). (**F**) After 60 minutes of dual NO-711 + SNAP-5114 perfusion, oscillations were abolished in all slices (** $p < 0.01$, paired-sample *t*-test).

Collectively, the effects of GAT blockade on oscillation properties generally agreed with the previously reported actions of GAT blockers on isolated $GABA_B$ receptor-mediated IPSCs. That is, the 1.4-fold and 2-fold increase in oscillation duration corresponds roughly to the reported 1.5-fold and 2.2-fold increase in $GABA_B$ IPSC amplitude produced by GAT1 or GAT3 blockade, respectively[220]. Additionally, GAT3 blockade significantly prolonged oscillation period, while the effect for GAT1 blockade was modest, consistent with reported effects on isolated $GABA_B$ IPSC decay[220].

Surprisingly, the effects of NO-711 and SNAP-5114 co-perfusion on evoked oscillations were not additive. Rather than prolonging evoked oscillations, dual GAT1+GAT3 blockade ultimately *eliminated* oscillations. Following a brief prolongation during the early phases of drug perfusion (see Figure 1C), dual GAT1+GAT3 blockade eventually decreased oscillation duration by 48% (Figure 1D, n = 9 slices from 4 animals, p = 0.026; here and in all results, percentages refer to relative change from control conditions). As the effects of dual blockade on oscillation duration did not appear to reach a steady state by 40 minutes, we extended the drug application to 60 minutes in a subset of experiments. For those slices, dual GAT1+GAT3 blockade invariably abolished oscillations (Figure 1F, n = 5 slices from 3 animals, p = 0.0062).

In summary, the observed effects of individual GAT1 or GAT3 blockade on oscillation duration and period generally reflect the actions the individual blockers have on $GABA_B$ receptor-mediated IPSCs isolated from thalamocortical neurons. GAT blockade-dependent increases in IPSC amplitude were associated with increased strength of oscillation, as measured by duration. However, the effects of dual GAT1+GAT3 blockade on oscillation duration did not reflect the additive effects of combined blockade on $GABA_B$ IPSCs[220]. To better understand the discrepancy between GAT regulation of IPSCs and GAT

regulation of thalamic oscillations, we next examined how IPSC amplitude and kinetics regulate the activity of single thalamocortical neurons.

Single neuron recordings

We investigated the effects of GAT-modulated, $GABA_B$ receptor-mediated currents on thalamocortical neuron rebound bursting, as this property is likely critical for the initiation of each successive cycle of an evoked oscillation[191,215,240]. Experimentally evoked $GABA_B$ receptor-mediated IPSCs isolated in acute thalamic slices vary considerably in amplitude[220], likely reflecting differences in synaptic activation of reticular thalamic neurons by the electrical stimulus. We therefore utilized an alternative approach to systematically examine the effects of GAT blockade on the firing properties of thalamocortical neurons: dynamic clamp[278,279]. We used $GABA_B$ receptor-mediated IPSC waveforms isolated under voltage clamp during each pharmacological condition (control, GAT1 blockade, GAT3 blockade, dual GAT1+GAT3 blockade) as conductance waveform commands applied to single thalamocortical neurons (Figure 2A). We refer to these dynamic clamp-mediated conductance waveforms as *d*IPSCs. We applied each *d*IPSC pharmacological condition (*d*Control, *d*GAT1-Block, *d*GAT3-Block, *d*Dual-Block; Figure 2B) to each recorded thalamocortical neuron.

Since neurons likely receive variable numbers of inhibitory inputs, we scaled the conductance waveform amplitudes for each pharmacological *d*IPSC by 25%, 50%, 100%, 200%, 400% and 800%, yielding 24 possible *d*IPSC waveforms (i.e. 4 pharmacological conditions x 6 amplitude scales). Additionally, we delivered each of the 24 waveforms at three approximate holding potentials: -60 mV, -65 mV or -70 mV. Five non-consecutive repetitions were performed for each *d*IPSC waveform and holding potential condition.

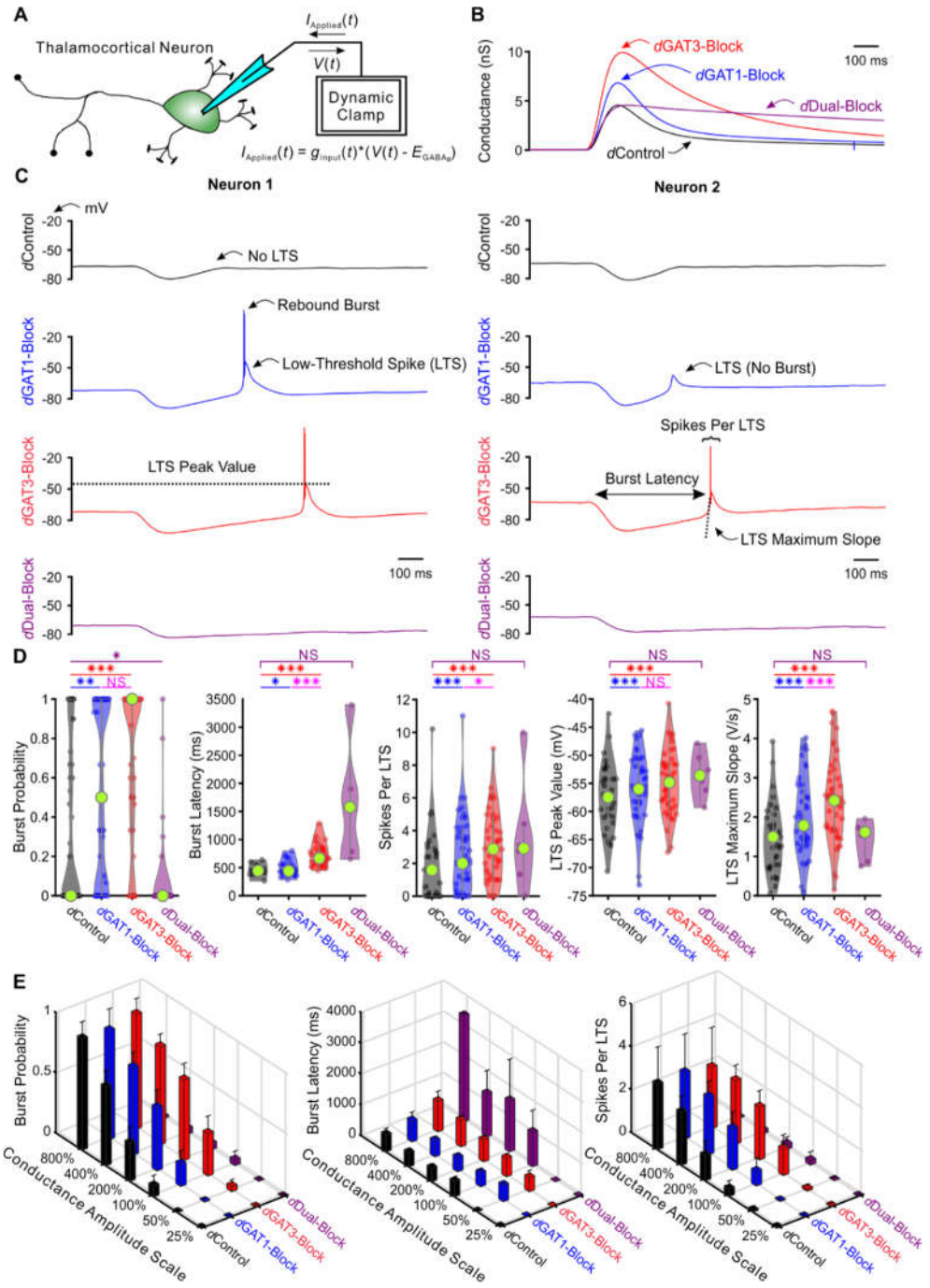

Figure 2. Post-inhibitory, low-threshold rebound spikes and bursts in thalamocortical neurons are bidirectionally modulated by $GABA_B$ receptor-mediated conductance waveforms.
(**A**) Dynamic clamp setup. A thalamocortical neuron was patched in the whole-cell configuration. The applied current was computed from the instantaneous voltage and a command conductance waveform over time to simulate $GABA_B$ receptor activation. (**B**) Command $GABA_B$ receptor conductance waveforms (*d*IPSCs, amplitudes scaled by 200%) that emulated different GAT blockade conditions based on $GABA_B$ IPSCs isolated with voltage clamp [220]. (**C**) Sample voltage responses of two neurons to the four different *d*IPSCs shown in (B). Annotations are for measures in (D) and (E). (**D**) Distributions of post-inhibitory low-threshold rebound spike or burst measures over all 47 recorded neurons across *d*IPSCs shown in (B). Relative to *d*Control responses, rebound burst probability increased following either *d*GAT1- or *d*GAT3-Block, but decreased following *d*Dual-Block (* $p < 0.05$, ** $p < 0.01$, *** $p < 0.001$, Friedman's test for burst probability, repeated-measures ANOVA otherwise). (**E**) Mean LTS or burst measures over all 47 recorded neurons, across 4 different *d*IPSC waveforms and 6 different conductance amplitude scales. Error bars denote 95% confidence intervals.

Figure 2C shows example responses to *d*IPSCs scaled by 200% delivered with dynamic clamp. Post-inhibitory, low-threshold calcium spikes (LTS) often followed each *d*IPSC, with sodium-dependent action potentials often crowning each LTS. Herein, *LTS* refers to the slow, broad (~50 ms) event following inhibition. *Burst*, on the other hand, specifically refers to the collection of action potentials crowning the LTS. We quantified several properties of each post-inhibitory LTS and burst in response to each *d*IPSC, including the probability of occurrence and the latency from *d*IPSC onset. We also computed LTS features such as peak voltage value, maximum rising slope and the number of spikes per LTS, averaged across trials for each neuron.

We first examined LTS and burst probability distributions over all recorded neurons following delivery of *d*IPSCs (LTS: not shown, burst: Figure 2D, 2E). Considering only those *d*IPSCs scaled by 200% (Figure 2D), relative to *d*Control responses, LTS and burst probabilities were higher following either *d*GAT1-Block (n = 47 cells, LTS: +26%, p = 0.0080, burst: +63%, p = 0.0018) or *d*GAT3-Block (n = 47 cells, LTS: +39%, p = 0.0015, burst: +106%, p = 1.7×10^{-7}), but lower following *d*Dual-Block (n = 47 cells, LTS: -88%, p = 4.8×10^{-6}, burst: -82%, p = 0.030). We observed the same trend across pharmacological conditions for all other conductance scales (LTS: not shown, burst: Figure 2E). Not surprisingly, increasing the conductance scale produced an increase in LTS and burst probability for either the *d*Control, *d*GAT1-Block or the *d*GAT3-Block condition. However, both probabilities were consistently very low, below 6%, across all conductance scales following *d*Dual-Block IPSCs. These changes in thalamocortical neuron rebound burst probability parallel the prolonged oscillation duration observed following individual GAT1 or GAT3 blockade, and the decrease in oscillation duration following dual GAT1+GAT3 blockade (Figure 1D).

Next, we examined distributions of average LTS and burst latencies over neurons

responsive to *d*IPSCs (LTS: not shown, burst: Figure 2D, 2E). We restricted this analysis to *d*GAT1- and *d*GAT3-Block IPSCs because the *d*Dual-Block IPSC did not reliably evoke LTSs. Considering *d*IPSCs scaled by 200% (Figure 2D), relative to *d*Control responses, average LTS latency was not significantly different following *d*GAT1-Block (n = 32 cells, p = 0.97), while average burst latency was modestly prolonged (+4.6%, n = 21 cells, p = 0.034). In contrast, *d*GAT3-Block IPSCs significantly prolonged both LTS (+53%, n = 32 cells, p = 3.7 x 10^{-9}) and burst latency (+58%, n = 21 cells, p = 1.1 x 10^{-9}). We observed the same trend across pharmacological conditions for all other conductance amplitude scales (Figure 2E). As the inter-burst interval (latency from last burst) separates each cycle of seizure-like oscillations, and is dominated by inhibition of TC cells [192], the above results are consistent with the increase in oscillation period upon following either individual GAT1 or GAT3 blockade, but a more pronounced effect for the latter (Figure 1E).

We also examined the distributions of effects on LTS features across neurons responsive to *d*IPSCs (Figure 2D). Relative to *d*Control responses, there was an increase in average number of spikes per LTS, average LTS peak value and average LTS maximum slope following either *d*GAT1-Block (n = 32, spikes per LTS: +62%, p = 1.3 x 10^{-6}, peak value: 2.5 ± 0.5 mV, p = 1.4 x 10^{-4}, maximum slope: +52%, p = 2.6 x 10^{-9}) or *d*GAT3-Block (n = 32, spikes per LTS: +93%, p = 9.3 x 10^{-7}, peak value: 3.3 ± 0.8 mV, p = 5.2 x 10^{-4}, maximum slope: +82%, p = 1.4 x 10^{-9}). As both greater LTS peak value and greater LTS maximum slope increase the likelihood for action potential generation, these changes were consistent with both the observed increase in spikes per LTS following either *d*GAT1-Block or *d*GAT3-Block and, secondarily, the prolongation of oscillation duration following either GAT1 or GAT3 blockade (Figure 1D). In contrast, dual GAT1+GAT3 blockade reduced burst probability and abolished oscillations (Figure 1F).

In summary, the bidirectional differences in rebound burst probability, burst latency and LTS features of single thalamocortical neurons in response to different $GABA_B$ activation waveforms were in agreement with the bidirectional differences in thalamic oscillation duration and period following the corresponding pharmacological manipulations. That is, by ultimately regulating thalamocortical neuron bursting, GATs appear to powerfully control thalamic network oscillations through differential activation of $GABA_B$ receptors.

Single neuron models

We next sought to determine the essential components of the thalamocortical neuron that contributes to the differential *d*IPSC responses observed during our dynamic clamp experiments. We also sought to better understand the underlying channel dynamics contributing to the differential responses. Towards these ends, we established a conductance-based, multi-compartment, single neuron model for each of the 36 experimentally recorded thalamocortical neurons for which we had stable responses across all acquired conductance amplitude scales (Figure 3A).

Our preliminary modeling results using existing TC cell models[254,250] failed to recapitulate two key features of $GABA_B$ receptor-mediated post-inhibitory rebound LTSs that are likely critical in determining network level responses. Notably, the average LTS latencies of the model responses were routinely much earlier (400~1000 ms) than the biological ones (400~4000 ms). In addition, the model LTS and burst responses tended to be continuously graded in amplitude as a function of inhibitory strength, in contrast to the more characteristic all-or-none responses of recorded neurons. Therefore, we developed a gradient descent fitting approach to obtain suitable multicompartment models

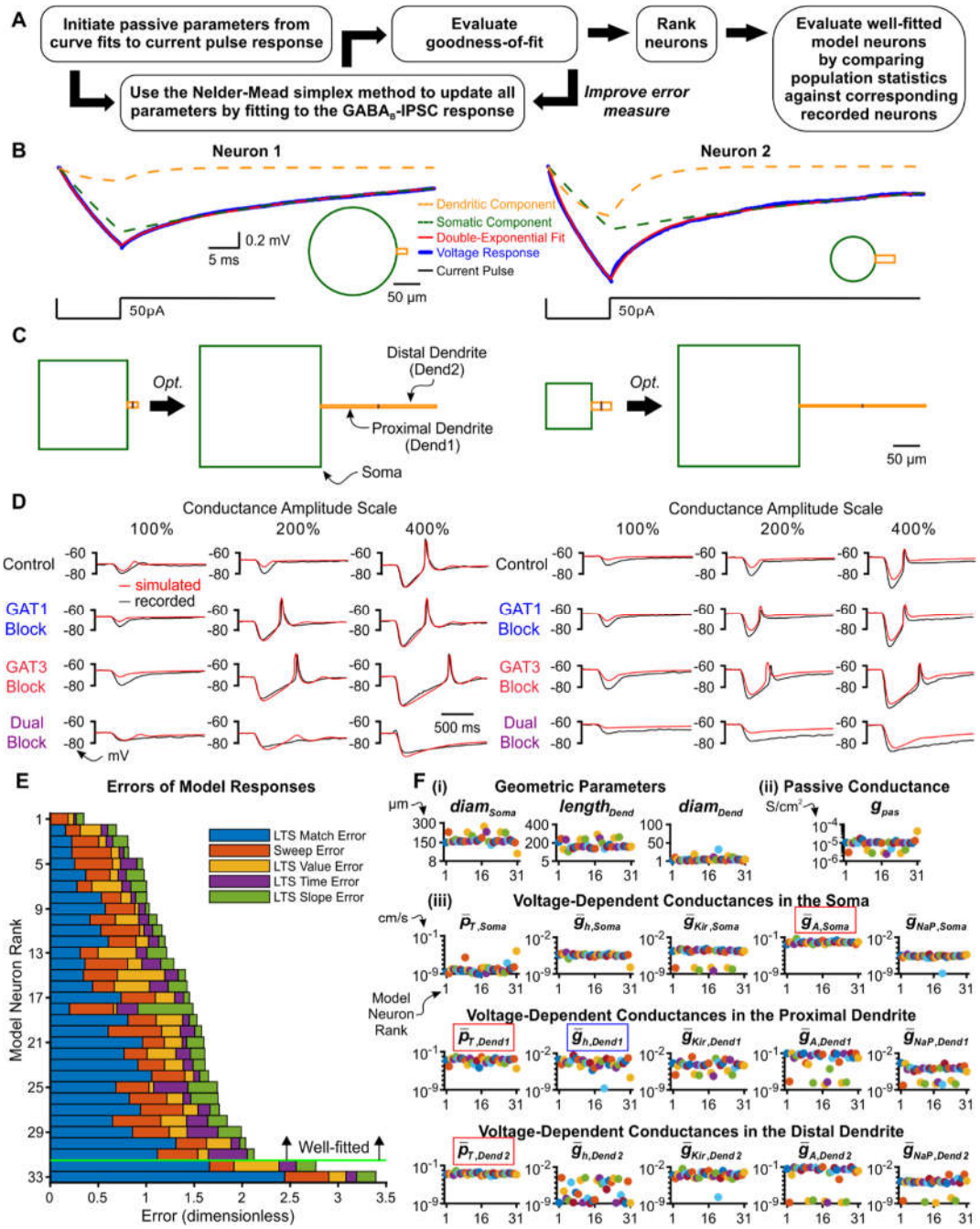

Figure 3. Model thalamocortical neurons reproduce $GABA_B$ IPSC and rebound responses. (**A**) Model optimization workflow. (**B**) Sample double-exponential curve fits (red) to averaged current pulse responses (blue) for two example neurons. The dotted lines correspond to the curves representing the somatic compartment (green) and dendritic compartment (orange). The resulting ball-and-stick geometries estimated from the 2 exponential components are shown below the recordings [280]. (**C**) We converted ball-and-stick models shown in (B) to cylindrical, three compartment models (left), which were then optimized (right). (**D**) Fits of simulated *s*IPSC responses to recorded *d*IPSC responses, for the same two neurons. (**E**) The 33 model neurons that underwent optimization were ranked by a weighted average of 5 different types of errors (see *Methods*). The 31 highest ranked model neurons were considered *well-fitted*. (**F**) Final values of parameters that could vary for the 31 well-fitted model neurons. Note that the T channel density is high in the dendrites and the A-type potassium channel density is high in the soma for all model neurons (red boxes). The h channel density in the proximal dendrite negatively correlates with LTS latency (blue box). Geometric parameters are in µm, maximal conductance densities ($\bar{g}$) and conductance densities (g) are in S/cm^2 and maximal permeability densities ($\bar{p}$) are in cm/s. The x axis is the model neuron rank in (E). We distinguish among (**i**) geometric parameters, (**ii**) voltage-independent *passive* parameters and (**iii**) voltage-dependent *active* parameters.

compatible with the data. As prior computational and experimental work demonstrates the importance of higher T channel densities in dendritic versus somatic compartments[254–257], we modeled each thalamocortical neuron by a cylindrical somatic compartment and two cylindrical dendritic compartments in series (Figure 3C).

To reduce the number of fitted parameters, some simplifying assumptions were made: the somatic length and diameter were equivalent, the two dendritic compartments had equal dimensions, and passive leak channels were inserted into all three compartments at uniform densities. Four voltage-independent (passive) parameters were allowed to vary across model neurons: the somatic diameter ($diam_{soma}$), the dendritic diameter ($diam_{dend}$), the dendritic length ($lengt_{dend}$) and the passive leak conductance density (g_{pas}). As prior work has identified ionic currents that contribute to the resting membrane potential of thalamocortical neurons[250], we inserted the following five voltage-dependent channels in all three compartments: the T-type calcium channel (I_T), the hyperpolarization-activated nonspecific cationic channel (I_h), the A-type transient potassium channel (I_A), the inward-rectifying potassium channel (I_{Kir}) and the persistent sodium channel (I_{NaP}). The densities of voltage-dependent channels were allowed to vary across compartments, resulting in a total of 15 (5 currents x 3 compartments) voltage-dependent (active) parameters that were allowed to vary across model neurons.

To provide an initial estimate of the geometric parameters that corresponded to each recorded thalamocortical neuron, we applied the short pulse methodology described by Johnston and Wu[280]. During dynamic clamp experiments, we applied a short current pulse at the beginning of each recorded sweep. The average current pulse response for each neuron was well-fitted by a double exponential function (Figure 3B). From the coefficients and time constants of the two exponential components, we inferred the

following four parameters for a ball-and-stick model[281]: input conductance, electrotonic length, dendritic-to-somatic conductance ratio and the membrane time constant. These Rall model values were then converted into initial passive parameter seed values ($diam_{Soma}$, $diam_{Dend}$, $lengt_{dend}$, g_{pas}) of each 3-compartment model neuron (see *Methods*).

Single thalamocortical neuron responses recorded during dynamic clamp experiments served to optimize passive and active parameters of each 3-compartment, model thalamocortical neuron. $GABA_B$ receptors were placed in the somatic compartment of each model neuron, and activation waveforms identical to the conductance waveforms used in dynamic clamp (the *d*IPSCs) were applied. We refer to these simulated $GABA_B$ receptor activation waveforms as *s*IPSCs, corresponding to each pharmacological condition (*s*Control, *s*GAT1-Block, *s*GAT3-Block, *s*Dual-Block). For each model neuron, simulated responses to *s*IPSCs were iteratively compared to experimental *d*IPSC responses. We evaluated the goodness-of-fit for each iteration with a total error defined by a weighted combination of component errors (see *Methods*). Examples of resultant geometry and voltage response fits are shown in Figures 3C and 3D, respectively.

Each model neuron was trained using a set of 12 recorded traces, each selected from a different *d*IPSC waveform, but evaluated against all recorded traces for the neuron and ranked by the total error (Figure 3E). By removing neurons with a total error greater than two standard deviations above the mean, we designated the top 31 neurons as the set of *well-fitted model neurons*. All well-fitted neurons were characterized by high T channel densities in the distal dendrite and high A-type potassium channel densities in the soma (Figure 3F). Considerable variability among model neurons was observed in the den-

sities of other ionic channels, likely contributing to the heterogeneity in LTS and burst statistics among recorded neurons in response to each $GABA_B$ *d*IPSC waveform (Figure 2D). For example, the value of the maximal h channel conductance density in the proximal dendrite $\bar{g}_{h,Dend1}$ was negatively correlated with LTS latency (R^2 = -0.80, not shown), which is consistent with the depolarizing effects of the h current[162].

We compared the distribution of LTS probabilities and features over the 31 well-fitted model neurons and over their 31 corresponding neurons recorded in dynamic clamp. In general, there was high agreement between the model simulations and dynamic clamp recordings. We first compared the *d* and *s*IPSC datasets when scaled by 200% (Figure 4A and 4B). Relative to *d*/*s*Control responses, LTS probability was increased following *d*/*s*GAT1-Block (n = 31, model: +30%, p = 0.0086, recorded: +31%, p = 0.038) or *d*/*s*GAT3-Block (model: +44%, p = 7.4 x 10^{-4}, recorded: +45%, p = 0.011) and decreased following *d*/*s*Dual-Block (model: -75%, p = 9.8 x 10^{-7}, recorded: -93%, p = 5.7 x 10^{-4}). Relative to *d*/*s*Control responses, average LTS latency was not different following *d*/*s*GAT1-Block (model: n = 27, p = 0.85, recorded: n = 21, p = 0.99) but was increased following *d*/*s*GAT3-Block (model: +42%, n = 27, p = 7.3 x 10^{-8}, recorded: +52%, n = 21, p = 2.4 x 10^{-6}). Differences in average number of spikes per LTS, average LTS peak value and average LTS maximum slope across *d*IPSC waveforms were not sufficiently captured by model neurons. The same trends across pharmacological conditions were observed for all other conductance amplitude scales, showing high agreement between model and recorded neurons for LTS probability and latency, but not for other LTS features (Figure 4C and 4D).

In summary, many single neuron models were established that sufficiently recapitulated the probability and timing of post-inhibitory rebound bursts in response to 12 different physiological $GABA_B$-receptor IPSC waveforms. A commonality among well-fitted

model neurons is that T channel densities were high in the dendrites and A-type

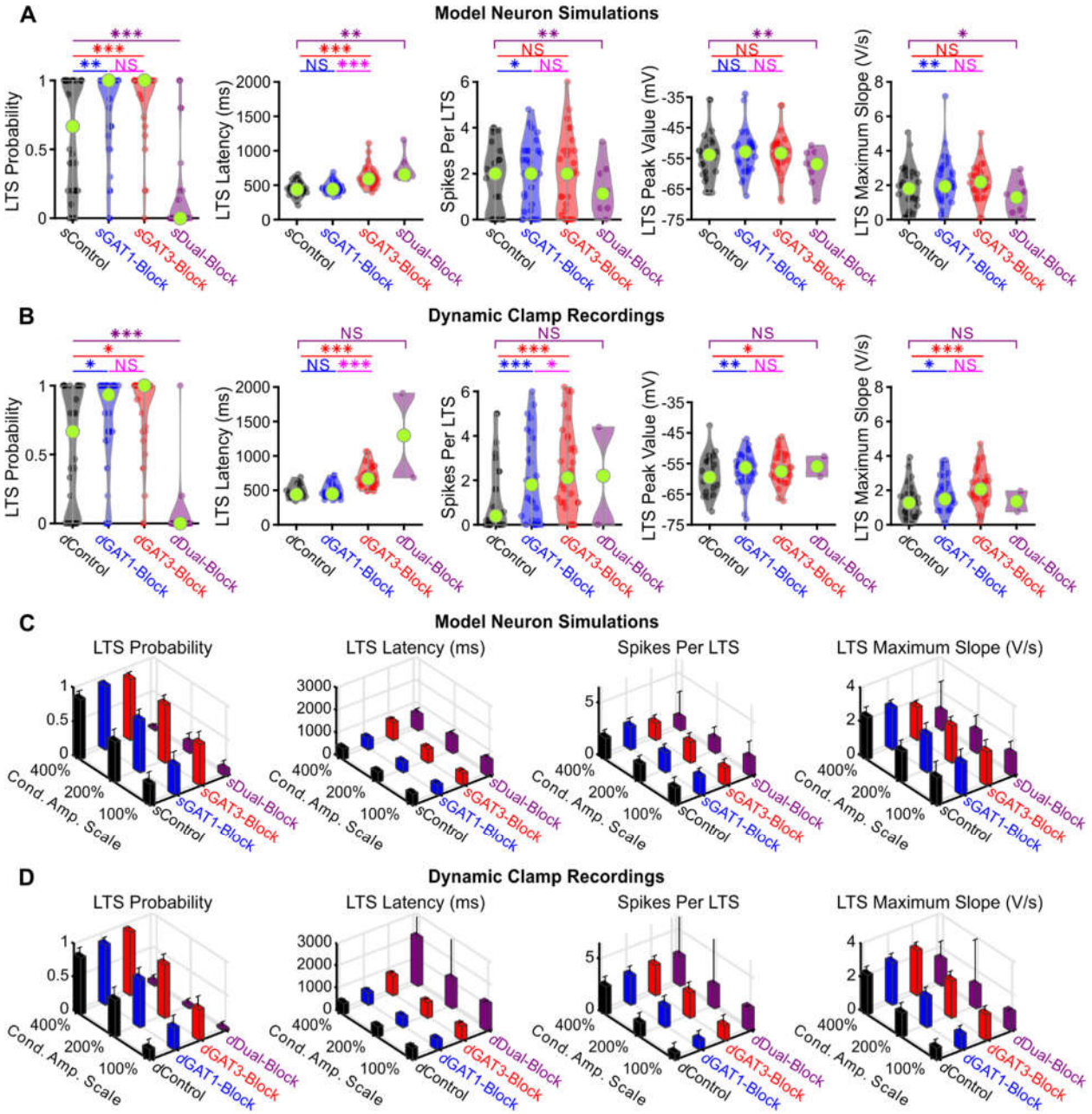

Figure 4. Well-fitted model and recorded neurons show similar low-threshold rebound spike differences in response to different $GABA_B$ IPSC waveforms.
(**A**) Distributions of post-inhibitory, low-threshold rebound spike measures over the 31 well-fitted model neurons across $GABA_B$ IPSC waveforms shown in Figure 2B (* $p < 0.05$, ** $p < 0.01$, *** $p < 0.001$, repeated-measures ANOVA for LTS probability, Friedman's test otherwise). (**B**) Same as (A) but for the corresponding 31 recorded neurons (Repeated-measures ANOVA for Spikes per LTS and LTS peak value, Friedman's test otherwise). (**C**) Mean LTS or burst measures over all 31 model neurons, across 4 different $GABA_B$ IPSC waveforms and 3 different conductance amplitude scales. Error bars denote 95% confidence intervals. (**D**) Same as (C) but for the corresponding 31 recorded neurons.

potassium channel densities were high in the soma, while there was heterogeneity in other channel densities.

Interplay between $GABA_B$ receptors and T-type calcium channels

We next sought to understand the post-synaptic ion channel dynamics contributing to the IPSC-evoked, post-inhibitory rebound LTS. We first compared examples of LTS-*producing* responses evoked by *s*GAT1- and *s*GAT3-Block waveforms with examples of LTS-*lacking* responses evoked by *s*Control and *s*Dual-Block waveforms in a model neuron (Figure 5). For LTS-producing responses, the LTS voltage response was present across all three compartments and appeared largest in the distal dendrite (Figure 5A). This voltage response reflected a dominant T-type calcium current in dendritic compartments (Figure 5B-C), consistent with experimental findings[255–257]. The initiation of the LTS was also associated with a slightly delayed outward A-type potassium current that was distributed more evenly across compartments (Figure 5B-C). The temporal overlap between the T and A currents has been shown to be important for controlling the LTS amplitude and width[282].

While much is known regarding the gating properties of low threshold, T-type calcium channels, little is known about how these properties behave during physiological stimuli such as voltage changes induced by synaptic inhibition. Although it has been proposed from artificial voltage ramp studies that rebound bursting is sensitive to the slope of voltage repolarization[263], the underlying T channel dynamics that confer such voltage sensitivity remain unknown. We therefore sought to understand how T channel activation and inactivation contribute to the production of the post-inhibitory rebound LTS (Figure 5D). In our well-fitted model neurons, we tracked the activation (m_T) and inactivation ($_T$) gating variables of the T channel, as a function of time. By convention,

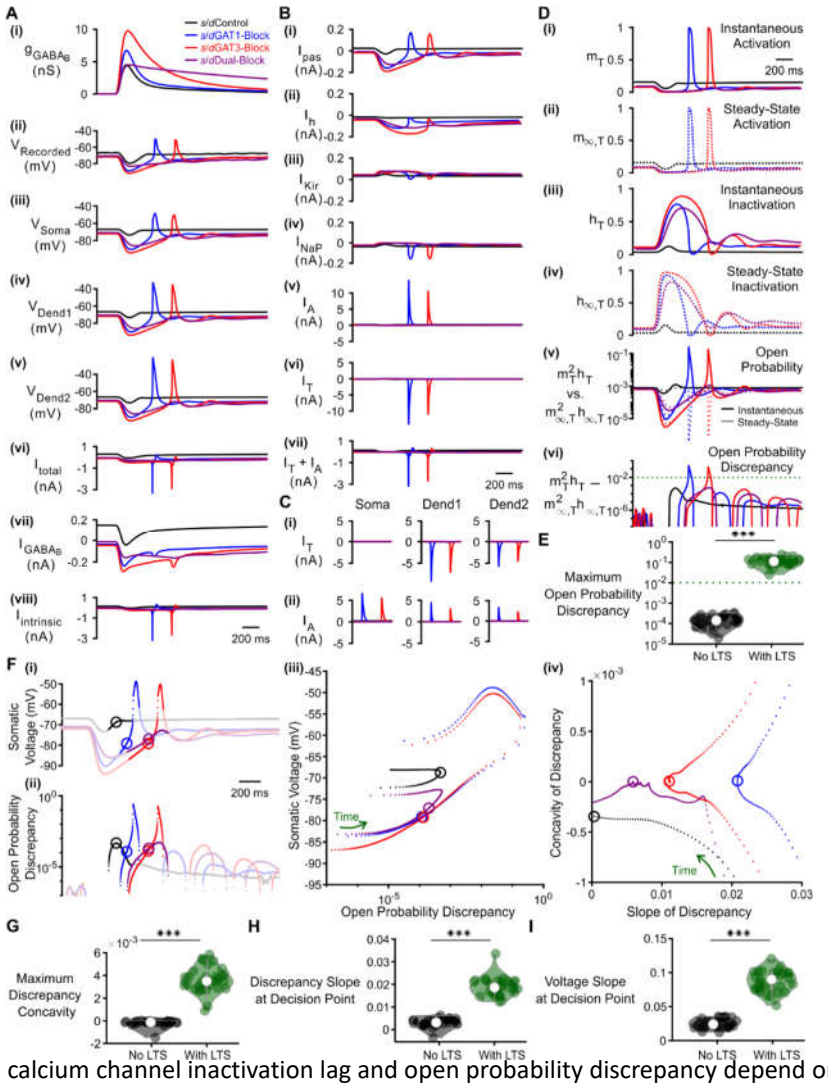

Figure 5. T-type calcium channel inactivation lag and open probability discrepancy depend on $GABA_B$ IPSC waveforms.
(**A**) The LTS response was most pronounced in the distal dendrite and correlates with the presence of large intrinsic channel currents. (**i**) Command *d/s*IPSCs as in Figure 2B. (**ii**) Voltage responses of Neuron 1 of Figure 2C recorded using dynamic clamp. (**iii-viii**) Simulated responses of the corresponding model neuron, including: (**iii**) somatic voltage, (**iv**) proximal dendritic voltage, (**v**) distal dendritic voltage, (**vi**) total current, (**vii**) $GABA_B$ receptor current, (**viii**) total intrinsic channel current. Currents were summed over all three compartments. (**B**) T-type calcium currents and A-type potassium currents were at least an order of magnitude larger than other intrinsic currents, with the T currents contributing to LTS initiation. Intrinsic currents were summed over all three compartments and include: (**i**) passive leak current, (**ii**) hyperpolarization-activated cationic current, (**iii**) inward-rectifying potassium current, (**iv**) persistent sodium current, (**v**) A-type fast-transient potassium current, (**vi**) T-type calcium current. A sum of A and T currents is shown in (**vii**). (**C**) Comparison of A and T currents across compartments. T currents were much larger in the dendrites and A currents were slightly elevated in the soma. (**D**) A combination of T channel recovery (high $_T$)$_2$ and inactivation lag ($_T$ different from $_{T,\infty}$) appeared to be necessary for T channel opening (high $m_T{}^2{}_T$). State variables for the distal dendritic T channel (other two compartments are similar) include: (**i**) instantaneous activation gating variable, (**ii**) steady-state activation gating variable, (**iii**) instantaneous inactivation gating variable, (**iv**) steady-state inactivation gating variable, (**v**) instantaneous open probability (solid line) versus steady-state open probability (dotted line), (**vi**) difference of instantaneous versus steady-state open probability (open probability discrepancy). (**E**) The maximum open probability discrepancy was higher in LTS-producing responses (*** $p < 0.001$, n = 31 cells, paired-sample *t*-test). (**F**) Within the LTS regions highlighted in both (**i**) somatic voltage curves and (**ii**) dendritic T channel open probability discrepancy curves, LTS-producing responses followed different trajectories than LTS-lacking responses in either (**iii**) the voltage vs. open probability discrepancy phase plot or (**iv**) the concavity versus slope of discrepancy phase plot. Sample points plotted are 1 ms apart. Circles denote the decision points where either zero (or maximal negative) concavity is reached in the open probability discrepancy curves. (**G**) The maximum open probability discrepancy concavity in the LTS region, (**H**) The slope of open probability discrepancy at the decision point, and (**I**) The slope of somatic voltage at the decision point were all higher in LTS-producing responses (*** $p < 0.001$, n = 31 cells, paired-sample *t*-test).

$m_T = 1$ when all channels are activated, and $_T = 0$ when all channels are inactivated[283]. We also distinguished between steady-state values ($m_{T,\infty}$ and $_{T,\infty}$), which depend only on voltage, from instantaneous values (m_T and $_T$), which reach steady-state values exponentially through a voltage-dependent time constant (i.e. depend on voltage and time).

One notable feature of the T channel is that the inactivation time constant is about 10-fold higher than the activation time constant [248]. Indeed, in all conditions, the instantaneous T channel activation variable m_T was nearly identical to its voltage-dependent steady-state value $m_{T,\infty}$. However, the instantaneous T channel inactivation variable $_T$ never achieved its steady-state value $_{T,\infty}$ during dynamic changes in membrane voltage (Figure 5D). That is, the activation gate responded to changes in membrane potential quickly, but the inactivation gate responds slowly. Notably, the T channel inactivation lag was larger for LTS-producing responses than for LTS-lacking responses.

We next explored how T channel inactivation lag affects open probability. Without significant T channel inactivation lag, there was no discrepancy between the instantaneous and steady state T channel open probabilities. Based on the measurements by Huguenard and McCormick[247], the maximum achievable T channel open probability at steady state ($\max_V(m_{T,\infty}(V)^2 \ _{T,\infty}(V))$) is 8.4 x 10^{-4}, which is close to the LTS-lacking, pre-IPSC, baseline values in our simulations (Figure 5D). Consequently, an LTS was only produced when the instantaneous T channel open probability ($m_T{}^2 \ _T$) was orders of magnitude higher than steady-state open probabilities. In fact, when all 31 well-fitted model neurons were considered, the maximum difference between the instantaneous and steady-state open probability ($\max_t(m_T{}^2 \ _T \quad m_{T,\infty}{}^2 \ _{T,\infty})$) was on average 2.9 orders of magnitude higher for LTS-producing responses than for LTS-lacking responses (Figure 5E, n = 31 cells,

p = 2.4 x 10^{-29}). Herein, we refer to the difference between instantaneous versus steady-state open probability ($m_T{}^2{}_T \quad m_{T,\infty}{}^2{}_{T,\infty}$) simply as *T channel open probability discrepancy*. When each trace for all 31 model neurons was considered, a threshold open probability discrepancy of 10^{-2} separated LTS-producing responses from LTS-lacking responses (not shown).

We sought to understand how high or low T channel open probability discrepancy arises in response to distinct *s*IPSCs. When the somatic voltage was plotted against the dendritic T channel open probability discrepancy, LTS-producing responses produced trajectories that were qualitatively different from the LTS-lacking responses (Figure 5F). For all *s*IPSC responses, open probability discrepancy increases upon voltage depolarization. Nevertheless, only for LTS-producing responses does the open probability discrepancy curve reach an inflection point (point of zero concavity) that eventually progresses to positive concavity. We define the point at which the open probability discrepancy curve reaches zero (or maximal negative) concavity as the *decision point* (circles in Figure 5F). A comparison between the *s*GAT3-Block (red) and sDual-Block (purple) responses showed that at the decision point, the *slope* of open probability discrepancy, rather than its value, determines whether positive concavity is eventually achieved. In fact, for all open probability curves that reach zero concavity, the slope of the open probability discrepancy curve at the decision point is always higher for LTS-producing responses than for LTS-lacking responses, but the threshold is cell-dependent (not shown). We show the progression of trajectories aligned to the decision points for two conditions (Movie 1, *s*GAT3-Block and sDual-Block) and for all conditions (Movie 2). When all 31 well-fitted model neurons were considered, there was a significant difference between LTS-producing and LTS-lacking responses for either the maximum open probability discrepancy concavity (Figure 5G), the

discrepancy slope at the decision point (Figure 5H) or the voltage slope at the decision point (Figure 5I). We conclude that IPSC responses produce LTSs only if two conditions are satisfied: (1) the open probability discrepancy curve reaches zero concavity, and (2) the slope of the open probability discrepancy curve at that decision point reaches a cell-dependent threshold.

We next applied our understanding of the T channel open probability discrepancy to how GAT-modulated, $GABA_B$ IPSCs regulate LTS production. We observed that the *s*Control waveform did not produce an LTS response simply because inhibition was insufficient for T channel recovery ($_T$ was always below 0.2, Figure 5D). In contrast, although T channels were sufficiently recovered ($_T$ reached above 0.6) by strong hyperpolarization associated with *s*GAT1-, *s*GAT3-, and *s*Dual-Block waveforms, only the former two waveforms produced an LTS response. We observed that rapid repolarization from a hyperpolarized state in response to the *s*GAT1- and *s*GAT3-Block waveforms allowed activation gates to open (m_T increased) before the inactivation gates closed ($_T$ decreased), creating a brief window characterized by a discrepancy between high instantaneous T channel open probabilities ($m_T{}^2$ $_T > 10^{-2}$) and the low steady-state open probabilities ($m_{T,\infty}{}^2$ $_{T,\infty} < 10^{-2}$). In contrast, the *s*Dual-Block waveform produced a prolonged inhibition, resulting in a slower rise during membrane potential repolarization, a small lag in T channel inactivation, a lack of increase in T channel open probability discrepancy and, ultimately, a lack of LTS response.

To test the contribution of T channel inactivation lag to LTS production, we bidirectionally altered the T channel inactivation time constant (τ_{h_T}) for the same *s*IPSC response simulations as in Figure 5. When τ_{h_T} was halved in *s*GAT1- and *s*GAT3-Block simulations,

T channel open probability discrepancy remained low and LTS responses normally observed during GAT1 and GAT3 blockade were abolished (cf. Figure 6A with Figure 5). In contrast, doubling τ_{h_T} in *s*Dual-Block simulations promoted a discrepancy between instantaneous and steady-state open probabilities and, consequently, normally absent LTSs appeared (cf. Figure 6B with Figure 5). Note that *s*Control waveforms did not produce an LTS as voltage hyperpolarization was weak and T channel recovery was low. Thus, a combination of sufficient T channel recovery and high T channel open probability discrepancy appears to be necessary for LTS production.

The kinetics of inhibition appeared to underlie the observed T channel open probability discrepancy. We therefore systematically varied the time constant of an LTS-producing *s*GAT3-Block IPSC while fixing the amplitude. Prolonging IPSC kinetics decreased T channel open probability discrepancy and abolished LTS responses as time constants increased above 4-fold (Figure 6C). Conversely, shortening the time constant of a non-LTS-producing *s*Dual-Block IPSC – also while fixing the amplitude – increased T channel open probability discrepancy and produced LTS responses as time constants decreased by 20% (Figure 6D). We show the progression of trajectories aligned to the decision points for two time constants (Movie 3, last LTS success and first LTS failure) and for all time constants (Movie 4). As changing the kinetics of inhibition also changes the total amount of inhibition delivered to a cell, we also changed inhibition kinetics while keeping charge (i.e. the area under the curve) constant. Nevertheless, we continued to observe that instantaneous versus steady-state open probability discrepancies became smaller and LTS responses diminished as *s*IPSC kinetics increased (Figure 6E). Therefore, the temporal envelope of inhibition appears to be important for LTS production through its influence on T channel open probability discrepancy.

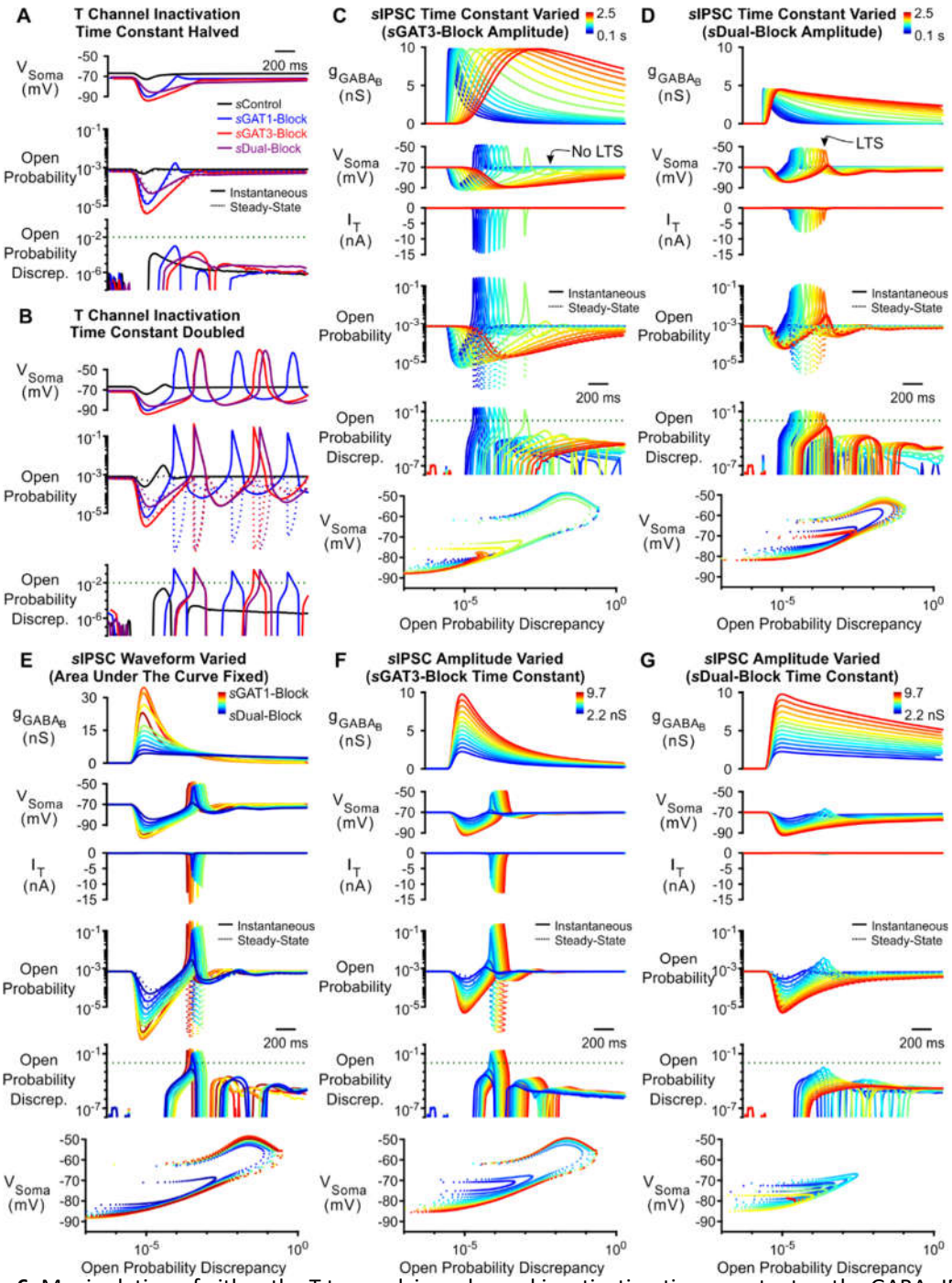

Figure 6. Manipulation of either the T-type calcium channel inactivation time constant or the $GABA_B$ IPSC kinetics bidirectionally modulates low-threshold rebound spike production.
(**A**) Simulated responses as in Figure 5 with the T channel inactivation time constant τ_{h_T} halved. The T channel inactivation lag disappeared and no LTS was produced following any *s*IPSC waveform. (**B**) Simulated responses as in Figure 5 with τ_{h_T} doubled. The T channel inactivation lag lengthened and LTSs appeared following *s*Dual-Block. (**C**) LTS responses to the *s*GAT3-Block waveform (blue) gradually disappeared as the time constant was increased (with amplitude fixed) to that of the *s*Dual-Block waveform (red). (**D**) LTS responses to the *s*Dual-Block waveform (red) gradually appeared as the time constant of the waveform was decreased (with amplitude fixed) to that of the *s*GAT3-Block waveform (blue). (**E**) LTS responses to the *s*Dual-Block waveform (blue) gradually appeared as all parameters of the waveform were shifted (with area under the curve fixed) to that of the *s*GAT3-Block waveform (yellow), then to the *s*GAT1-Block waveform (dark red). (**F**) LTS responses gradually appeared as the amplitude of the *s*GAT3-Block waveform was increased (with time constant fixed). (**G**) Robust LTS responses never appeared as the amplitude of the *s*Dual-Block waveform is increased (with time constant fixed).

Since hyperpolarization promotes T channel recovery[248], it remains possible that a sufficiently strong hyperpolarization – regardless of waveform – will produce an LTS. To test this possibility, we varied the inhibition amplitude using either the *s*GAT3-Block (fast kinetics) or *s*Dual-Block (slow kinetics) waveform. As we increased the amplitude of the *s*GAT3-Block waveform while fixing the rise and decay time constants, LTSs emerged as T channel open probability discrepancy increased (Figure 6F). In contrast, as the amplitude of the *s*Dual-Block waveform increased while fixing the rise and decay time constants, T channel open probability discrepancy nonetheless remained low and robust LTS responses never emerged (Figure 6G). Thus, fast inhibition kinetics are important for driving T channel open probability discrepancy, and slow kinetics provides an explanation for the consistently low LTS or burst probability across conductance amplitude scales following *s*/*d*Dual Block (Figures 2E, 4C and 4D).

In summary, LTS production following physiological inhibition is largely controlled by the dynamics of T channel open probability discrepancy in the distal dendrites. We extend this understanding by showing that LTS production appears to depend not only on the *amplitude* of inhibition, but also the *temporal envelope* of inhibition. Large inhibition amplitude is required for sufficient T channel recovery, whereas fast inhibition decay is required for driving the T channel open probability discrepancy beyond an inflection point and creating a brief time window with sufficiently high T channel open probability for LTS production.

Network models

We next explored whether the interplay between $GABA_B$-mediated inhibition and T type calcium channel dynamics in thalamocortical neurons contributes to the observed

changes in network-level oscillations following GAT blockade. We first examined the effects of $GABA_B$ receptor-mediated inhibition in a simplified 2-cell network configuration. In each 2-cell network, we connected a single compartment, GABAergic reticular thalamic model neuron[284] to one of the 31 well-fitted model thalamocortical neurons (Figure 7A). To generate action potentials, Hodgkin-Huxley type sodium and potassium channels were inserted into the somatic compartment of each model neuron[257]. The reticular thalamic neuron was connected to the thalamocortical neuron via a $GABA_B$ receptor-mediated inhibitory synapse ($GABA_A$ receptors were blocked during experimentally evoked oscillations, see Figure 1). Consistent with previous intra-thalamic models[173], the thalamocortical neuron provided AMPA receptor-mediated excitation to reticular thalamic neurons. By applying a brief stimulating current to the reticular thalamic neuron and varying the $GABA_B$ receptor activation parameters (*s*IPSCs), $GABA_B$ conductance waveforms comparable to those used by dynamic clamp were evoked in each thalamocortical neuron (Figure 7B). To simulate variable tonic inhibition on thalamocortical neurons, we varied the thalamocortical neuron leak reversal potential between -73 and -60 mV (14 leak reversal potentials). To generate trial-to-trial variability (5 trials per leak reversal potential), we randomized the leak conductance of each neuron to within 10% of the original value. Of all 31 possible 2-cell networks, 24 had a quiescent, pre-stimulation baseline over this range of leak reversal potentials. In those networks with quiescent baseline, oscillations persisted only when the $GABA_B$-mediated inhibition promoted T channel open probability discrepancy in thalamocortical neurons to produce rebound bursting (Figure 7C). An oscillation probability was computed for each 2-cell network over the 14 x 5 = 70 trials. In addition, an oscillatory period and an oscillatory index based on the autocorrelation function of pooled spikes was computed for each

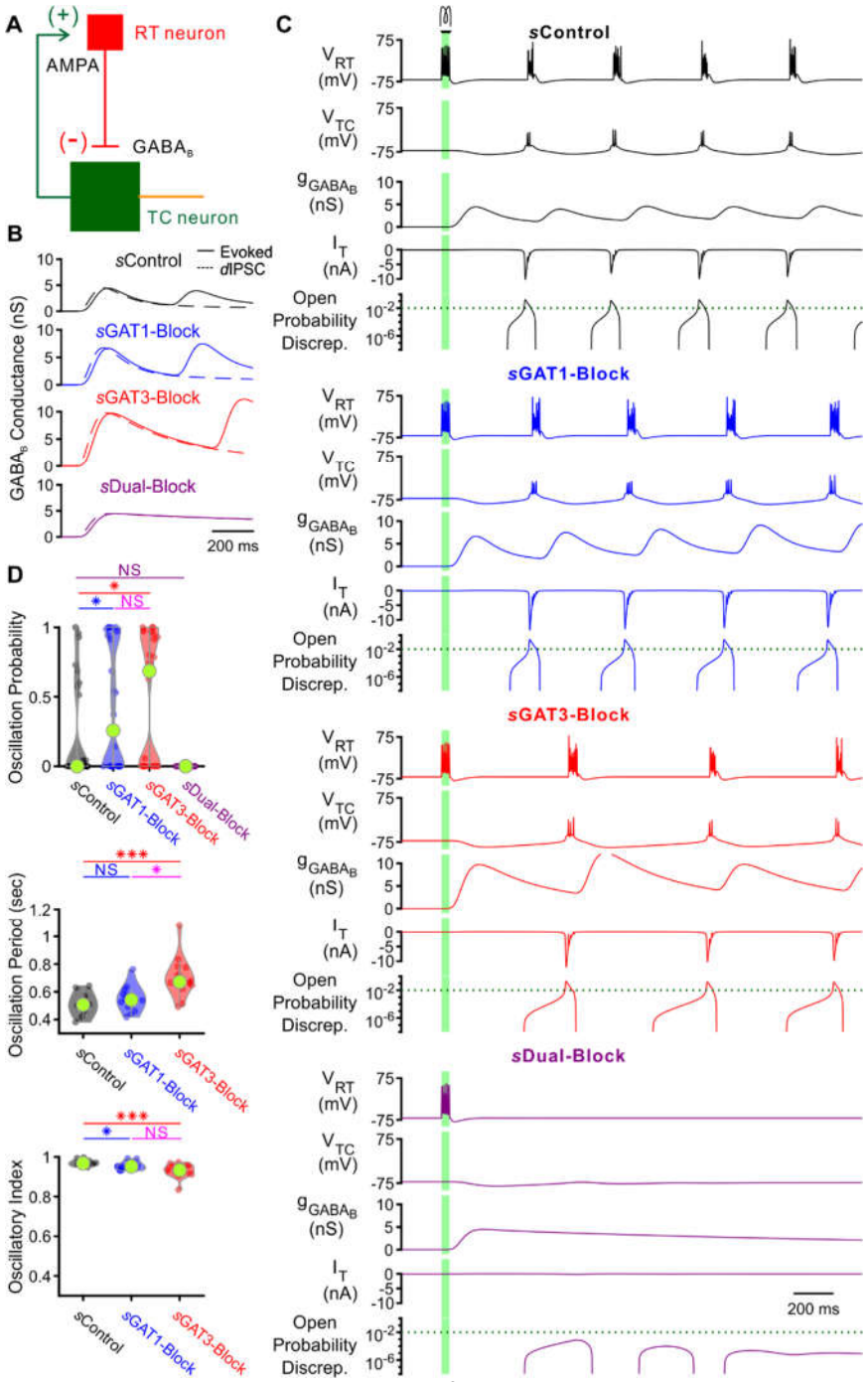

Figure 7. GABA$_B$-receptor mediated conductance waveforms modulate oscillations produced by 2-cell model thalamic networks.
(**A**) Schematic of a 2-cell model network. A reticular thalamic (RT) neuron projected a GABA$_B$ receptor-mediated inhibitory synapse (-) to a thalamocortical (TC) neuron, which reciprocally projected an AMPA receptor-mediated excitatory synapse (+) to the reticular thalamic neuron. (**B**) Evoked GABA$_B$ conductance waveforms in network model TC neurons (solid lines) were similar to GABA$_B$ *d*IPSC waveforms (dashed lines). (**C**) 2-cell network responses under different GABA$_B$ receptor conditions. Model TC neuron parameters corresponded to Neuron 1 in Figure 2. A brief (40 ms, 0.2 nA) current stimulus was applied to the reticular thalamic neuron, evoking an initial burst of 12 spikes. Oscillations were evoked under some but not all GABA$_B$ receptor conditions. A total of 24 model TC neurons produced oscillations in response to stimulation. (**D**) Distributions of oscillation measures over all 24, 2-cell networks. Oscillation probability was increased when either *s*GAT1-Block parameters or *s*GAT3-Block parameters were used, but decreased when *s*Dual-Block parameters were used (* $p < 0.05$, ** $p < 0.01$, *** $p < 0.001$, Friedman's test).

successfully-evoked oscillation (see *Methods*).

We examined the distributions of oscillation probability, average oscillation period and average oscillatory index over the 24 different 2-cell networks wherein *s*IPSCs were scaled by 200% (Figure 7D). Relative to using *s*Control parameters, oscillation probability increased when using *s*GAT1-Block parameters (+66%, n = 24 networks, p = 0.016) or *s*GAT3-Block parameters (+93%, p = 0.048). These results are consistent with the experimental observation that individual GAT1 or GAT3 blockade prolonged oscillations (Figure 2D). Relative to using *s*Control parameters, average oscillation period increased when using *s*GAT3-Block parameters (+39%, n = 10, p = 4.2×10^{-4}). These results are consistent with the experimental observation that individual GAT3 blockade increased oscillation periods (Figure 2E). In contrast, when *s*Dual-Block parameters were applied in the network, oscillations do not arise, consistent with the experimental observation that dual GAT1+GAT3 blockade inevitably abolished oscillations (Figure 2D & 2F). Although the 2-cell networks recapitulated some effects of GAT blockade on oscillations, the 2-cell oscillations were extremely stereotyped and regular, resulting in unrealistically high oscillatory indices.

We sought to determine whether larger, more complex model networks could more realistically simulate experimental oscillations and recapitulate the bidirectional effects of GAT blockade by varying *s*IPSCs. We scaled up the network to include one circular layer of 100 reticular thalamic (RT) neurons and one circular layer of 100 thalamocortical (TC) neurons (Figure 8A). RT-TC inhibitory connections and TC-RT excitatory connections were both convergent and divergent. To assess the importance of the geometric and conductance heterogeneity we observed in the single cell models (Figure 3F), we established two sets of model thalamic networks: (1) 24 *TC-homogeneous*

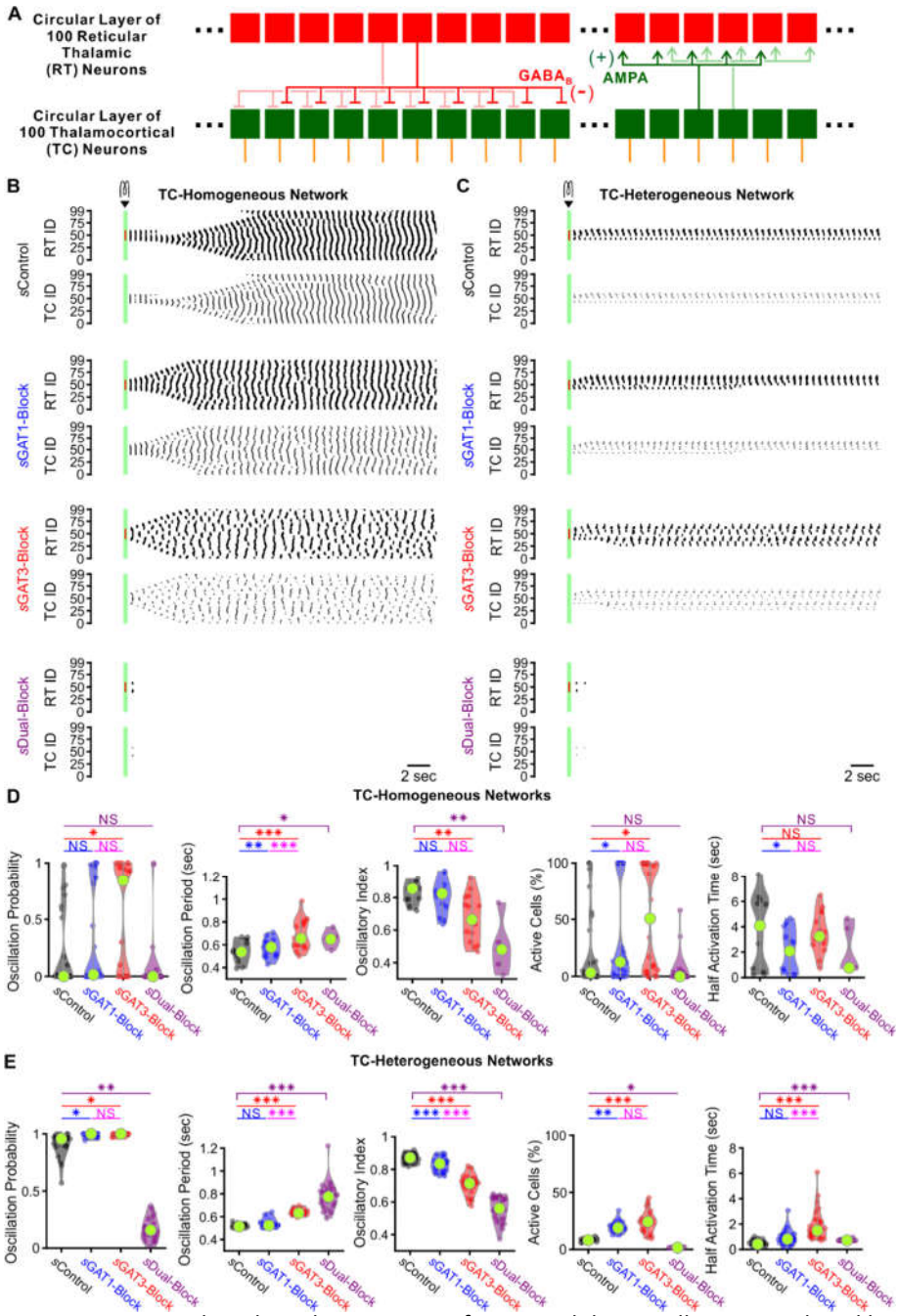

Figure 8. GABA$_B$-receptor mediated conductance waveforms modulate oscillations produced by 200-cell model thalamic networks.
(**A**) Schematic of a 200-cell model network. Each reticular thalamic (RT) neurons projected GABA$_B$ receptor-mediated inhibitory synapses (-) to 9 nearby thalamocortical (TC) neurons. Each TC neuron projected AMPA receptor-mediated synapses (+) to 5 nearby reticular thalamic neurons. (**B**) Sample spike raster plots of a TC-homogenous network, using model TC neuron parameters corresponding to Neuron 1 of Figure 3. A brief (40 ms, 0.2 nA) current stimulus was applied to each of the center 20 reticular thalamic neurons. Spikes within the stimulation period are red; all other evoked spikes are black. (**C**) Sample spike raster plots of a TC-heterogeneous network, using model TC neuron parameters corresponding to the 24 model TC neurons used in Figure 7. Relative to TC-homogeneous networks, activity was more localized for TC-heterogeneous networks. (**D**) Distributions of oscillation measures over all 24 TC-homogeneous 200-cell networks (* $p < 0.05$, ** $p < 0.01$, *** $p < 0.001$, repeated-measures ANOVA for oscillation period and half activation time, Friedman's test otherwise). (**E**) Distributions of oscillation measures over all 24 TC-heterogeneous 200-cell networks. Oscillation probability, oscillation period and percent of active cells increased when *s*GAT3-Block parameters were used, but decreased when *s*Dual-Block parameters were used (repeated-measures ANOVA for oscillatory index, Friedman's test otherwise).

networks with TC parameters taken from each of the 24 model neurons used for the 2-cell networks and (2) 24 *TC-heterogeneous* networks with TC parameters taken from all of the 24 model neurons, randomly ordered. All networks had a quiescent, pre-stimulation baseline when the thalamocortical neuron leak reversal potential was varied between -73 and -60 mV (14 leak reversal potentials). To generate trial-to-trial variability (5 trials per leak reversal potential), we randomized the leak conductance for each of the 200 neurons to within 10% of the original value. For both *TC-homogeneous* and *TC-heterogeneous* networks, oscillations emerged and spread in response to some but not all $GABA_B$ receptor activation parameters (Figure 8B & 8C). An oscillation probability was computed for each 200-cell network over the 14 x 5 = 70 trials. In addition, an oscillatory period, an oscillatory index and a half activation time was computed for each successfully-evoked oscillation (see *Methods*).

We examined the distributions of oscillation probability, average oscillation period, average oscillatory index, average percent of active TC cells and average half activation time over the set of *TC-homogeneous* networks (Figure 8D) and the set of *TC-heterogeneous* networks (Figure 8E) wherein *s*IPSCs were scaled by 200%. The values of oscillation periods and oscillatory indices for TC-heterogenous networks were similar to values extracted from experimental recordings (oscillation period: Figure 1E, oscillatory index: not shown). In response to the same *s*IPSC conditions, we observed highly varied (often bimodal) oscillation responses across TC-homogeneous networks, which reflects the highly varied LTS responses across individual model TC neurons (Figure 4B). In contrast, oscillation measures were less variable across the different TC-heterogeneous networks. Therefore, cell heterogeneity averages out the LTS response variability, provides more robust network responses and accentuates the differences across *s*IPSCs. Indeed, for the set of

TC-heterogeneous networks, relative to using *s*Control parameters, oscillation probability increased when using either *s*GAT1-Block (+8.2%, n = 24 networks, p = 0.049) or *s*GAT3-Block parameters (+8.5%, p = 0.013), but decreased when using *s*Dual- Block parameters (-82%, p = 0.0010); average oscillation period increased when using either *s*GAT3-Block (+23%, $p = 1.3 \times 10^{-7}$) or *s*Dual-Block parameters (+19%, $p = 2.8 \times 10^{-6}$); average percent of active TC cells increased when using either *s*GAT1-Block (+130%, p = 0.0044) or *s*GAT3-Block parameters (+193%, $p = 1.6 \times 10^{-5}$), but decreased when using *s*Dual-Block parameters (-79%, p = 0.037). These results are consistent with experimental findings that individual GAT1 or GAT3 blockade increased oscillation durations (Figure 2D) and oscillation periods (Figure 2E), whereas dual GAT1+GAT3 blockade eliminated oscillations (Figure 2F) in acute thalamic slices.

In summary, a population of thalamic network models was established that sufficiently recapitulated the bidirectional effects of individual versus dual GAT blockade on thalamic oscillations by merely altering the kinetics of $GABA_B$-receptor inhibition. Therefore, the same interplay between $GABA_B$-receptor-mediated inhibition and T channel open probability that governs thalamocortical neuron rebound bursting appears to regulate network-level oscillations. Furthermore, we found that including cell heterogeneity in network simulations provides more robust oscillations and more realistically recapitulates experimental oscillation periods by averaging out LTS response heterogeneity. Using heterogeneous networks in future studies would thus facilitate comparison across pharmacological conditions.

Discussion

We show that seizure-like thalamic oscillations were prolonged following individual GAT1 or GAT3 blockade, yet abolished following dual GAT1+GAT3 blockade. We have also shown that, relative to control $GABA_B$ IPSC waveform responses, thalamocortical neuron rebound burst probability increased following waveforms corresponding to individual GAT1 or GAT3 blockade, but decreased following waveforms corresponding to dual GAT1+GAT3 blockade. Using a population of model neurons and a population of model thalamic networks, we show that the observed thalamocortical neuron responses to $GABA_B$ IPSCs and the observed oscillation changes following GAT blockade, respectively, can be recapitulated by varying the $GABA_B$ receptor activation waveform. Finally, we've characterized a link between $GABA_B$-mediated inhibition and T channel opening across both voltage and time dimensions that provides an explanation for the bidirectional effects of GAT blockade on both thalamocortical rebound bursting and seizure-like oscillations. Specifically, we identified a decision point at which the discrepancy between the instantaneous and the steady-state T channel open probability follows one of two trajectories: failing to reach a concavity and slope threshold or driving past the threshold to produce a rebound burst. These observations provide a mechanistic explanation for burst sensitivity to voltage ramps[263], and burst sensitivity to both the amplitude and the decay of physiological synaptic inhibition.

Role of thalamocortical neuron rebound bursting in generalized seizures

Thalamocortical neuron rebound bursting has long been implicated in spike-wave discharges (SWDs) observed in generalized seizures, and T channels mediate thalamocortical neuron rebound bursting[69,163]. The expression of the CaV3.1 T channel subtype by thalamocortical neurons correlates with SWD expression in both animal models[69,149,61]

and human patients[40]. Blocking T channels reduce both thalamocortical neuron bursting and oscillations in thalamic slice models[215]. However, the importance of thalamocortical neuron bursting in generalized seizures remains unresolved. One recent study found reduced thalamocortical neuron firing during SWDs and a lack of seizure reduction with weak, local T channel blockade in the ventrobasal nucleus (however, strong blockade diminished SWDs[285]), while a second recent study found that increasing thalamocortical neuron bursting increases SWDs in both epileptic mice and rats[286]. One possibility accounting for these discrepant findings is that the population of active thalamocortical neurons during SWDs is sparse[287]. Interestingly, our heterogenous network models were largely characterized by robust, yet sparse, oscillations (in contrast, homogenous network models produced oscillations that were widespread, Figure 8B and C).

Our study found a strong relationship between thalamocortical neuron bursting and epileptiform thalamic oscillations. *First*, the pharmacological conditions in which oscillation *durations* were increased (individual GAT1 or GAT3 blockade) or decreased (dual GAT1+GAT3 blockade) relative to baseline were the same conditions in which thalamocortical neuron rebound burst *probability* increased (individual GAT1- or GAT3-Block $GABA_B$ *d*IPSC waveform) or decreased (Dual-Block $GABA_B$ *d*IPSC waveform), relative to control *d*ISPCs. *Second*, the pharmacological conditions in which oscillation *periods* were increased (GAT1 or GAT3 blockade) relative to baseline were also the same conditions in which thalamocortical neuron rebound burst *latencies* increased (individual GAT1- or GAT3-Block *d*IPSC waveform) relative to control *d*IPSCs. *Finally*, in our 2-cell model thalamic network, each successive oscillation cycle was initiated by a thalamocortical neuron rebound burst (Figure 7C), similar to what has been reported in experiments when a reticular thalamic neuron and a thalamocortical neuron is simultaneously recorded during

a thalamic oscillation[192].

Role of the inhibitory temporal envelope in seizures

Prior experimental and computational work has suggested that a shift from $GABA_A$ receptor-mediated to $GABA_B$ receptor-mediated inhibition at the RT-TC synapse transforms oscillations in acute thalamic slices from a 10 Hz, sparse, spindle-like activity to a 3 Hz, hyper-synchronized, seizure-like state[191,173,261,273]. Notably, the shift in oscillation frequency is consistent with differences in IPSC decay constants ($GABA_A$: < 100 ms; $GABA_B$: about 300 ms) recorded in thalamocortical neurons[215]. Multiple animal model studies support the hypothesis that generalized spike-wave seizures rely on robust $GABA_B$ receptor-mediated inhibition. Specifically, systemic injection of $GABA_B$ receptor agonists increases SWDs[223,272], while injection of $GABA_B$ receptor antagonists reduces or even abolishes SWDs[223,271]. Notably, however, other studies were not able to record rhythmic $GABA_B$ IPSCs during SWDs *in vivo*[288] or find significant SWD changes with $GABA_B$ receptor modulation[224], and have highlighted a particular role for extrasynaptic $GABA_A$ receptors in SWDs[66]. Presumably, tonic $GABA_A$ currents hyperpolarize the resting membrane potential, promoting T channel recovery and increasing rebound bursting[211]. Thus, the disparate conclusions regarding the importance of $GABA_A$ receptor-versus $GABA_B$ receptor-mediated inhibition appear to nonetheless converge on similar conclusions regarding the importance of T channel recovery, a process that involves membrane potential hyperpolarization. Under physiological conditions, it seems reasonable to expect multiple, convergent inhibitory mechanisms that promote T channel recovery.

Our study establishes a clear link between $GABA_B$ receptor-mediated inhibition, thalamocortical neuron rebound bursting and epileptiform thalamic oscillations. *First*, we

found a 1.4-fold or a 2-fold increase in oscillation duration in acute thalamic slices after perfusing with the GAT1 blocker NO-711 or the GAT3 blocker SNAP-5114 (Figure 1D), closely corresponding with the 1.5-fold or 2.2-fold increase in $GABA_B$ IPSC amplitude recorded under the same conditions, respectively[220]. *Second*, in both dynamic clamp recordings and model neuron simulations, the GAT1-Block and GAT3-Block $GABA_B$ IPSC waveforms produced higher thalamocortical neuron rebound LTS or burst probability relative to the Control waveform, with the GAT3-Block waveform increasing LTS or burst probability more (Figure 2D & Figure 4A-B). *Third*, we found that increasing conductances for each of the Control, GAT1-Block and GAT3-Block waveforms led to an increase in LTS or burst probability, for both dynamic clamp recordings and model neuron simulations (Figure 2E & Figure 4C-D). *Finally*, a comparison of the Control (black) versus GAT1-Block (blue) IPSC responses in Figure 5 shows that the lack of LTS in the former correlates with a decreased level of TC hyperpolarization, a lack of T channel de-inactivation (both $_T$ and $_{\infty,T}$ are low) and a deficiency in T current production (no spike in I_T), agreeing with prior studies in that the initiation of a low-threshold rebound spike depends on the sufficient removal of T channel inactivation through membrane potential hyperpolarization[159,248].

More interestingly, we found that not only is the overall amount of inhibition important, how such inhibition distributes over time is equally important. For instance, the *d*Dual-Block waveform has an area under the curve (i.e. charge) about twice that of the *d*GAT3-Block waveform (Figure 2B). Nevertheless, both dynamic clamp recordings and model neuron simulations showed that the *d*Dual-Block waveform decreased rebound burst probability relative to the control, whereas the *d*GAT3-Block waveform increased rebound burst probability (Figure 2D & Figure 4). In fact, the *d*Dual-Block waveform largely

failed to produce rebound bursts even when the conductance amplitude was scaled so high that the burst probability was close to 1 in all other conditions, i.e. following *d*Control, *d*GAT1-Block and *d*GAT3-Block waveforms (Figure 2E & Figure 4). Dual GAT blockade also abolished oscillations, in stark contrast to the robust prolongation of oscillations observed during GAT3 blockade only (Figure 1D & 1F). Therefore, even high levels of synaptic inhibition, if decayed too slowly, can abolish both thalamocortical neuron rebound bursts and epileptiform thalamic oscillations, a conclusion recapitulated by our model thalamic networks (Figure 7D & 8C).

T channel open probability discrepancy drives thalamocortical neuron rebound bursting

What are the intrinsic channels in thalamocortical neuron that enable rebound bursting? Prior experimental work has shown that T channels are critical for the generation of post-inhibitory low-threshold rebound spikes in thalamocortical neurons[69,163]. A computational study by Destexhe *et al.*[254] showed that membrane voltage trajectories of low-threshold rebound spikes in thalamocortical neurons can be recapitulated using a 3-compartment model, but not a single-compartment model. A recent study by Amarillo *et al.*[250] used pharmacological approaches to identify seven intrinsic channels (I_T, I_h, I_A, I_{Kir}, I_{NaP}, I_{NaLeak}, I_{KLeak}) contributing to the resting membrane potential of thalamocortical neurons. The same study created a single-compartment computational model neuron that produced thalamocortical neuron rebound bursting and showed that a balance between the 5 voltage-dependent channels shapes the low-threshold rebound spike.

Our model thalamocortical neurons extend the studies by Destexhe *et al.*[254] and

Amarillo *et al.*[250]. That is, we incorporated the same intrinsic channels described by Amarillo *et al.*[250], but allowed channel density to vary across three compartments [note that the two different leak channels in Amarillo *et al.* were simplified by combining them into a single passive leak conductance (g_{pas}) with a reversal potential (E_{pas})]. Furthermore, we established a different model neuron for each set of single thalamocortical neuron recordings, in an effort to capture the heterogeneity in response to physiologically relevant inhibitory inputs such as $GABA_B$ receptor-mediated IPSCs (Figure 3). By creating a set of 31 well-fitted model neurons, we were also able to generate population statistics that were in many ways similar to those of the corresponding population of recorded neurons (Figure 4).

We found that the well-fitted neurons, despite having fitted to IPSC responses that were widely heterogeneous in both LTS probability and latency, two parameters were highly convergent. *First*, T channel densities were always higher in the dendrites than in the soma (Figure 3F). This observation is in agreement with prior computational and experimental work[255,256,254,257]. In fact, as shown in Figure 5C, the relative magnitude of T currents during the LTS in all of our well-fitted models was negligible in the soma relative to that in the dendrites. Further, even after reducing the somatic T currents to zero, there was no visible change in the LTS responses (data not shown). Thus, our simulations suggest that the LTS response in the soma that ultimately results in a burst of action potentials is highly dependent on dendritic input currents. *Second*, A-type potassium channel densities were always highest in the soma (Figure 3F). As A channels are important for controlling the amplitude and width of the LTS response, but not for initiation [250], we focused on the relationship between inhibition and T channel opening in this study. Nevertheless, the striking similarity of the sum of the T and A currents ($I_T + I_A$) versus the total currents

provided by intrinsic channels ($I_{Intrinsic}$) suggests that these two currents work in opposition to shape the LTS response (Figure 5A-B, [289]). The degree to which modulation of the A channel influences thalamocortical neuron bursting has yet to be explored.

Perhaps more interestingly, our model neuron allowed us to identify a novel mechanism in which inhibition kinetics regulate T channel opening. We discovered a pronounced lag between the instantaneous and steady-state T channel inactivation curves ($_T$ versus $_{T,\infty}$) during *s*GAT1-Block and *s*GAT3-Block waveforms, but not during *s*Dual-Block waveforms. As this lag was difficult to visualize and was only important when the activation (m_T) was also high, we computed the instantaneous T channel open probability ($m_T{}^2$ $_T$) versus its steady-state ($m_{T,\infty}{}^2$ $_{T,\infty}$) and resolved a high discrepancy during *s*GAT1- and *s*GAT3-Block waveforms, but not during *s*Dual-Block waveforms. Across all $GABA_B$ *s*IPSC responses, the maximum difference between instantaneous versus steady-state T channel open probability predicted the presence of an LTS response (Figure 5E). Indeed, upon bidirectional manipulation of T channel inactivation time constant, congruent, bidirectional changes in T channel open probability discrepancy and LTS production were observed (Figure 6A-B). We thus propose that future efforts in modulating thalamocortical rebound bursting can be directed at modulating the T channel inactivation time constant.

In order to confirm that inhibition kinetics influence LTS production by controlling T channel opening, we varied the $GABA_B$ *s*IPSC waveform systematically five different ways (Figure 6C-G). In each case, an LTS was only produced when there was both sufficient T channel recovery and an increase in T channel open probability discrepancy. We concluded that a high inhibition amplitude was required for sufficient T channel recovery, but fast inhibition kinetics was required for driving T channel open probability discrepancy

past the threshold for LTS production. Collectively, the results of these manipulations (*c.f.* Figures 6F and 6G) support the hypothesis that dual GAT1+GAT3 blockade eliminates thalamic oscillations by promoting sustained, $GABA_B$ receptor-mediated inhibition that, in turn, promotes a convergence of instantaneous and steady-state T channel open probabilities, a state that results in LTS failure.

Implication on anti-epileptic therapies

Drugs that increase synaptic inhibition in the brain may paradoxically exacerbate generalized seizures. For example, the GAT1 blocker tiagabine increases extracellular GABA concentrations[220] and is an effective anti-epileptic drug used to treat focal epilepsy[290,291]. However, tiagabine can also induce continuous SWDs (i.e. absence status epilepticus) in patients with absence epilepsy[277] and non-convulsive status epilepticus in patients with focal epilepsy[228,229]. GAT1 knockout mice, which have increased inhibitory currents, and presumed increased activation of $GABA_B$ receptors[220] in thalamocortical neurons, also exhibit increased incidence of SWDs[66]. Furthermore, application of $GABA_B$ receptor antagonists increases seizures in rats susceptible to convulsive focal seizures, but suppresses seizures in rats with non-convulsive absence seizures[271]. Together, these observations suggest that, although a seizure is a manifestation of hyperexcitable neuronal firing, increasing inhibition in the form of neuronal hyperpolarization may not always reduce seizures[94].

In fact, as we discovered in this study, the temporal envelope of inhibition seems to play an important role in determining whether thalamocortical rebound bursts and seizure-like oscillations occur. Although the finding that dual GAT1+GAT3 blockade abolished epileptiform oscillations may at first glance suggest that nonspecific GABA transporter

blockers may be used to treat generalized seizures, this approach would be relatively non-specific, including for example, disrupting normal spindle oscillation formation, leading to undesirable side effects. Nevertheless, it is possible that temporary, pharmacological enhancement of GABA transporter expression or function may create pockets of IPSC response heterogeneity in the overall thalamocortical neuron population, making it less likely for the thalamic network to develop a hypersynchronous state[114].

Materials and Methods

Oscillation recordings in acute thalamic slices

Sprague-Dawley rats (Charles River Laboratories, Wilmington, MA) of postnatal day 11 to 17 (P11-P17), of either sex, were used in oscillation experiments, which were performed in accordance with protocols approved by the Institutional Animal Care and Use Committee at the University of Virginia (Charlottesville, VA). Rats were deeply anesthetized with pentobarbital, then transcardially perfused with ice-cold protective recovery solution containing the following (in mM): 92 NMDG, 25 glucose, 5 Na-ascorbate, 3 Na-pyruvate, 2.5 KCl, 2 thiourea, 20 HEPES, 26 $NaHCO_3$, 1.25 NaH_2PO_4, 0.5 $CaCl_2$, 10 $MgSO_4$, titrated to a pH of 7.3-7.4 with HCl[292]. Horizontal slices (400 µm) containing the thalamus were cut in ice-cold protective recovery solution using a vibratome (VT1200, Leica Biosystems, Wetzlar, Germany). Slices were trimmed to remove the hippocampus and the hypothalamus, and then transferred to protective recovery solution maintained at 32-34°C for 12 min. Brain slices were kept in room temperature ACSF consisting of the following (in mM): 126 NaCl, 2.5 KCl, 10 glucose, 26 $NaHCO_3$, 1.25 NaH_2PO_4, 2 $CaCl_2$, and 1 $MgSO_4$. All solutions were equilibrated with 95% O_2/5% CO_2.

Slices were placed in a humidified, oxygenated interface recording chamber and

perfused with oxygenated ACSF (2 mL/min) at 32-34°C. 10 μM bicuculline was added to the ACSF (bicuculline-ACSF) to block $GABA_A$ receptors. Oscillations were evoked by a square voltage pulse (10 V, 0.5 ms duration) delivered once every 60 seconds through two parallel tungsten electrodes (50-100 kΩ, FHC) 50-100 μm apart and placed in either the internal capsule or the reticular thalamus, which stimulated traversing corticothalamic and thalamocortical axons. Extracellular potentials were recorded in a differential manner with two tungsten electrodes (50-100 kΩ, FHC) by placing one in the somatosensory ventrobasal nuclei of the thalamus close to the stimulating electrode and one far away from the stimulating electrode. One experiment was performed per slice. Multi-unit recordings were amplified 10,000 times with a P511 AC amplifier (Grass), digitized at 10 kHz with Digidata 1440A, band-pass filtered between 100 Hz and 3kHz, and acquired using Clampex 10.7 software (Molecular Devices, San Jose, CA).

After at least 20 minutes in baseline bicuculline-ACSF, slices were perfused with one of 4 possible solutions: (1) bicuculline-ACSF, (2) bicuculline-ACSF plus 4 μM NO-711 to block GAT1 transport[275], (3) bicuculline-ACSF plus 100 μM SNAP-5114 to block GAT3 transport[276] or (4) bicuculline-ACSF plus a combination of 4 μM NO-711 and 100 μM SNAP-5114 to simultaneously block both GAT1 and GAT3. After 40 minutes, the perfusion solution was switched back to bicuculline-ACSF for at least 20 minutes.

Dynamic clamp recordings

Male Sprague-Dawley rats of postnatal day 11 to 15 (P11-P15) were used in dynamic clamp experiments, which were performed in accordance with protocols approved by the Administrative Panel on Laboratory Animal Care at Stanford University (Palo Alto, CA). Rats were deeply anesthetized with pentobarbital, then brains were rapidly extracted

and placed in ice-cold protective recovery solution containing the following (in mM): 34 sucrose, 2.5 KCl, 11 glucose, 26 $NaHCO_3$, 1.25 NaH_2PO_4, 0.5 $CaCl_2$, and 10 $MgSO_4$, titrated to a pH of 7.4 with HCl. Horizontal slices (300 μm) containing the thalamus were cut in ice-cold protective recovery solution using a vibratome (VT1200, Leica Biosystems). Slices were transferred to artificial cerebrospinal fluid (ACSF) maintained at 32°C for 45-60 min, then gradually brought to room temperature. The ACSF contained the following (in mM): 126 NaCl, 2.5 KCl, 10 glucose, 26 $NaHCO_3$, 1.25 NaH_2PO_4, 2 $CaCl_2$, and 1 $MgSO_4$. All solutions were equilibrated with 95% O_2/5% CO_2.

Slices were placed in a submerged recording chamber and perfused with oxygenated ACSF (2 mL/min) at 32-34°C. The chamber contained nylon netting which suspended the slice 1-2 mm from the chamber floor and enhanced slice perfusion. Slices were visualized with Dodt-contrast optics (Luigs & Newmann, Ratingen, Germany) on an Axioskop microscope (Zeiss, Pleasanton, CA). Recordings were obtained with a MultiClamp 700A patch amplifier (Molecular Devices), digitized with Digidata 1322A and acquired using Clampex software. Borosilicate glass pipettes (1.5-3 MΩ) pulled on a P-87 micropipette puller (Sutter Instruments, Novato, CA) were filled with an internal solution containing (in mM): 100 potassium gluconate, 13 KCl, 10 EGTA, 10 HEPES, 9 $MgCl_2$, 2 Na_2-ATP, 0.5 Na-GTP, 0.07 $CaCl_2$ (pH 7.4).

Dynamic clamp experiments were conducted using a computer running the RealTime Application Interface for Linux (RTAI, www.rtai.org) sampling the intracellular potential at 50 kHz. Custom-written software modified from previous work[293] used the sampled membrane potential and the pre-specified $GABA_B$-mediated inhibitory conductance to, at every timestep, update the inhibitory current that was injected into the thalamocortical neuron at 50 kHz. All measured voltages were corrected for a junction

potential of -10 mV.

Inhibitory conductance waveforms (*d*Control, *d*GAT1-Block, *d*GAT3-Block, *d*Dual-Block, Figure 2B) for use in dynamic clamp experiments were created based on previous recordings of $GABA_B$-mediated IPSCs[220]. In the previous study, voltage-clamped thalamocortical neurons were recorded during electrical stimulation of presynaptic reticular thalamic neurons while the thalamic slices were bathed in ionotropic glutamate receptor and $GABA_A$ antagonists to isolate $GABA_B$-mediated IPSCs. After acquiring baseline data, one of three drugs was added to the perfusing ACSF: 4 µM NO-711 to block GAT1, 100 µM SNAP-5114 to block GAT3, or both 4 µM NO-711 and 100 µM SNAP-5114 to block both GAT1 and GAT3[275,276]. After at least 10 minutes of drug perfusion and stabilization of drug effect, a series of $GABA_B$-mediated IPSCs was acquired. In the present study, we converted the previously obtained averaged IPSCs for each drug condition into a conductance waveform fitted with the equation:

$$g_{GABA_B} = A(1 \quad e^{-t/\tau_{rise}})^8(we^{-t/\tau_{fallfast}} + (1 \quad w)e^{-t/\tau_{fallslow}})$$

where A is the amplitude coefficient, τ_{rise} is the rise time constant, $\tau_{fallfast}$ and $\tau_{fallslow}$ are the fast and slow decay constants, respectively, and w is the weighting factor for the two decay terms[294]. The percent change in each parameter from baseline to drug condition was computed for each experiment. Baseline-normalized parameter values were compared between conditions, and for parameters with significant population differences in values ($p < 0.05$, Wilcoxon signed rank test), the mean change in parameter value was found and implemented for that drug condition. For parameters that did not change significantly in the drug condition compared to baseline, the parameter value was kept identical to that of the baseline (*d*Control) condition for the templates (Figure 2B). Parameter values for the four experiment conditions (*d*Control, *d*GAT1-Block, *d*GAT3-Block,

*d*Dual-Block) are listed in Table 1. A value of -115 mV was used to for the reversal potential associated with the GIRK conductance following post-synaptic $GABA_B$ receptor activation.

Since the number of $GABA_B$ receptors activated in a physiological setting was not determined, all $GABA_B$ IPSC waveforms (*d*IPSCs) had amplitude scaled between 25%-800%. A total of 5-15 repetitions were performed for each *d*IPSC waveform, with a holding current adjusted at the beginning of each recording so the holding membrane potential is in the range of -73 to -60 mV. For each sweep, a brief current pulse (-50 pA, 10 ms) was applied at around 100 ms to assess electrode resistance and passive membrane properties, then the *d*IPSC was applied at 1000 ms.

	A	τ_{rise}	$\tau_{fallfast}$	$\tau_{fallslow}$	w
*d*Control	16.00	52.00	90.10	1073.20	0.952
*d*GAT1-Block	24.00	52.00	90.10	1073.20	0.952
*d*GAT3-Block	8.88	38.63	273.40	1022.00	0.775
*d*Dual-Block	6.32	39.88	65.80	2600.00	0.629

Table 1. Parameter values of $GABA_B$-mediated inhibitory conductance waveforms used in dynamic clamp experiments. These values (with the amplitudes scaled by 200%) correspond to the conductance templates shown in Figure 2B. A, amplitude coefficient; τ_{rise}, rise time constant; $\tau_{fallfast}$, fast decay time constant; $\tau_{fallslow}$, slow decay time constant; w, weighting factor for the two decay terms.

Analysis of oscillation recordings

MATLAB R2018a (MathWorks, Natick, MA) was used for all data analysis. Single action potential *spikes* were detected from raw multi-unit activity as follows[196]. The raw signal was first bandpass-filtered between 100-1000 Hz. Slopes between consecutive sample points were computed from the filtered signal. For each sweep i, the baseline slope noise α_i was computed from the root-mean-square average of the slope vector over the

baseline region before stimulation start, and the maximum slope β_i was defined as the maximum slope value at least 25 ms after stimulation start (to account for the stimulus artifact). For each slice, if $\alpha = \sum_i \alpha_i$ is the baseline slope noise averaged over all sweeps and $\beta = \sum_i \beta_i$ is the maximum slope averaged over all sweeps, then the slice-dependent signal-to-noise ratio was given by $r = 1 + 0.1(\frac{\beta}{\alpha} \quad 1)$. The resulting signal-to-noise ratios fell between 2-5. A sweep-dependent slope threshold was then defined by $\theta_i = r\alpha_i$. Finally, single spikes were defined as all local maxima of the slope vector at least 25 ms after stimulation start with values exceeding a slope threshold.

To compute the oscillation duration for each sweep, spikes were first binned by 10 ms intervals to yield a spike histogram. Evoked *bursts* were detected by joining consecutive bins with a minimum spike rate of 100 Hz, using a minimum burst length of 60 ms, a maximum delay after stimulation start of 2000 ms and a maximum inter-burst interval of 2000 ms (Figure 1A). The *oscillation duration* was defined as the time difference between the end of the last evoked burst and stimulation start.

To compute the oscillation period for each sweep, an autocorrelation function (ACF) was first computed from the binned spikes, then moving-average-filtered using a 100 ms window. Peaks (local maxima) were detected from the filtered ACF using a minimum peak prominence that is 0.02 of the amplitude of the primary peak (the first value of the ACF). Peaks with lags greater than the oscillation duration were ignored. The *oscillation period* was computed by searching for the lag value δ that minimizes the distance function $f(\delta) = \sum_j |p_j \quad q_j(\delta)|$, where p_j is the lag value of peak j and $q_j(\delta)$ is the closest multiple of δ to p_j. The search was initialized with the estimate $\delta_0 = p_2 \quad p_1$ and confined to the bounds $\left[\frac{2}{3}\delta_0, \frac{3}{2}\delta_0\right]$.

An *oscillatory index* [293] was also computed from the filtered autocorrelation function (fACF). For each sweep, the non-primary peak with largest fACF value was designated as the secondary peak. The *oscillatory index* was then defined by $OI = (A_{peak2} \quad A_{trough})/(A_{peak1} \quad A_{trough})$, where A_{peak1} is the fACF value of the primary peak, A_{peak2} is the fACF value of the secondary peak and A_{trough} is the minimum fACF value between the primary peak and the secondary peak.

The average oscillation duration or period at the end of each phase (baseline or drug) was computed by choosing the 5 values from the last 10 sweeps of each phase that were within 40% of the average of the group of values. This approach was used to minimize bias caused by abnormally-shortened evoked oscillations due to the presence of spontaneous oscillations.

Analysis of dynamic clamp recordings

MATLAB R2018a was used for all data analysis. Responses to *d*IPSCs were analyzed as follows: All voltage traces were manually examined and noisy recordings were excluded. The peak of the current trace (IPSC peak) within the first 300 ms of *d*IPSC start was first detected. The most likely candidate for a calcium-dependent low-threshold spike (LTS) was then detected from the raw voltage trace in between the time of IPSC peak and 7000 ms after *d*IPSC start.

To detect the *LTS candidate*, the voltage trace was first median-filtered with a time window of 30 ms to remove action potentials[295], then moving-average-filtered with a time window of 30 ms. First and second derivatives of the doubly-filtered voltage traces were computed by differences between consecutive sample points, and the first derivative vector was moving-average-filtered with a time window of 30 ms before taking the second

derivative. The local maximum of the doubly-filtered voltage trace with the most negative second derivative was chosen as the LTS candidate. A histogram of LTS candidate second derivatives for traces was fitted to a sum of 3 Gaussian distributions and the minimum of the probability density function between the first two peaks was used as a second derivative threshold.

Features were computed for each LTS candidate. The LTS *peak value* was the absolute voltage value for the peak. The LTS *latency* was defined by the time difference between the LTS peak time and *d*IPSC start. A time region that was bounded by the first local minimum of the doubly-filtered voltage trace on either side of the peak was used to compute the LTS *maximum slope* and detect action potentials. For accuracy, the slope value was computed from a different doubly-filtered trace with a smaller moving-average-filter time window corresponding to roughly a 3 mV-change in amplitude for that trace. Action potentials spikes were detected by a relative amplitude threshold 10 mV above the LTS amplitude for that trace.

An LTS candidate was then assigned as an *LTS* if the following criteria were all satisfied: (1) Peak prominence must be greater than the standard deviation of the filtered voltage values before IPSC start; (2) Peak second derivative must be more negative than the threshold (-0.0023 V^2/s^2) described above; (3) If there were action potentials riding on the LTS, the LTS peak time must occur after the time of the first action potential. Detection results were manually examined by blinded experts and the algorithm's decision for LTS determination was overturned only if 3 of the 4 polled electrophysiology experts agreed. The *LTS or burst probability* was defined as the proportion of traces producing an LTS or a *burst* (an LTS with at least one riding action potential) across all 5-15 repetitions (with varying holding potentials) for a particular $GABA_B$ IPSC waveform.

Single thalamocortical neuron models

All computational simulations were performed using NEURON[296] version 7.5 with a temperature of 33°C. Each model thalamocortical neuron had one cylindrical somatic compartment (Soma) and two cylindrical dendritic compartments (Dend1 and Dend2) in series (Figure 3C). The somatic length and diameter were set to be equivalent with the parameter $diam_{soma}$. The two dendritic compartments were set to have equal diameters ($diam_{dend}$), with each having lengths equal to half of the parameter L_{dend}. Values for specific membrane capacitance and axial resistivity were equivalent to those reported by Destexhe *et al.*[254]. Passive leak channels were inserted in all three compartments at equivalent densities (g_{pas}) with a fixed reversal potential of -70 mV. The 4 voltage-independent (*passive*) parameters described above were allowed to vary across neurons.

The following mechanisms were inserted in all 3 compartments: the T-type calcium current (I_T) and the submembranal calcium extrusion mechanism (Ca_{decay}) was adapted from Destexhe et al. (1998); the hyperpolarization-activated nonspecific cationic current (I_h), the A-type transient potassium current (I_A), the inward-rectifying potassium current (I_{Kir}) and the persistent sodium current (I_{NaP}) were adapted from Amarillo et al. (2014). The following parameters were allowed to vary across compartments and across neurons: the maximum permeability $\bar{p}_T$ (in cm/s) of I_T, which was described by the Goldman–Hodgkin–Katz flux equation[247], and the maximum conductance densities $\bar{g}_h$, $\bar{g}_A$, $\bar{g}_{Kir}$, $\bar{g}_{NaP}$ (in S/cm^2) of other currents described by Ohm's law. All parameters that were not varied during optimization were identical for all model neurons and taken from literature values. Based on calculations from solutions used in experiments, the potassium reversal

potential was -100 mV, the sodium reversal potential was 88 mV, the calcium concentration outside neurons was 2 mM and the initial calcium concentration inside neurons was 240 nM.

All intrinsic current mechanisms were described by Hodgkin-Huxley type equations with voltage and/or time-dependent activation (m) and inactivation ( ) gating variables and have been described in detail in the corresponding sources[250,254]. In particular, the open probability of I_T was described by $m(V,t)^2$ (V,t)[143]. At every point in time, the activation variable m converges exponentially to its steady-state value $m_\infty(V)$ with a time constant $\tau_m(V)$ and the inactivation variable converges exponentially to its steady-state value $_\infty(V)$ with a time constant $\tau_h(V)$. The equations for $m_\infty(V)$, $\tau_m(V)$, $_\infty(V)$ and $\tau_h(V)$ were fitted from electrophysiological recordings and described by Huguenard & McCormick[247].

For simulations involving action potentials, a fast sodium and potassium mechanism adapted from Sohal and Huguenard[195] was inserted in the somatic compartment and made identical across neurons. Based on the comparison of the number of spikes per LTS between model neurons and corresponding recorded neurons (Figure 4A-B), the threshold parameter V_{Traub} was changed to -65 mV.

A custom $GABA_B$ receptor mechanism was inserted in the somatic compartment that produced IPSCs with the equation form given by Eq1. The parameters used were identical to that used for dynamic clamp, with kinetics varying for each pharmacological condition as in Table 1. Although parameter measurements were performed at a same temperature (33 °C) as simulations, a Q_{10} of 2.1[294] was included in the model.

All simulations performed for each model neuron were matched to traces recorded using dynamic clamp for the corresponding recorded neuron as follows: To

match the holding potentials, we first performed a test simulation to voltage clamp the model neuron (with initial potential -70 mV) for 2 seconds to bring it to a quasi-steady state. The resultant steady-state current was used as holding for the current clamp simulation. To simulate dynamic clamp of the recorded neuron, after 2 seconds to allow state variables in the model to stabilize, a brief current pulse (-50 pA, 10 ms) was applied at around 2.1 seconds, then an *s*IPSC identical to the *d*IPSC applied in dynamic clamp was applied at 3 seconds. The analysis of LTS and burst features for simulated *s*IPSC responses is identical to that for recorded *d*IPSC responses.

Parameter initialization

Initial values for *passive parameters* were different for each model neuron and were estimated from the current pulse responses from the corresponding recorded neuron by a strategy adopted from Johnston and Wu[280]. A portion of raw current pulse responses had a systematic voltage shift at the beginning and end of the pulse, consistent with an unbalanced bridge. These shifts were detected by a slope threshold determined through a histogram of all initial slopes and then corrected by shifting the entire portion of the response during the brief current pulse, by the calculated amount. The corrected current pulse responses for a particular neuron were then fitted to the following first order response equation with 2 exponential components:

$$V(t) = [C_0(1 \quad e^{-t/\tau_0}) + C_1(1 \quad e^{-t/\tau_1})]B(t \le t_p) +$$
$$[C_0(1 \quad e^{-t_p/\tau_0})e^{-(t-t_p)/\tau_0} + C_1(1 \quad e^{-t_p/\tau_1})e^{-(t-t_p)/\tau_1}]B(t > t_p),$$

where C_0, C_1 are the amplitudes (in mV) of the two components, τ_0, τ_1 are the time constants (in ms) of the two components, $t_p = 10$ ms is the width of the current pulse, and $B(x)$ is a Boolean function defined by $B(x) = 1$ if $x = \text{true}$ and $B(x) = 0$ if

$x = \text{false}$. Initial values for the curve fit were $C_{0,i} = \quad V$, $C_{1,i} = \quad V$, $\tau_{0,i} = 10\ \text{ms}$, $\tau_{1,i} = 1\ \text{ms}$ where V is the mean voltage change for the neuron after each 10 ms stimulus.

Next, given the fitted coefficients, we estimated the defining parameters for a ball-and-stick model. The input resistance was computed by

$$R_{Input} = (C_0 + C_1)/I_p,$$

where $I_p = 50\ \text{pA}$ is the amplitude of the current pulse. The membrane time constant τ_m was set to equal that of the slow component $\tau_m = \tau_0$. The length constant was computed by solving for L in equation 4.5.57 of Johnston and Wu[280]:

$$\left|C_1/\left((2C_0\tau_1/\tau_0) \quad C_1\right)\right| = \cot(\alpha_1 L)[\cot(\alpha_1 L) \quad 1/\alpha_1 L],$$

where $\alpha_1 = \left((\tau_1/\tau_0) \quad 1\right)^{1/2}$, starting with the initial guess of $L_i = \pi/\alpha_1$. The dendritic-to-somatic conductance ratio ρ was then computed by equation 4.5.58 of Johnston and Wu[280]:

$$\rho = \quad \alpha_1 \cot(\alpha_1 L)/\coth(L).$$

Finally, we converted the defining ball-and-stick parameters to initial estimates for the passive parameters in our 3-compartment NEURON model that are optimized. The input resistances of the soma and the dendrite were computed by

$$R_{Memb} = R_{Input} \quad R_s,\ R_{Soma} = (1+\rho)R_{Memb},\ R_{Dend} = R_{Soma}/\rho,$$

where R_s is the series resistance. The specific membrane resistivity R_m was computed by equation 4.3.3 of Johnston and Wu[280]:

$$R_m = \tau_m/C_m,$$

where a fixed value of 0.88 µF/cm^2 [254] for the specific membrane capacitance C_m. Then the somatic diameter $diam_{Soma}$ was computed by equation 4.3.8 of Johnston and Wu:

$$diam_{Soma} = 2\sqrt{R_m/4\pi R_{Soma}},$$

the dendritic diameter $diam_{Dend}$ was computed by equation 4.5.47 of Johnston and Wu:

$$diam_{Dend} = \left(2\sqrt{R_m R_a}(\coth L)/\pi R_{Dend}\right)^{2/3},$$

where a fixed value of 173 Ω·cm[254] for the axial resistivity R_a, the dendrite length L_{Dend} was computed by equation 4.4.15 of Johnston and Wu[280]:

$$L_{Dend} = L\sqrt{diam_{Dend} R_m/4R_a},$$

and the passive conductance g_{pas} was estimated by

$$g_{pas} = 1/R_{Input}A,$$

where $A = \pi\left(diam_{Soma}{}^2 + diam_{Dend}L_{Dend}\right)$ is the total surface area of the neuron.

Initial values for *active parameters* were identical for all model neurons and were taken from literature values[250,261] as follows: $\bar{p}_{T,Soma} = \bar{p}_{T,Dend1} = \bar{p}_{T,Dend2} = 2.0 \text{ x } 10^{-4}$ cm/s, $\bar{g}_{h,Soma} = \bar{g}_{h,Dend1} = \bar{g}_{h,Dend2} = 2.2 \text{ x } 10^{-5}$ S/cm^2, $\bar{g}_{Kir,Soma} = \bar{g}_{Kir,Dend1} = \bar{g}_{Kir,Dend2} = 2.0 \text{ x } 10^{-5}$ S/cm^2, $\bar{g}_{A,Soma} = \bar{g}_{A,Dend1} = \bar{g}_{A,Dend2} = 5.5 \text{ x } 10^{-3}$ S/cm^2 and $\bar{g}_{NaP,Soma} = \bar{g}_{NaP,Dend1} = \bar{g}_{NaP,Dend2} = 5.5 \text{ x } 10^{-6}$ S/cm^2.

Parameter optimization

The voltage responses of a model neuron to a set of 12 different $GABA_B$ IPSC waveforms (4 pharmacological conditions at 3 different conductance amplitude scales) was compared with the responses of the corresponding recorded neuron. To emphasize the LTS response, model neurons excluded fast sodium and potassium channels and the experimental responses were median-filtered with a time window of 30 ms to remove action potentials. As multiple objective functions were of interest[297], a total error E_{total} was computed by a weighted average of component errors (Figure 3E):

$$E_{total} = (w_m E_m + w_{sw} E_{sw} + w_a E_a + w_t E_t + w_{sl} E_{sl}) / \sum_i w_i,$$

where E_m is the average error across all traces for whether the presence or absence of LTS matches (if an LTS is missed an error of 18 is assigned; if an LTS is falsely produced an error of 6 is assigned), E_{sw} is the average root-mean-square error of voltage values, E_a is the average LTS peak value error across all LTS-matching traces, E_t is the average LTS latency error across all LTS-matching traces, E_{sl} is the average LTS maximum slope error across all LTS-matching traces, and the w_i's denote the corresponding weights. Based on the maximum LTS latency observed in recorded neurons, the fitting region was restricted to between 0-1.8 seconds after the start of the IPSC. Traces were also allowed to have different sweep weights, in which case the average across traces were computed using root-mean-square.

A modified version of the Nelder-Mead simplex algorithm[298] was used to update parameter values within defined parameter bounds, with the objective of minimizing E_{total}. For each simplex, the maximum number of iterations was 2000, the maximum number of error evaluations was 4000, the relative error tolerance was 0.1, the relative parameter change tolerance was 0.1, the coefficient of reflection was $\rho = 1$, the coefficient of expansion was $\chi = 2$, the coefficient of contraction was $\gamma = 0.75$, the coefficient of shrinkage was $\sigma = 0.8$. The initial simplex was set up so that each vertex deviates in a parameter to be varied by $\delta = 2/3$ of the parameter's total range. To transform values to an unconstrained parameter space so that the Nelder-Mead method could be applied, each bounded parameter value was first linearly transformed to the region $[\ \ 1, 1]$ than transformed to $(\ \ \infty, \infty)$ using the inverse tangent function.

A total of 21 different iterations were run to optimize each model neuron, with the

weights among different error types and weights among different traces varying from iteration to iteration. For some poorly fit neurons, the initial parameters for that neuron were replaced by the best-fit neuron's parameters from the previous iteration. One trace per $GABA_B$ IPSC waveform was used during model optimization, but all traces were used for the final model evaluation (Figure 3E).

Network Models

Each 2-cell network includes one single-compartment model reticular thalamic neuron, described in previous work[284], and one of the well-fitted, 3-compartment model thalamocortical neurons described earlier. The reticular thalamic neuron has an AMPA receptor that is synaptically activated by the thalamocortical neuron, and the thalamocortical neuron has a $GABA_B$ receptor in the somatic compartment that is synaptically activated by the reticular thalamic neuron. Synaptic currents were evoked with 100% probability and a delay of 1 ms whenever the presynaptic neuron reached a voltage threshold of -30 mV.

AMPA receptors were adapted from Sohal et al. (2000). Reflecting more recent physiological measurements[132], AMPA currents were adjusted to bring rise time to 0.5 ms, decay time to 5.6 ms and maximal conductance of 7 nS per synapse. The reversal potential for AMPA currents was maintained at 0 mV.

$GABA_B$ receptors were as described before for single model TC neurons. In order for overlapping IPSCs to be summed linearly, we expanded Eq1 into 18 terms, each having its own rise and decay exponential time constants. To be consistent with dynamic clamp experiments, a reversal potential of -115 mV was used in simulations, although the networks behave similarly if a reversal potential of -100 mV was used instead (data not

shown). Relative to the values used in dynamic clamp, the conductance amplitudes were scaled by 1/12 to account for temporal summation from an RT burst, and the synaptically-evoked IPSCs was verified to be comparable to recorded values (Figure 7B).

Each 200-cell network assumed a bilayer architecture, with one 100-cell circular layer of single-compartment model reticular thalamic neurons and one 100-cell circular layer of 3-compartment model TC neurons. The identity of the TC neuron was chosen from each of the 31 well-fitted model TC neurons. Each reticular thalamic neuron inhibited the nine nearest TC cells, whereas each TC neuron excited the five nearest reticular thalamic neurons [195]. The passive leak conductance of each model reticular thalamic neuron was randomly selected from a uniform distribution between 45 and 55 $\mu S/cm^2$ [195]. The passive leak conductance of each model TC neuron was randomly selected from a uniform distribution between -10% to 10% of the optimized value.

Network simulations were performed with leak reversal potentials and initial membrane potentials set to a value between -73 mV and -60 mV, at 1 mV increments, so that a total of 14 repetitions were applied for each model network. After a delay of 3 seconds to allow for state variable stabilization, either the reticular thalamic neuron in the 2-cell network or each of the center 20 reticular thalamic neurons in the 200-cell network was injected with a square current pulse (0.2 nA, 40 ms). Simulations were performed with a 0.1 ms integration time step and continued for a total of 30 seconds. Pooling all action potential spikes after stimulation end, we detected bursts and computed an oscillation period and an oscillatory index using the same algorithm as that for multiunit recordings, except for a bin width of 100 ms for spike histograms and a minimum peak prominence of 0.5 relative to the largest secondary peak for the filtered autocorrelation function. Oscillation probability was defined as the proportion of simulations (with varying

holding potentials) that induced oscillations with at least three bursts. Percent of active TC cells was defined as the percentage of model TC neurons in the network that produced at least one spike. Half activation latency was defined as the time it took for half of the final percentage of active cells to be activated. Mean oscillation period, mean oscillatory index and mean half activation latency were computed by restricting to trials with a successfully evoked oscillation.

Statistics

MATLAB R2019b was used for all statistical analysis. Since the number of available data points for LTS and burst features was significantly different for the Dual-Block condition, we performed a paired t-test or a signed-rank test between the Control condition and the Dual Block condition. We used either repeated-measures ANOVA or the Friedman's test for comparison across the Control, GAT1-Block and GAT3-Block conditions.

Paired comparisons were applied if not otherwise specified. Normality of the differences to the within-subject mean was assess for all groups using a combination of the Lilliefors test, the Anderson-Darling test and the Jarque-Bera test. Normality was satisfied when the geometric mean of three p values was at least 0.05 for all groups. When normality was satisfied, the paired-sample *t*-test was used when there are two groups and repeated-measures ANOVA (with multiple comparison) was used when there are more than two groups. When normality was not satisfied, the Wilcoxon signed-rank test was used when there are two groups and Friedman's test (with multiple comparison) was used when there are more than two groups. Tests were two-tailed with a significance level of 0.05. Error bars reflect 95% confidence intervals. All violin plots used a bandwidth that was 10% of the maximum data range.

Drugs

Bicuculline methiodide was purchased from Sigma-Aldrich (St. Louis, MO). The GAT1 blocker NO-711 [(1,2,5,6-tetrahydro-1-[2-[[(diphenylmethylene)amino]oxy]ethyl]-3-pyridinecarboxylic acid hydrochloride] and GAT3 blocker SNAP-5114 [1-[2-[tris(4-methoxyphenyl)methoxy]ethyl]-(S)-3-piperidinecarboxylic acid] were purchased from Tocris Bioscience (Minneapolis, MN).

Code

Data analysis, data visualization, statistical tests, NEURON model setup and NEURON model optimization were performed using custom MATLAB code. All code for reproducing results (including NEURON .hoc, .tem and .mod files used) are available online at https://github.com/luadam4c/m3ha_published/.

Chapter 3: Conclusion and Future Directions

Research goals achieved

Combining experimental and computational approaches, I discovered a nonlinear interaction between physiological inhibition and both thalamocortical bursting and thalamic network oscillations. In response to increased amplitude and duration of $GABA_B$ IPSCs through individual GAT1 or GAT 3 blockade, thalamocortical rebound bursting was more robust and thalamic network oscillations were lengthened. However, in response to a further increase in $GABA_B$ IPSC duration through dual GAT1+GAT3 blockade, thalamocortical rebound bursting was less probable and thalamic network oscillations were eliminated. Furthermore, this nonlinear interaction persisted across conductance amplitude scales. Therefore, in addition to the overall level and amplitude of inhibition, the *kinetics* of inhibition appeared to be crucial for controlling intra-thalamic network oscillations.

By exploring computational models further, I described mechanistically how distinct inhibition waveforms control thalamocortical rebound bursting. Supported by the non-LTS producing responses of dual blockade IPSCs, increased hyperpolarization and increased removal of T channel inactivation was not sufficient for T channel opening. An increased discrepancy between instantaneous and steady-state T channel open probability driven by a combination of a slow T channel inactivation time constant and a fast voltage rise from a hyperpolarized state was also required. Although an interaction between voltage ramps and low threshold spikes has been previously described[263], I provided an explanation for this interaction by examining trajectory differences in the voltage versus

T channel open probability discrepancy phase plane. Furthermore, I have identified the time point at which the T channel open probability discrepancy reaches zero concavity as the decision point for LTS production. This understanding provides a framework for future studies on the control of LTS production.

Finally, my work has laid a foundation for future research on thalamocortical neuronal heterogeneity through the creation of 31 data-driven computational model neurons. Previous computational work on thalamic neurons typically creates a single model based on example or averaged experimental data[250,254]. In contrast, I attempted to generate a computational model neuron for each recorded neuron. As a result, the heterogeneity in the LTS and burst responses of thalamocortical neurons was and could be further explored as a function of intrinsic channel parameters. Furthermore, I was able to generate a TC-heterogeneous thalamic network model that was more robust and more realistically reflected oscillation differences across pharmacological manipulations.

In the rest of this chapter, I will discuss potential future directions that logically follow from this work.

Prediction of LTS production

As discussed previously, I have identified a decision point for LTS production using the T channel open probability discrepancy concavity (Figure 5F of Chapter 2). In short, if the concavity remained negative, no LTS will be produced. If the concavity reached zero, it either become positive and produce an LTS or become negative and caused an LTS failure. What factor causes the open probability discrepancy trajectory to go one way or the other at the decision point? In preliminary explorations of all available IPSC responses, there appeared to be a threshold for either the voltage slope value or the open probability

discrepancy slope value at the decision point that separates. Nevertheless, this threshold appeared to be neuron-dependent. Given the heterogeneity in neuronal parameters (Figure 3F of Chapter 2), one could potentially correlate and manipulate an intrinsic channel parameter with the slope threshold values and provide further mechanistic explanation of LTS production.

Implications of thalamocortical neuron heterogeneity

Responses to IPSCs across recorded neurons was highly heterogeneous, often with bimodal distributions (Figure 2D and Figure 4B of Chapter 2). The heterogeneity could be recapitulated by the model neurons (Figure 4A of Chapter 2), which are reflected in parameter heterogeneity (Figure 3F of Chapter 2). How can parameter heterogeneity explain response heterogeneity? Preliminary explorations correlating each LTS response feature with each individual parameter identified a strong relationship between LTS latency and HCN channel density. However, strong individual predictors of LTS probability, LTS amplitude and LTS maximum slope were not identified. Future exploration using generalized linear models and hierarchical clustering may identify combinations of parameters as strong predictors. Nevertheless, a mechanistic understanding would require manipulations on identified individual parameters or combinations of parameters. With the benefit of a population of heterogeneous model neurons that recapitulates the LTS response heterogeneity, one could artificially reduce the heterogeneity of a given set of parameters and measure the resulting change in the heterogeneity of a particular LTS response feature. Therefore, a brute-force approach iterating through all possible sets of parameters is another potential method for identifying predictors of LTS features.

Development of a physiologically-relevant thalamic network model

Spike-wave discharges have been modelled across several levels of complexity, from formal mathematical models to biophysically detailed networks[299]. In this work, I used biophysical, compartmental models to model the basic thalamic circuit. This level of complexity was necessary for the following two reasons: (1) to be able to dissect the effects of biophysical properties of individual channels and receptors on network oscillations; (2) to be able to introduce heterogeneity across neurons in the network. Although prior biophysical thalamic network models have captured several aspects of thalamic oscillations[259,300,301], they have not accounted for oscillation changes in response to varying RT-TC inhibition kinetics. Furthermore, prior models typically reduced all neurons of the same type to the same identical geometric and channel parameters, with the exception of leak conductance variability. The lack of cell parameter heterogeneity ignored observed electrophysiological response differences across thalamocortical neurons.

To better account for experimental data, I have updated the thalamic network model as follows: (1) a simplified model of the $GABA_B$ receptor was created that did not make any assumptions on intrinsic gating mechanisms, but rather utilized empirical IPSC conductance traces that were recorded under different pharmacological conditions; (2) a set of thalamocortical model neurons that accounted for electrophysiological response differences among recorded neurons was established and included in the same layer of the network.

There were two important effects with the inclusion of thalamocortical neuron heterogeneity. First, the percent of TC neurons activated was considerably smaller, and oscillations were more localized to an area of the network. Reduced activation percentage in the model network more realistically captures anecdotal findings in the acute thalamic

slice, where oscillations were often found to be localized to within a millimeter of a recording electrode. Furthermore, there is a possibility of sparse activation of thalamocortical neurons during absence seizures *in vivo*, which could explain the difficulty in intracellularly recording thalamic bursts during seizures[287]. Second, the variable rebound burst response profiles across individual thalamocortical neurons was averaged out in the network. The averaging of LTS latencies caused oscillation periods of TC-heterogeneous to be averaged relative to the corresponding TC-homogeneous networks. The resulting oscillation period values produced by the TC-heterogeneous networks were remarkably similar to experimentally observed values (Figure 1E and 8E of Chapter 2). The averaging of response profiles also caused network oscillations to be less variable from trial to trial. With increased robustness of the network responses, oscillation differences across pharmacological manipulations were more easily compared. The incorporation of biological variability also increased the reproducibility of results, in line with current recommendations[302].

Nevertheless, there was a major shortcoming of the current thalamic network model: variable oscillation durations were not recapitulated. In fact, most oscillations did not terminate with 27 seconds of simulations after stimulation, while experimentally recorded oscillations were usually no longer than 20 seconds. A prior thalamic model successfully modelled finite oscillation durations by including presynaptic depression of $GABA_B$ receptors upon repetitive activation. However, there is no experimental evidence of presynaptic $GABA_B$ receptors at RT-TC synapses, as immunohistochemical stains in the ventrobasal nucleus found that $GABA_B$ receptors were exclusively extrasynaptic[220]. Therefore, a more physiological explanation of how oscillations terminate in acute thalamic slices is warranted and could be explored in future iterations of the network model.

Role of heterogeneity in intrathalamic inter-neuronal synchrony

In mouse thalamic slices, simultaneous extracellular recordings of neighboring TC neurons upon a synchronized activation of RT neurons showed a synchronous timing for IPSP initiation but an asynchronous timing for rebound firing, both across TC neurons (rebound LTS heterogeneity) and across trials (rebound LTS jitter)[114]. What underlies the lack of inter-neuronal synchrony and apparent rebound LTS heterogeneity in TC neurons? There are three possibilities:

(1) Heterogeneity in RT-TC synapses could, through a differential expression of synaptic $GABA_A$ receptors, extrasynaptic $GABA_A$ receptors and $GABA_B$ receptors, result in differences in IPSP amplitude and kinetics across TC neurons (RT-TC IPSP heterogeneity) that can impact their respective rebound LTS timing or jitter[114,117].

(2) Heterogeneity in intrinsic currents across TC neurons could lead to differential interactions with similar IPSPs and directly result in rebound LTS heterogeneity. In fact, dynamic clamp recordings showed high variability in the LTS latencies (Figure 2D of Chapter 2). The HCN channel density in the proximal dendrite was found to be negatively correlated with LTS latency, in corroboration with previous studies[293].

(3) The lateral inhibition architecture discussed in Chapter 1 could amplify rebound LTS jitter and heterogeneity[114]. Specifically, since rebound LTSs in TC neurons occur at different times, a polysynaptic IPSP (through lateral inhibition) evoked by the firing of an earlier-rebounding TC neuron could suppress a would-be rebound LTS, introducing further uncertainty in the rebound LTS timing of neighboring TC neurons.

Which of the three mechanisms is most important? In support of (3), when simultaneous recording of neighboring TC neurons (see above), blocking polysynaptic excitation

with NBQX (an AMPA receptor antagonist) and APV (an NMDA receptor antagonist) reduced the rebound LTS jitter for each TC neuron by 50% and also increases its probability and speed, demonstrating that the lateral inhibition architecture played an important role in desynchronizing network activity[114]. In further support of (3), bath application of NBQX or APV shortened the duration of evoked spindle oscillations in rat thalamic slices[221]. Nevertheless, there was still rebound LTS heterogeneity across neighboring TC neurons even after blocking lateral inhibition[114], which demonstrates that either (1) or (2) must be valid mechanisms as well.

To tease apart these three mechanisms, one could use the TC-heterogeneous thalamic network model with $GABA_A$ receptors reinstated. Neurons could be randomly activated in the model and the inter-neuronal synchrony could be evaluated across TC neurons over time. A manipulation in the relative strength of $GABA_A$ versus $GABA_B$ receptors could test (1), a choice of different combinations of TC neurons could test (2) and a manipulation in the strength of intra-RT inhibition could test (3).

Role of hypersynchrony in absence seizures

Absence seizures are electrographically defined by high amplitude spike-wave discharges that represent hyper-synchronized, oscillatory activity among neurons[10]. *In vivo* multi-site recordings have revealed that action potentials in most thalamic regions are largely synchronized with the spike of spike-wave discharges[92]. Nevertheless, how intra-thalamic neuronal hypersynchrony arises and its role in the initiation, maintenance and termination of absence seizures remain largely unanswered.

Are seizures always reflective of hypersynchrony at the action potential level? One study of human focal seizures found inter-neuronal hypersynchrony only in the initial 20

ms period of spike-wave complexes and that the increase in synchrony largely resulted from a transient increase in spiking rates[303]. Therefore, synchrony may not be important for the maintenance of seizures. In fact, a study of rodent spike-wave discharges found that the peak frequency of SWDs actually *decreased* monotonously from about 10 Hz at the beginning to 8 Hz at the end[304]. A decrease in inter-neuronal synchrony from cycle to cycle may even contribute to the eventual termination of seizures. An interesting future direction would test this hypothesis in the setting of intra-thalamic oscillations, using both recordings in acute thalamic slices and the thalamic network model.

On the other hand, there is evidence that hypersynchrony may be involved in the initiation of seizures. A simultaneous EEG-functional MRI study of human spike-wave discharges found an increase in inter-regional synchrony 2 seconds before seizure onset[305]. Whether there is a similar increase in inter-neuronal synchrony at the action potential level remains unknown. Using tetrode recordings in the rats, a study found that local interneurons in the hippocampus displayed increased synchronization before the onset of pilocarpine-induced seizures[306]. Although similar in vivo studies have not been done for absence seizures, one could first examine inter-neuronal synchrony in the acute thalamic slice. When perfused with bicuculline and either NO-711 (a GAT1 blocker) or SNAP-5114 (a GAT3 blocker), paroxysmal (epileptiform) thalamic oscillations do not always have to be electrically-evoked, but often spontaneously arise. Therefore, an interesting future direction would test the hypothesis that inter-neuronal synchrony increases right before the appearance of spontaneous oscillations, is highest at the beginning of oscillations and gradually decrease over time.

What about the role of hypersynchrony in the transition from normal spindle oscillations to abnormal spike-wave discharges? Again, one could start with answers in the

acute thalamic slice. There appears to be a change in inter-neuronal synchrony as oscillations transition from spindle-like oscillations to paroxysmal oscillations in the acute thalamic slice. In my preliminary experiments, bursts appeared irregular when the perfusate consists of only artificial cerebrospinal fluid (aCSF), but gradually increased in regularity as bicuculline (a $GABA_A$ receptor blocker) is washed on, and reversed back as bicuculline is washed off. How much the increase in burst regularity can be accounted for by increased inter-neuronal synchrony as opposed to increased neuronal recruitment remains unknown. Nevertheless, evoked oscillations gradually lengthened as bicuculline was washed on, and spontaneous oscillations only appeared in when slices were bathed in bicuculline. Therefore, some level of hypersynchrony may be associated with the strength and duration of thalamic oscillations.

How could the role of hypersynchrony in oscillations be evaluated? There are three major future directions. First, one could analyze multi-unit recordings of thalamic oscillations in further detail. Second, one could apply calcium imaging to acute thalamic slices and directly evaluate inter-neuronal synchrony during both evoked and spontaneous oscillations. Third, one could use the computational TC-heterogeneous thalamic network model to artificially manipulate inter-neuron synchrony and evaluate changes in oscillation measures. I will discuss each of these three approaches in further detail.

As a first pass, multi-unit recordings acquired on the interface rig can be used to assess inter-neuronal synchrony. Although spikes detected in extracellular multi-unit recordings are not assigned to individual neurons, one can assess inter-neuronal synchrony indirectly by evaluating overall spike regularity in the form of an oscillatory index described in Chapter 2. One can also evaluate spike regularity over the course of an oscilla-

tion by computing a running oscillatory index over a sliding time window. If neuronal synchrony indeed plays a role in maintaining oscillations, there would be the following predictions: (1) Across oscillations (spindle-like or paroxysmal), a higher oscillatory index would be expected to correlate with a longer oscillation duration; (2) Within evoked oscillations, the running oscillatory index would be expected to be highest at the beginning of the oscillation decrease towards the end; (3) Before spontaneous oscillations arise, the running oscillatory index would be expected to increase. Note that in Chapter 2 the oscillatory index was defined base on detected spikes, but one could potentially compute the index from an autocorrelation function of the raw trace so that the index would be more independent of the overall number of spikes. Other potential measures of spike regularity, including the variance of inter-spike-intervals and the variance of the number of spikes per burst, may also be used for indirectly assessing inter-neuronal synchrony.

A more direct method to assess inter-neuronal synchrony is to simultaneously monitor thalamic neurons and correlate activity during both evoked oscillations and spontaneous oscillations with calcium imaging. Rats can be injected intracerebroventricularly with a virus expressing GCaMP (a green calcium indicator) under the CAMKII promoter (expressed in excitatory neurons) and a virus expressing RCaMP (a red calcium indicator) under the GAD (expressed in inhibitory neurons) promoter. Importantly, as there may be concern that calcium required for low-threshold spikes during oscillations are chelated by the calcium indicator, oscillations must be verified to be similarly evoked in acute thalamic slices of rats expressing calcium indicators. If successful, the calcium imaging approach would allow the activity of populations of neurons in both the reticular thalamic nucleus and the ventrobasal nucleus to be simultaneously monitored before and during oscillations. Performing experiments at a 5x magnification would allow activity across regions of

the thalamus to be correlated, whereas performing experiments at a 25x magnification would allow more accurate quantification and correlation of activity across single thalamocortical neurons.

How could neuronal activity be correlated? Synchronization could be evaluated among raw dF/F signals. Phase synchronization between each pair of neurons could be quantified with a "mean phase coherence" defined using the Hilbert transform[307]. Synchronization could also be evaluated among rasters of detected spike times. A *spike-field coherence* between each neuron and the population average could be measured over 100 ms time windows by generating a time-frequency coherence spectrogram for each neuron[306,308,309]. The spike-field coherence in the 2-5 Hz frequency band may indicate a propensity for oscillations and would be expected to increase before the onset of spontaneous oscillations, reach the highest value at the beginning of oscillations and gradually decrease over time. Inter-neuronal synchrony may also be measured across several different temporal precisions (5 ms, 10 ms, 25 ms) by the Δ-coarse covariation model[303]. Whereas synchrony as coarser levels (25 ms) might occur at every cycle of an oscillation, synchrony at finer levels (5 ms) may occur in earlier cycles only. Finally, if calcium activity does not provide high enough temporal precision for fine-level synchrony measures, graphene electrodes may be used in combination with imaging[310].

Finally, inter-neuronal synchrony can be manipulated in computational thalamic network models. Using different combinations of thalamocortical model neurons that exhibited less or more variable LTS latencies, one could compare generate model networks with greater or less inter-neuronal synchrony. Oscillation measures could then be compared across networks. Alternatively, parameter sensitivity analysis on the entire population of single thalamocortical neuron models could be applied to identify receptor and

channel parameters that contribute to the LTS latency heterogeneity. The identified parameter could then be measured in the model network over the course of an oscillation or manipulated across different oscillations. If a specific channel parameter were found to modulate both inter-neuronal synchrony and model network oscillations, one could even generate testable predictions in the acute thalamic slice preparations using appropriate pharmacology.

Spatial patterns of thalamic oscillations

In the acute thalamic slice, I have made the following observations of bicuculline-induced paroxysmal oscillations: (1) Oscillations were not present throughout the slice but appeared to be localize around a narrow region in the ventrobasal thalamus and was thus difficult to find; (2) Spike amplitudes were not always consistent across bursts and often exhibit an alternating pattern from cycle to cycle. Furthermore, when slices were perfused with aCSF without bicuculline, spindle-like oscillations were even more difficult to find.

Several questions arise from these observations: (1) How many neurons are activated during a thalamic oscillation? (2) Do the same neurons participate in each cycle of the oscillation, or are their two or more separate groups of neurons that are activated in an alternating or rotating manner? (3) How many of the activated neurons are in phase with the oscillations?

To resolve the extent and spatial pattern of neurons firing together during each cycle of an oscillation, one could use calcium imaging to simultaneously monitor the activity of neuronal ensembles (countable populations of neurons) throughout the course of both spindle-like and seizure-like oscillations. One could also simultaneously record field or multiunit activity extracellularly, so that activity of individual neurons could be

easily correlated with population activity. A similar approach in zebrafish neurons found that neuronal ensembles were more frequent, less numerous and spatially farther apart during a non-seizure hyperactive state, but less frequent, more numerous and spatially more clustered during seizure states[311,312]. Nevertheless, my observations in the thalamic slice would suggest that thalamic oscillations involve neuronal ensembles that are not as numerous but spatially clustered.

Termination of absence seizures

Recall that one unique feature of typical absence seizures is the shortness of duration (< 30 s). If the mechanism behind this early termination of seizures could be understood, new treatments could be devised that would terminate seizures as soon as they develop. Furthermore, if the mechanism for termination can be applied to smaller networks as well, new treatments could be devised to terminate focal paroxysmal activity before it spreads and generalizes. However, only recently have the absence epilepsy field turned its attention to spike-wave discharge termination, and the majority have been correlative studies using EEG or MEG[313–315]. The mechanism underlying SWD termination is yet to be understood.

Before discussing how absence seizures might terminate, I will discuss how normal spindle oscillations are thought to terminate. An early hypothesis is that the progressive hyperpolarization of GABAergic RT/PGN neurons and the consequent decreased response to TC-RT activation may contribute to spindle termination[191]. However, it was found that RT cells are depolarized and may actually progressively depolarize throughout a spindle wave[138,140]. Another hypothesis is that a gradual inhibition of GABA release from RT/PGN neurons through the activation of presynaptic $GABA_B$ receptors terminates spindles. This

has been demonstrated to be possible in the form of paired-burst inhibition[251]. However, there is a lack of histochemical evidence of $GABA_B$ receptors in the ventrobasal thalamus[220], and blocking $GABA_B$ receptors does not affect the generation of spindle waves or the spindle wave refractory period[166,192]. We now turn to hypotheses with more extensive evidence:

Hypothesis I: Persistent activation of the HCN channels of thalamocortical neurons terminates spindles.

In ferret slices, intracellular recordings of TC neurons of the dorsal lateral geniculate nucleus showed that within each spindle wave (or each bout of paroxysmal oscillations if bicuculline is added), the negative-most membrane potential of each cycle became progressively more depolarized[166]. This was followed by a slow afterdepolarization (ADP) during which any evoked rebound LTS from either injecting a hyperpolarizing pulse or stimulating RT neurons have decreased amplitude[166]. The decreased responsiveness was rescued by artificially hyperpolarizing the membrane potential and was exacerbated by artificially depolarizing the membrane potential[166]. Such an ADP was also generated with intracellular injections of repetitive hyperpolarizing current pulses (80-250 ms) at 2-8 Hz and was abolished by applying cesium (an HCN channel blocker) locally with a micropipette[166]. Therefore, the ADP seems to be important for setting the length of the refractory period, and it is result of the activation of HCN channels (I_h)[166]. In fact, when cesium was applied to the bath solution, both the ADP the refractory period disappeared, causing the network to continuously oscillate[166]. Furthermore, computational models could replicate waxing and waning oscillations, generate the slow ADP and spindle wave refractory period by including a slow time constant or calcium dependence for I_h[173].

In summary, the persistent activation of the HCN channels depolarizes the membrane potential and increases the membrane conductance; the former prevents the de-inactivation of T channels and the latter decreases the amplitude of RT-TC IPSPs, further depolarizing the membrane potential and preventing the de-inactivation of T channels, precluding future rebound bursts from occurring and resulting in the termination of the oscillation.

Hypothesis II: Altered corticothalamic feedback terminate spindles.

In anaesthetized cats with the left cortex removed, field recordings in the thalamus showed a lack of spatial coherence in 80% of the spindles observed[243]. Therefore, corticothalamic projections are not only significant in the cortical focus theory of SWD generation, but may also play a role in the synchronization of thalamocortical oscillations, and a decrease in corticothalamic feedback might allow spindles to terminate.

On the other hand, also in anaesthetized cats, *in vivo* field and extracellular recordings in the motor cortex showed that there is an increase in cortical firing right before spindle termination[316]. Simultaneous intracellular recordings in the motor cortex and thalamus showed that whereas in the early phases of a spindle wave cortical firing was driven by thalamic rebound bursts, in late phases cortical firing was no longer in phase with thalamic IPSPs, the overall hyperpolarization level of TC neurons was reduced and TC neurons rarely fired rebound bursts[316]. A computational model was also established that reproduced waxing-and-waning spindle-like oscillations[316]. During the waning phase, cortical activity fell out of step with thalamic activity[316]. This desynchronization between the cortex and the thalamus caused the corticothalamic feedback to steadily depolarize TC neurons, preventing the de-inactivation of T type calcium channels and eventually led to the termination of the oscillation[316].

In summary, a sudden increase or decrease in corticothalamic feedback might increase desynchronization between the cortex and the thalamus and lead to the termination of spindles.

Hypothesis III: Enhanced intra-RT GABAergic inhibition terminate spindles.

In barbiturate-anesthetized cats, local injection of bicuculline (a $GABA_A$ receptor antagonist) in rostral RT decreased the frequency of spindles to 4 Hz and increased the synchrony of firing across RT and TC neurons, indicating the importance of intra-RT $GABA_A$ inhibition in desynchronization[82]. In mice, the duration of electrical stimulation-induced spindle-like oscillations were reversibly shortened after clonazepam (an allosteric $GABA_A$ receptor agonist) treatment[196]. This effect was also found in mice with a benzodiazepine mutation the α_1 subunit of the $GABA_A$ receptor (those in TC neurons), but not in mice with a benzodiazepine mutation the α_3 subunit of the $GABA_A$ receptor (those in RT neurons), showing that clonazepam shortened spindles through enhancing intra-RT inhibition[196]. Extracellular recordings of RT neurons showed that the spikes that occur at the peak of each oscillation cycle (the synchronous spikes) were preferentially suppressed and that the suppression of spikes grew over the course of the oscillation[196]. Intracellular recordings showed that clonazepam treatment did not affect the number of spikes per burst, but decreased the number of bursts overall[196]. Therefore, enhanced intra-RT inhibition seems to terminate oscillations through desynchronization. RT neurons across the network would receive varying levels of inhibition at different times, causing the neurons to fire with unequal delays, or to fail to fire entirely, on the next oscillation cycle. In fact, the $GABA_A$-mediated IPSPs on RT neurons can be relatively long lasting (200 ms)[317], adding to the resulting temporal offset between connected RT neurons.

In support for a role of RT neurons in spindle termination, simultaneous multi-unit

recordings of topographically-coupled TC and RT neurons in freely sleeping rats found a steady decrease of spikes per burst in RT neurons, but not in TC neurons, over the course of a spindle oscillation[318]. There is also a sudden drop in RT activity right before the termination of an oscillation. Interestingly, the probability for an RT neuron to burst in the first spindle cycle negatively correlated with the oscillation duration[318]. However, optogenetic stimulation of RT neurons at different intensities had no effect on oscillation duration, so the significance of the correlation is yet to be determined[318].

In summary, enhanced intra-RT inhibition may shorten the duration of thalamic oscillations by desynchronizing RT activity, reducing inhibitory output to TC neurons, attenuating the rebound bursts in TC neurons and recruiting less RT on the next cycle, gradually preventing future bursts from occurring[196].

Finally, we turn to absence seizures. Which structures are important for the termination of seizures? Granger causality analysis on field recordings of WAG/Rij rats showed that during SWDs, there is a complete reversal of cortex-to-thalamus coupling strength after the termination of SWDs, but the thalamus-to-cortex coupling strength remains elevated for at least another 5 seconds[91]. This seems to suggest that a reduced influence of the cortex on the thalamus could terminate SWDs. In a follow-up study, there is a sudden decrease in layer 4 cortex-to-rostral RT coupling 1.5 seconds prior to SWD offset, and an increase in caudal RT to rostral RT coupling 1 second prior to SWD offset[313]. The authors suggested that SWD termination involves both corticothalamic as well as intrathalamic processes, that the rostral RT maintains SWDs and that inhibition from caudal RT to rostral RT breaks the oscillations[313].

Nevertheless, further studies are warranted to dissect the mechanism for SWD

termination. Since SWDs utilize similar circuitry as spindle oscillations, the three hypotheses for spindle termination presented above may apply to SWDs as well. In the latter two hypotheses, desynchronization appear to be a common theme. Since SWDs are highly synchronized neural activity generalized throughout the thalamocortical network, the termination of SWDs likely involve network desynchronization[117]. In addition to the contribution of altered corticothalamic feedback and enhanced intra-RT GABAergic inhibition discussed above, another major source of network desynchronization is the increase in heterogeneity in the timing and probability of rebound LTSs in TC neurons.

How could an increase in rebound LTS heterogeneity or jitter in TC neurons limit thalamic network synchrony and lead to the termination of an oscillation? Since TC-RT excitation is convergent, each RT neuron are excited by many distinct TC neurons. If there were an increase in rebound LTS heterogeneity, RT neurons would receive TC-RT EPSCs at different times and prevent temporal summation, which would decrease the magnitude of RT bursting and subsequently decrease the amplitude of RT-TC IPSCs. Since TC-RT excitation is not divergent, distinct RT neurons would receive excitation from distinct TC neurons. An increase in rebound LTS heterogeneity would cause distinct RT neurons to receive TC-RT excitation at different times and prevent synchronization *across* RT neurons. The convergence and non-divergence of TC-RT connections, together with the variability in the rebound LTS timing of TC neurons, would result in a reduction and desynchronization of RT-TC IPSCs. Since RT-TC connections are convergent, desynchronization would lead to a loss of temporal summation of the already reduced RT-TC IPSCs, causing the summed IPSC to be prolonged. A shift to slower inhibition kinetics, as demonstrated in this study, would lead to a failure in creating T channel open probability discrepancy, reducing the likelihood of generating the next rebound burst. Furthermore, if a later-arriving IPSP suppressed the

post-inhibitory rebound burst evoked by an earlier-arriving IPSP, as shown to be possible in rat thalamic slices[215], TC activity would then be suppressed, preventing the next cycle of oscillation from occurring.

How, then, could such an increase in rebound LTS heterogeneity or jitter in TC neurons be achieved? In thalamic slices of *α3(H126R)* mice, which have a benzodiazepine-insensitive mutation at $GABA_A$ receptors on RT neurons, application of zolpidem (a $GABA_A$ agonist that will now preferentially activate $GABA_A$ receptors on TC neurons) decreased the latency and increased the probability of a rebound LTS (which reduced the period of oscillations) and, more interestingly, increased the phase difference among rebound LTSs recorded in TC neurons[293]. Note that zolpidem increased both the amplitude and duration of RT-TC $GABA_A$R-mediated IPSPs. Using dynamic clamp to modify the train of $GABA_A$-IPSPs a TC neuron experiences during oscillations, an increase in either the amplitude or the duration of $GABA_A$-IPSPs increased rebound LTS probability, decreased rebound LTS latency and modestly increased rebound LTS heterogeneity[293]. On the other hand, an increase in tonic inhibitory current (which hyperpolarizes the resting membrane potential) decreased rebound LTS probability, increased rebound LTS latency and greatly increased rebound LTS heterogeneity[293]. Therefore, it is likely that a prolonged hyperpolarization increases rebound LTS heterogeneity or jitter in TC neurons. An alternative mechanism for LTS heterogeneity is synaptic influence from other areas of the brain. For instance, stimulation of the cerebellar nuclei, which projects to the sensory thalamus, has been demonstrated to terminate SWDs abruptly[319].

In summary, changing the thalamic network architecture, the RT-TC IPSP profile and intrinsic current properties are all possible mechanisms that contribute to SWD termination through increased rebound LTS heterogeneity or jitter in TC neurons. Future

studies could utilize the population of model TC neurons and the heterogenous model thalamic network developed by this work to resolve the mechanisms of SWD termination.

References

1. What Is Epilepsy? | Epilepsy Foundation. http://www.epilepsy.com/learn/epilepsy-101/what-epilepsy.
2. A Revised Definition of Epilepsy. *Epilepsy Foundation* http://www.epilepsy.com/article/2014/4/revised-definition-epilepsy.
3. Who Gets Epilepsy? *Epilepsy Foundation* https://www.epilepsy.com/learn/about-epilepsy-basics/who-gets-epilepsy.
4. Zack, M. M. National and State Estimates of the Numbers of Adults and Children with Active Epilepsy — United States, 2015. *MMWR Morb. Mortal. Wkly. Rep.* **66**, (2017).
5. Forsgren, L. *et al.* Mortality of Epilepsy in Developed Countries: A Review. *Epilepsia* **46**, 18–27 (2005).
6. New Terms for Seizure Classification | Epilepsy Foundation. http://www.epilepsy.com/learn/types-seizures/new-terms-seizure-classification.
7. Fisher, R. S. *et al.* Operational classification of seizure types by the International League Against Epilepsy: Position Paper of the ILAE Commission for Classification and Terminology. *Epilepsia* **58**, 522–530 (2017).

8. Types of Epilepsy Syndromes. *Epilepsy Foundation* http://www.epilepsy.com/learn/types-epilepsy-syndromes.

9. What Causes Epilepsy and Seizures? *Epilepsy Foundation* http://www.epilepsy.com/learn/epilepsy-101/what-causes-epilepsy-and-seizures.

10. Panayiotopoulos, C. P. Typical absence seizures and related epileptic syndromes: Assessment of current state and directions for future research. *Epilepsia* **49**, 2131–2139 (2008).

11. Atypical Absence Seizures | Epilepsy Foundation. http://www.epilepsy.com/learn/types-seizures/atypical-absence-seizures.

12. Absence Epilepsies - Loiseau - 1995 - Epilepsia - Wiley Online Library. http://onlinelibrary.wiley.com/doi/10.1111/j.1528-1157.1995.tb01060.x/abstract.

13. Childhood Absence Epilepsy. *Epilepsy Foundation* http://www.epilepsy.com/learn/types-epilepsy-syndromes/childhood-absence-epilepsy.

14. Juvenile Absence Epilepsy. *Epilepsy Foundation* http://www.epilepsy.com/learn/types-epilepsy-syndromes/juvenile-absence-epilepsy.

15. Wirrell, E. C., Camfield, C. S., Camfield, P. R., Gordon, K. E. & Dooley, J. M. Long-term prognosis of typical childhood absence epilepsy: remission or progression to juvenile myoclonic epilepsy. *Neurology* **47**, 912–918 (1996).

16. Grosso, S. *et al.* Childhood Absence Epilepsy: Evolution and Prognostic Factors. *Epilepsia* **46**, 1796–1801 (2005).

17. Callenbach, P. M. C. *et al.* Long-term outcome of childhood absence epilepsy: Dutch Study of Epilepsy in Childhood. *Epilepsy Res.* **83**, 249–256 (2009).

18. Matricardi, S., Verrotti, A., Chiarelli, F., Cerminara, C. & Curatolo, P. Current Advances in Childhood Absence Epilepsy. *Pediatr. Neurol.* **50**, 205–212 (2014).

19. Tenney, J. R. & Glauser, T. A. The Current State of Absence Epilepsy: Can We Have Your Attention? *Epilepsy Curr.* **13**, 135–140 (2013).

20. Kostyuk, P. G., Molokanova, E. A., Pronchuk, N. F., Savchenko, A. N. & Verkhratsky, A. N. Different action of ethosuximide on low- and high-threshold calcium currents in rat sensory neurons. *Neuroscience* **51**, 755–758 (1992).

21. Leresche, N. *et al.* On the Action of the Anti-Absence Drug Ethosuximide in the Rat and Cat Thalamus. *J. Neurosci.* **18**, 4842–4853 (1998).

22. Glauser, T. A. *et al.* Ethosuximide, Valproic Acid, and Lamotrigine in Childhood Absence Epilepsy. *N. Engl. J. Med.* **362**, 790–799 (2010).

23. Glauser, T. A. *et al.* Ethosuximide, valproic acid, and lamotrigine in childhood absence epilepsy: Initial monotherapy outcomes at 12 months. *Epilepsia* **54**, 141–155 (2013).

24. Cnaan, A. *et al.* Second monotherapy in childhood absence epilepsy. *Neurology* **88**, 182–190 (2017).

25. Kessler, S. K. & McGinnis, E. A Practical Guide to Treatment of Childhood Absence Epilepsy. *Pediatr. Drugs* **21**, 15–24 (2019).

26. Tamura, N. My epilepsy story: What is it like to be absent?—A message from an "ex"-patient. *Epilepsia* **56**, 1707–1709 (2015).

27. Masur, D. *et al.* Pretreatment cognitive deficits and treatment effects on attention in childhood absence epilepsy. *Neurology* **81**, 1572–1580 (2013).

28. Caplan, R. *et al.* Childhood absence epilepsy: Behavioral, cognitive, and linguistic comorbidities. *Epilepsia* **49**, 1838–1846 (2008).

29. Wirrell, E. C. *et al.* Long-term Psychosocial Outcome in Typical Absence Epilepsy: Sometimes a Wolf in Sheeps' Clothing. *Arch. Pediatr. Adolesc. Med.* **151**, 152–158 (1997).

30. Lennox, W. G. The heredity of epilepsy as told by relative and twins. *J. Am. Med. Assoc.* **146**, 529–536 (1951).

31. Wallace, R. H. *et al.* Mutant GABAA receptor γ2-subunit in childhood absence epilepsy and febrile seizures. *Nat. Genet.* **28**, 49–52 (2001).

32. Kananura, C. *et al.* A Splice-Site Mutation in GABRG2 Associated With Childhood

Absence Epilepsy and Febrile Convulsions. *Arch. Neurol.* **59**, 1137–1141 (2002).

33. Maljevic, S. *et al.* A mutation in the GABAA receptor α1-subunit is associated with absence epilepsy. *Ann. Neurol.* **59**, 983–987 (2006).

34. Urak, L., Feucht, M., Fathi, N., Hornik, K. & Fuchs, K. A GABRB3 promoter haplotype associated with childhood absence epilepsy impairs transcriptional activity. *Hum. Mol. Genet.* **15**, 2533–2541 (2006).

35. Feucht, M. *et al.* Possible association between childhood absence epilepsy and the gene encoding GABRB3. *Biol. Psychiatry* **46**, 997–1002 (1999).

36. Lü, J. *et al.* Case-control study and transmission/disequilibrium tests of the genes encoding GABRA5 and GABRB3 in a Chinese population affected by childhood absence epilepsy. *Chin. Med. J. (Engl.)* **117**, 1497–1501 (2004).

37. Tanaka, M. *et al.* Hyperglycosylation and Reduced GABA Currents of Mutated GABRB3 Polypeptide in Remitting Childhood Absence Epilepsy. *Am. J. Hum. Genet.* **82**, 1249–1261 (2008).

38. Jouvenceau, A. *et al.* Human epilepsy associated with dysfunction of the brain P/Q-type calcium channel. *The Lancet* **358**, 801–807 (2001).

39. Imbrici, P. *et al.* Dysfunction of the brain calcium channel CaV2.1 in absence epilepsy and episodic ataxia. *Brain* **127**, 2682–2692 (2004).

40. Singh, B. *et al.* Mutational analysis of CACNA1G in idiopathic generalized epilepsy. *Hum. Mutat.* **28**, 524–525 (2007).

41. Chen, Y. *et al.* Association between genetic variation of CACNA1H and childhood absence epilepsy. *Ann. Neurol.* **54**, 239–243 (2003).

42. Liang, J. *et al.* New variants in the CACNA1H gene identified in childhood absence epilepsy. *Neurosci. Lett.* **406**, 27–32 (2006).

43. Liang, J. *et al.* Common Polymorphisms in the CACNA1H Gene Associated with Childhood Absence Epilepsy in Chinese Han Population. *Ann. Hum. Genet.* **71**, 325–335 (2007).

44. Everett, K. V. *et al.* Linkage and association analysis of CACNG3 in childhood absence epilepsy. *Eur. J. Hum. Genet.* **15**, 463–472 (2007).

45. Everett, K. *et al.* Linkage and mutational analysis of CLCN2 in childhood absence epilepsy. *Epilepsy Res.* **75**, 145–153 (2007).

46. Moore, T. *et al.* Polymorphism analysis of JRK/JH8, the human homologue of mouse jerky, and description of a rare mutation in a case of CAE evolving to JME. *Epilepsy Res.* **46**, 157–167 (2001).

47. Gu, W., Sander, T., Becker, T. & Steinlein, O. K. Genotypic association of exonic LGI4 polymorphisms and childhood absence epilepsy. *Neurogenetics* **5**, 41–44 (2004).

48. Suls, A. *et al.* Early-onset absence epilepsy caused by mutations in the glucose transporter GLUT1. *Ann. Neurol.* **66**, 415–419 (2009).

49. Mullen, S. A., Suls, A., Jonghe, P. D., Berkovic, S. F. & Scheffer, I. E. Absence epilepsies with widely variable onset are a key feature of familial GLUT1 deficiency. *Neurology* **75**, 432–440 (2010).

50. Yalçin, Ö. *et al.* An association analysis at 2q36 reveals a new candidate susceptibility gene for juvenile absence epilepsy and/or absence seizures associated with generalized tonic–clonic seizures. *Epilepsia* **52**, 975–983 (2011).

51. Yalçın, Ö. Genes and molecular mechanisms involved in the epileptogenesis of idiopathic absence epilepsies. *Seizure* **21**, 79–86 (2012).

52. Glauser, T. A. *et al.* Pharmacogenetics of antiepileptic drug efficacy in childhood absence epilepsy. *Ann. Neurol.* **81**, 444–453 (2017).

53. Venzi, M., Di Giovanni, G. & Crunelli, V. A Critical Evaluation of the Gamma-Hydroxybutyrate (GHB) Model of Absence Seizures. *CNS Neurosci. Ther.* **21**, 123–140 (2015).

54. Snead, O. C. The gamma-hydroxybutyrate model of absence seizures: correlation of regional brain levels of gamma-hydroxybutyric acid and gamma-butyrolactone with spike wave discharges. *Neuropharmacology* **30**, 161–167 (1991).

55. Kliouеva, I. A., van Luijtelaar, E. L. J. M., Chepurnova, N. E. & Chepurnov, S. A. PTZ-

induced seizures in rats: effects of age and strain. *Physiol. Behav.* **72**, 421–426 (2001).

56. Noebels, J. L. & Sidman, R. L. Inherited epilepsy: spike-wave and focal motor seizures in the mutant mouse tottering. *Science* **204**, 1334–1336 (1979).

57. Fletcher, C. F. *et al.* Absence Epilepsy in Tottering Mutant Mice Is Associated with Calcium Channel Defects. *Cell* **87**, 607–617 (1996).

58. Barclay, J. *et al.* Ducky Mouse Phenotype of Epilepsy and Ataxia Is Associated with Mutations in the Cacna2d2 Gene and Decreased Calcium Channel Current in Cerebellar Purkinje Cells. *J. Neurosci.* **21**, 6095–6104 (2001).

59. Hosford, D. A. *et al.* The role of GABAB receptor activation in absence seizures of lethargic (lh/lh) mice. *Science* **257**, 398–401 (1992).

60. Letts, V. A. *et al.* The mouse stargazer gene encodes a neuronal Ca2+-channel γ subunit. *Nat. Genet.* **19**, 340–347 (1998).

61. Ernst, W. L., Zhang, Y., Yoo, J. W., Ernst, S. J. & Noebels, J. L. Genetic Enhancement of Thalamocortical Network Activity by Elevating α1G-Mediated Low-Voltage-Activated Calcium Current Induces Pure Absence Epilepsy. *J. Neurosci.* **29**, 1615–1625 (2009).

62. Heuermann, R. J. *et al.* Reduction of thalamic and cortical Ih by deletion of TRIP8b produces a mouse model of human absence epilepsy. *Neurobiol. Dis.* **85**, 81–92 (2016).

63. DeLorey, T. M. *et al.* Mice Lacking the β3 Subunit of the GABAA Receptor Have the Epilepsy Phenotype and Many of the Behavioral Characteristics of Angelman Syndrome. *J. Neurosci.* **18**, 8505–8514 (1998).

64. Tan, H. O. *et al.* Reduced cortical inhibition in a mouse model of familial childhood absence epilepsy. *Proc. Natl. Acad. Sci.* **104**, 17536–17541 (2007).

65. Pearl, P. L., Shukla, L., Theodore, W. H., Jakobs, C. & Michael Gibson, K. Epilepsy in succinic semialdehyde dehydrogenase deficiency, a disorder of GABA metabolism. *Brain Dev.* **33**, 796–805 (2011).

66. Cope, D. W. *et al.* Enhanced tonic GABAA inhibition in typical absence epilepsy. *Nat. Med.* **15**, 1392–1398 (2009).

67. Yu, Z. *et al.* GABA Transporter-1 Deficiency Confers Schizophrenia-Like Behavioral Phenotypes. *PLOS ONE* **8**, e69883 (2013).

68. Beyer, B. *et al.* Absence seizures in C3H/HeJ and knockout mice caused by mutation of the AMPA receptor subunit Gria4. *Hum. Mol. Genet.* **17**, 1738–1749 (2008).

69. Kim, D. *et al.* Lack of the Burst Firing of Thalamocortical Relay Neurons and Resistance to Absence Seizures in Mice Lacking α1G T-Type Ca2+ Channels. *Neuron* **31**, 35–45 (2001).

70. Astori, S. *et al.* The CaV3.3 calcium channel is the major sleep spindle pacemaker in

thalamus. *Proc. Natl. Acad. Sci.* **108**, 13823–13828 (2011).

71. Schofield, C. M., Kleiman-Weiner, M., Rudolph, U. & Huguenard, J. R. A gain in GABAA receptor synaptic strength in thalamus reduces oscillatory activity and absence seizures. *Proc. Natl. Acad. Sci.* **106**, 7630–7635 (2009).

72. Coenen, A. M. L. & Luijtelaar, E. L. J. M. van. Genetic Animal Models for Absence Epilepsy: A Review of the WAG/Rij Strain of Rats. *Behav. Genet.* **33**, 635–655 (2003).

73. Drinkenburg, W. H. I. M., Coenen, A. M. L., Vossen, J. M. H. & Van Luijtelaar, E. L. J. M. Spike-wave discharges and sleep-wake states in rats with absence epilepsy. *Epilepsy Res.* **9**, 218–224 (1991).

74. Danober, L., Deransart, C., Depaulis, A., Vergnes, M. & Marescaux, C. Pathophysiological mechanisms of genetic absence epilepsy in the rat. *Prog. Neurobiol.* **55**, 27–57 (1998).

75. Berman, R. *et al.* Simultaneous EEG, fMRI, and behavior in typical childhood absence seizures. *Epilepsia* **51**, 2011–2022 (2010).

76. Moeller, F. *et al.* Functional connectivity in patients with idiopathic generalized epilepsy. *Epilepsia* **52**, 515–522 (2011).

77. Nersesyan, H., Hyder, F., Rothman, D. L. & Blumenfeld, H. Dynamic fMRI and EEG Recordings during Spike-Wave Seizures and Generalized Tonic-Clonic Seizures in

WAG/Rij Rats. *J. Cereb. Blood Flow Metab.* **24**, 589–599 (2004).

78. Chipaux, M., Vercueil, L., Kaminska, A., Mahon, S. & Charpier, S. Persistence of Cortical Sensory Processing during Absence Seizures in Human and an Animal Model: Evidence from EEG and Intracellular Recordings. *PLOS ONE* **8**, e58180 (2013).

79. Vergnes, M. & Marescaux, C. Cortical and thalamic lesions in rats with genetic absence epilepsy. *J. Neural Transm. Suppl.* **35**, 71–83 (1992).

80. Williams, D. A study of thalamic and cortical rhythms in petit mal. *Brain J. Neurol.* **76**, 50–69 (1953).

81. Vergnes, M., Marescaux, C., Depaulis, A., Micheletti, G. & Warter, J. M. Spontaneous spike and wave discharges in thalamus and cortex in a rat model of genetic petit mal-like seizures. *Exp. Neurol.* **96**, 127–136 (1987).

82. Steriade, M. & Contreras, D. Spike-Wave Complexes and Fast Components of Cortically Generated Seizures. I. Role of Neocortex and Thalamus. *J. Neurophysiol.* **80**, 1439–1455 (1998).

83. Meeren, H. K. M., Pijn, J. P. M., Luijtelaar, E. L. J. M. V., Coenen, A. M. L. & Silva, F. H. L. da. Cortical Focus Drives Widespread Corticothalamic Networks during Spontaneous Absence Seizures in Rats. *J. Neurosci.* **22**, 1480–1495 (2002).

84. Polack, P.-O. *et al.* Deep Layer Somatosensory Cortical Neurons Initiate Spike-and-

Wave Discharges in a Genetic Model of Absence Seizures. *J. Neurosci.* **27**, 6590–6599 (2007).

85. Manning, J.-P. A., Richards, D. A., Leresche, N., Crunelli, V. & Bowery, N. G. Cortical-area specific block of genetically determined absence seizures by ethosuximide. *Neuroscience* **123**, 5–9 (2004).

86. Polack, P.-O., Mahon, S., Chavez, M. & Charpier, S. Inactivation of the Somatosensory Cortex Prevents Paroxysmal Oscillations in Cortical and Related Thalamic Neurons in a Genetic Model of Absence Epilepsy. *Cereb. Cortex* **19**, 2078–2091 (2009).

87. Tenney, J. R. *et al.* Focal corticothalamic sources during generalized absence seizures: A MEG study. *Epilepsy Res.* **106**, 113–122 (2013).

88. Avanzini, G., Vergnes, M., Spreafico, R. & Marescaux, C. Calcium-Dependent Regulation of Genetically Determined Spike and Waves by the Reticular Thalamic Nucleus of Rats. *Epilepsia* **34**, 1–7 (1993).

89. Banerjee, P. K. & Snead, O. C. Thalamic mediodorsal and intralaminar nuclear lesions disrupt the generation of experimentally induced generalized absence-like seizures in rats. *Epilepsy Res.* **17**, 193–205 (1994).

90. Meeren, H. K. M., Veening, J. G., Möderscheim, T. A. E., Coenen, A. M. L. & van Luijtelaar, G. Thalamic lesions in a genetic rat model of absence epilepsy: Dissociation

between spike-wave discharges and sleep spindles. *Exp. Neurol.* **217**, 25–37 (2009).

91. Sitnikova, E., Dikanev, T., Smirnov, D., Bezruchko, B. & van Luijtelaar, G. Granger causality: Cortico-thalamic interdependencies during absence seizures in WAG/Rij rats. *J. Neurosci. Methods* **170**, 245–254 (2008).

92. Inoue, M., Duysens, J., Vossen, J. M. H. & Coenen, A. M. L. Thalamic multiple-unit activity underlying spike-wave discharges in anesthetized rats. *Brain Res.* **612**, 35–40 (1993).

93. Seidenbecher, T., Staak, R. & Pape, H.-C. Relations between cortical and thalamic cellular activities during absence seizures in rats. *Eur. J. Neurosci.* **10**, 1103–1112 (1998).

94. Beenhakker, M. P. & Huguenard, J. R. Neurons that Fire Together Also Conspire Together: Is Normal Sleep Circuitry Hijacked to Generate Epilepsy? *Neuron* **62**, 612–632 (2009).

95. Sherman, S. M. The thalamus is more than just a relay. *Curr. Opin. Neurobiol.* **17**, 417–422 (2007).

96. Peters, A. & Feldman, M. L. The projection of the lateral geniculate nucleus to area 17 of the rat cerebral cortex, IV terminations upon spiny dendrites. *J. Neurocytol.* **6**, 669–689 (1977).

97. Hooks, B. M. *et al.* Organization of Cortical and Thalamic Input to Pyramidal Neurons in Mouse Motor Cortex. *J. Neurosci.* **33**, 748–760 (2013).

98. Dufour, A. *et al.* Area Specificity and Topography of Thalamocortical Projections Are Controlled by ephrin/Eph Genes. *Neuron* **39**, 453–465 (2003).

99. Chmielowska, J., Carvell, G. E. & Simons, D. J. Spatial organization of thalamocortical and corticothalamic projection systems in the rat SmI barrel cortex. *J. Comp. Neurol.* **285**, 325–338 (1989).

100. Steriade, M. The GABAergic reticular nucleus: A preferential target of corticothalamic projections. *Proc. Natl. Acad. Sci.* **98**, 3625–3627 (2001).

101. Liu, X.-B., Honda, C. n. & Jones, E. g. Distribution of four types of synapse on physiologically identified relay neurons in the ventral posterior thalamic nucleus of the cat. *J. Comp. Neurol.* **352**, 69–91 (1995).

102. Erişir, A., Van Horn, S. C. & Sherman, S. M. Relative numbers of cortical and brainstem inputs to the lateral geniculate nucleus. *Proc. Natl. Acad. Sci.* **94**, 1517–1520 (1997).

103. Van Horn, S. C., Erişir, A. & Sherman, S. M. Relative distribution of synapses in the A-laminae of the lateral geniculate nucleus of the cat. *J. Comp. Neurol.* **416**, 509–520 (2000).

104. Liu, X.-B. & Jones, E. G. Predominance of corticothalamic synaptic inputs to thalamic reticular nucleus neurons in the rat. *J. Comp. Neurol.* **414**, 67–79 (1999).

105. Sumser, A., Mease, R. A., Sakmann, B. & Groh, A. Organization and somatotopy of corticothalamic projections from L5B in mouse barrel cortex. *Proc. Natl. Acad. Sci.* **114**, 8853–8858 (2017).

106. Deschênes, M., Veinante, P. & Zhang, Z.-W. The organization of corticothalamic projections: reciprocity versus parity. *Brain Res. Rev.* **28**, 286–308 (1998).

107. Mishima, K. Facilitatory and Inhibitory Processes in the Thalamic Ventrobasal Nucleus of the Rat. *Jpn. J. Physiol.* **42**, 193–210 (1992).

108. Ferster, D. & Levy, S. The axonal arborizations of lateral geniculate neurons in the striate cortex of the cat. *J. Comp. Neurol.* **182**, 923–944 (1978).

109. Harris, R. M. Axon collaterals in the thalamic reticular nucleus from thalamocortical neurons of the rat ventrobasal thalamus. *J. Comp. Neurol.* **258**, 397–406 (1987).

110. Kim, U. & McCormick, D. A. The Functional Influence of Burst and Tonic Firing Mode on Synaptic Interactions in the Thalamus. *J. Neurosci.* **18**, 9500–9516 (1998).

111. Ide, L. S. The fine structure of the perigeniculate nucleus in the cat. *J. Comp. Neurol.* **210**, 317–334 (1982).

112. Friedlander, M. J., Lin, C. S., Stanford, L. R. & Sherman, S. M. Morphology of functionally identified neurons in lateral geniculate nucleus of the cat. *J. Neurophysiol.* **46**, 80–129 (1981).

113. Stanford, L. R., Friedlander, M. J. & Sherman, S. M. Morphological and physiological properties of geniculate W-cells of the cat: a comparison with X- and Y-cells. *J. Neurophysiol.* **50**, 582–608 (1983).

114. Pita-Almenar, J. D., Yu, D., Lu, H.-C. & Beierlein, M. Mechanisms Underlying Desynchronization of Cholinergic-Evoked Thalamic Network Activity. *J. Neurosci.* **34**, 14463–14474 (2014).

115. Cox, C. L., Huguenard, J. R. & Prince, D. A. Heterogeneous axonal arborizations of rat thalamic reticular neurons in the ventrobasal nucleus. *J. Comp. Neurol.* **366**, 416–430 (1996).

116. Pinault, D. & Deschênes, M. Projection and innervation patterns of individual thalamic reticular axons in the thalamus of the adult rat: A three-dimensional, graphic, and morphometric analysis. *J. Comp. Neurol.* **391**, 180–203 (1998).

117. Fogerson, P. M. & Huguenard, J. R. Tapping the Brakes: Cellular and Synaptic Mechanisms that Regulate Thalamic Oscillations. *Neuron* **92**, 687–704 (2016).

118. Pinault, D., Bourassa, J. & Deschênes, M. The Axonal Arborization of Single Thalamic

Reticular Neurons in the Somatosensory Thalamus of the Rat. *Eur. J. Neurosci.* **7**, 31–40 (1995).

119. Pinault, D. The thalamic reticular nucleus: structure, function and concept. *Brain Res. Rev.* **46**, 1–31 (2004).

120. Yen, C. T., Conley, M., Hendry, S. H. & Jones, E. G. The morphology of physiologically identified GABAergic neurons in the somatic sensory part of the thalamic reticular nucleus in the cat. *J. Neurosci.* **5**, 2254–2268 (1985).

121. Liu, X.-B., Warren, R. A. & Jones, E. G. Synaptic distribution of afferents from reticular nucleus in ventroposterior nucleus of cat thalamus. *J. Comp. Neurol.* **352**, 187–202 (1995).

122. Ohara, P. T. Synaptic organization of the thalamic reticular nucleus. *J. Electron Microsc. Tech.* **10**, 283–292 (1988).

123. Williamson, A. M., Ohara, P. T., Ralston, D. D., Milroy, A. M. & Ralston, H. J. Analysis of gamma-aminobutyric acidergic synaptic contacts in the thalamic reticular nucleus of the monkey. *J. Comp. Neurol.* **349**, 182–192 (1994).

124. Zhang, L. & Jones, E. G. Corticothalamic Inhibition in the Thalamic Reticular Nucleus. *J. Neurophysiol.* **91**, 759–766 (2004).

125. Sun, Y.-G., Wu, C.-S., Lu, H.-C. & Beierlein, M. Target-Dependent Control of Synaptic

Inhibition by Endocannabinoids in the Thalamus. *J. Neurosci.* **31**, 9222–9230 (2011).

126. Sanchez-Vives, M. V., Bal, T. & McCormick, D. A. Inhibitory Interactions between Perigeniculate GABAergic Neurons. *J. Neurosci.* **17**, 8894–8908 (1997).

127. Shu, Y. & McCormick, D. A. Inhibitory Interactions Between Ferret Thalamic Reticular Neurons. *J. Neurophysiol.* **87**, 2571–2576 (2002).

128. Landisman, C. E. *et al.* Electrical Synapses in the Thalamic Reticular Nucleus. *J. Neurosci.* **22**, 1002–1009 (2002).

129. Parker, P. R. L., Cruikshank, S. J. & Connors, B. W. Stability of Electrical Coupling despite Massive Developmental Changes of Intrinsic Neuronal Physiology. *J. Neurosci.* **29**, 9761–9770 (2009).

130. Cruikshank, S. J., Urabe, H., Nurmikko, A. V. & Connors, B. W. Pathway-Specific Feedforward Circuits between Thalamus and Neocortex Revealed by Selective Optical Stimulation of Axons. *Neuron* **65**, 230–245 (2010).

131. Hou, G., Smith, A. G. & Zhang, Z.-W. Lack of Intrinsic GABAergic Connections in the Thalamic Reticular Nucleus of the Mouse. *J. Neurosci.* **36**, 7246–7252 (2016).

132. Deleuze, C. & Huguenard, J. R. Distinct Electrical and Chemical Connectivity Maps in the Thalamic Reticular Nucleus: Potential Roles in Synchronization and Sensation. *J. Neurosci.* **26**, 8633–8645 (2006).

133. Condorelli, D. F., Belluardo, N., Trovato-Salinaro, A. & Mudò, G. Expression of Cx36 in mammalian neurons. *Brain Res. Rev.* **32**, 72–85 (2000).

134. Zolnik, T. A. & Connors, B. W. Electrical synapses and the development of inhibitory circuits in the thalamus. *J. Physiol.* **594**, 2579–2592 (2016).

135. Lam, Y.-W., Nelson, C. S. & Sherman, S. M. Mapping of the Functional Interconnections Between Thalamic Reticular Neurons Using Photostimulation. *J. Neurophysiol.* **96**, 2593–2600 (2006).

136. Avanzini, G., de Curtis, M., Panzica, F. & Spreafico, R. Intrinsic properties of nucleus reticularis thalami neurones of the rat studied in vitro. *J. Physiol.* **416**, 111–122 (1989).

137. Domich, L., Oakson, G. & Steriade, M. Thalamic burst patterns in the naturally sleeping cat: a comparison between cortically projecting and reticularis neurones. *J. Physiol.* **379**, 429–449 (1986).

138. Steriade, M., Domich, L. & Oakson, G. Reticularis thalami neurons revisited: activity changes during shifts in states of vigilance. *J. Neurosci.* **6**, 68–81 (1986).

139. Bal, T. & McCormick, D. A. Mechanisms of oscillatory activity in guinea-pig nucleus reticularis thalami in vitro: a mammalian pacemaker. *J. Physiol.* **468**, 669–691 (1993).

140. Mulle, C., Madariaga, A. & Deschenes, M. Morphology and electrophysiological

properties of reticularis thalami neurons in cat: in vivo study of a thalamic pacemaker. *J. Neurosci.* **6**, 2134–2145 (1986).

141. Steriade, M., Domich, L., Oakson, G. & Deschenes, M. The deafferented reticular thalamic nucleus generates spindle rhythmicity. *J. Neurophysiol.* **57**, 260–273 (1987).

142. Lee, S.-H., Govindaiah, G. & Cox, C. L. Heterogeneity of firing properties among rat thalamic reticular nucleus neurons. *J. Physiol.* **582**, 195–208 (2007).

143. Huguenard, J. R. & Prince, D. A. A novel T-type current underlies prolonged Ca(2+)-dependent burst firing in GABAergic neurons of rat thalamic reticular nucleus. *J. Neurosci.* **12**, 3804–3817 (1992).

144. Crandall, S. R., Govindaiah, G. & Cox, C. L. Low-Threshold Ca2+ Current Amplifies Distal Dendritic Signaling in Thalamic Reticular Neurons. *J. Neurosci.* **30**, 15419–15429 (2010).

145. Talley, E. M. *et al.* Differential Distribution of Three Members of a Gene Family Encoding Low Voltage-Activated (T-Type) Calcium Channels. *J. Neurosci.* **19**, 1895–1911 (1999).

146. Klöckner, U. *et al.* Comparison of the Ca2+ currents induced by expression of three cloned α1 subunits, α1G, α1H and α1I, of low-voltage-activated T-type Ca2+ channels. *Eur. J. Neurosci.* **11**, 4171–4178 (1999).

147. Joksovic, P. M., Bayliss, D. A. & Todorovic, S. M. Different kinetic properties of two T-type Ca2+ currents of rat reticular thalamic neurones and their modulation by enflurane. *J. Physiol.* **566**, 125–142 (2005).

148. Tsakiridou, E., Bertollini, L., Curtis, M. de, Avanzini, G. & Pape, H. C. Selective increase in T-type calcium conductance of reticular thalamic neurons in a rat model of absence epilepsy. *J. Neurosci.* **15**, 3110–3117 (1995).

149. Broicher, T., Kanyshkova, T., Meuth, P., Pape, H.-C. & Budde, T. Correlation of T-channel coding gene expression, IT, and the low threshold Ca2+ spike in the thalamus of a rat model of absence epilepsy. *Mol. Cell. Neurosci.* **39**, 384–399 (2008).

150. Talley, E. M., Solórzano, G., Depaulis, A., Perez-Reyes, E. & Bayliss, D. A. Low-voltage-activated calcium channel subunit expression in a genetic model of absence epilepsy in the rat. *Mol. Brain Res.* **75**, 159–165 (2000).

151. Tringham, E. *et al.* T-Type Calcium Channel Blockers That Attenuate Thalamic Burst Firing and Suppress Absence Seizures. *Sci. Transl. Med.* **4**, 121ra19-121ra19 (2012).

152. Stocker, M. Ca2+-activated K+ channels: molecular determinants and function of the SK family. *Nat. Rev. Neurosci.* **5**, 758–770 (2004).

153. Schumacher, M. A., Rivard, A. F., Bächinger, H. P. & Adelman, J. P. Structure of the

gating domain of a Ca2+-activated K+ channel complexed with Ca2+/calmodulin. *Nature* **410**, 1120–1124 (2001).

154. Hotson, J. R. & Prince, D. A. A calcium-activated hyperpolarization follows repetitive firing in hippocampal neurons. *J. Neurophysiol.* **43**, 409–419 (1980).

155. Alger, B. E. & Nicoll, R. A. Epileptiform burst afterhyperolarization: calcium-dependent potassium potential in hippocampal CA1 pyramidal cells. *Science* **210**, 1122–1124 (1980).

156. Sailer, C. A. *et al.* Regional Differences in Distribution and Functional Expression of Small-Conductance Ca2+-Activated K+ Channels in Rat Brain. *J. Neurosci.* **22**, 9698–9707 (2002).

157. Debarbieux, F., Brunton, J. & Charpak, S. Effect of Bicuculline on Thalamic Activity: A Direct Blockade of I AHP in Reticularis Neurons. *J. Neurophysiol.* **79**, 2911–2918 (1998).

158. Kleiman-Weiner, M., Beenhakker, M. P., Segal, W. A. & Huguenard, J. R. Synergistic Roles of GABAA Receptors and SK Channels in Regulating Thalamocortical Oscillations. *J. Neurophysiol.* **102**, 203–213 (2009).

159. Llinás, R. & Jahnsen, H. Electrophysiology of mammalian thalamic neurones in vitro. *Nature* **297**, 406–408 (1982).

160. McCarley, R. W., Benoit, O. & Barrionuevo, G. Lateral geniculate nucleus unitary discharge in sleep and waking: state- and rate-specific aspects. *J. Neurophysiol.* **50**, 798–818 (1983).

161. Leresche, N., Lightowler, S., Soltesz, I., Jassik-Gerschenfeld, D. & Crunelli, V. Low-frequency oscillatory activities intrinsic to rat and cat thalamocortical cells. *J. Physiol.* **441**, 155–174 (1991).

162. McCormick, D. A. & Pape, H. C. Properties of a hyperpolarization-activated cation current and its role in rhythmic oscillation in thalamic relay neurones. *J. Physiol.* **431**, 291–318 (1990).

163. Porcello, D. M., Smith, S. D. & Huguenard, J. R. Actions of U-92032, a T-Type Ca2+ Channel Antagonist, Support a Functional Linkage Between I T and Slow Intrathalamic Rhythms. *J. Neurophysiol.* **89**, 177–185 (2003).

164. Soltesz, I. *et al.* Two inward currents and the transformation of low-frequency oscillations of rat and cat thalamocortical cells. *J. Physiol.* **441**, 175–197 (1991).

165. Chapin, E. M. & Andrade, R. Calcium-Independent Afterdepolarization Regulated by Serotonin in Anterior Thalamus. *J. Neurophysiol.* **83**, 3173–3176 (2000).

166. Bal, T. & McCormick, D. A. What Stops Synchronized Thalamocortical Oscillations? *Neuron* **17**, 297–308 (1996).

167. DiFrancesco, D. & Tortora, P. Direct activation of cardiac pacemaker channels by intracellular cyclic AMP. *Nature* **351**, 145–147 (1991).

168. Ingram, S. L. & Williams, J. T. Modulation of the hyperpolarization-activated current (Ih) by cyclic nucleotides in guinea-pig primary afferent neurons. *J. Physiol.* **492**, 97–106 (1996).

169. Santoro, B. *et al.* Molecular and Functional Heterogeneity of Hyperpolarization-Activated Pacemaker Channels in the Mouse CNS. *J. Neurosci.* **20**, 5264–5275 (2000).

170. Munsch, T. & Pape, H.-C. Modulation of the hyperpolarization-activated cation current of rat thalamic relay neurones by intracellular pH. *J. Physiol.* **519**, 493–504 (1999).

171. McCormick, D. A. & Pape, H. C. Noradrenergic and serotonergic modulation of a hyperpolarization-activated cation current in thalamic relay neurones. *J. Physiol.* **431**, 319–342 (1990).

172. Monckton, J. E. & McCormick, D. A. Neuromodulatory Role of Serotonin in the Ferret Thalamus. *J. Neurophysiol.* **87**, 2124–2136 (2002).

173. Destexhe, A., Bal, T., McCormick, D. A. & Sejnowski, T. J. Ionic mechanisms underlying synchronized oscillations and propagating waves in a model of ferret thalamic slices. *J. Neurophysiol.* **76**, 2049–2070 (1996).

174. Kao, C.-Q. & Coulter, D. A. Physiology and Pharmacology of Corticothalamic Stimulation-Evoked Responses in Rat Somatosensory Thalamic Neurons In Vitro. *J. Neurophysiol.* **77**, 2661–2676 (1997).

175. Golshani, P., Liu, X.-B. & Jones, E. G. Differences in quantal amplitude reflect GluR4-subunit number at corticothalamic synapses on two populations of thalamic neurons. *Proc. Natl. Acad. Sci.* **98**, 4172–4177 (2001).

176. Mease, R. A., Krieger, P. & Groh, A. Cortical control of adaptation and sensory relay mode in the thalamus. *Proc. Natl. Acad. Sci.* **111**, 6798–6803 (2014).

177. Crandall, S. R., Cruikshank, S. J. & Connors, B. W. A Corticothalamic Switch: Controlling the Thalamus with Dynamic Synapses. *Neuron* **86**, 768–782 (2015).

178. Paz, J. T. *et al.* A new mode of corticothalamic transmission revealed in the Gria4-/- model of absence epilepsy. *Nat. Neurosci.* **14**, 1167–1173 (2011).

179. Kang, J. & Macdonald, R. L. The GABAA Receptor γ2 Subunit R43Q Mutation Linked to Childhood Absence Epilepsy and Febrile Seizures Causes Retention of α1β2γ2S Receptors in the Endoplasmic Reticulum. *J. Neurosci.* **24**, 8672–8677 (2004).

180. Brickley, S. G., Cull-Candy, S. G. & Farrant, M. Single-Channel Properties of Synaptic and Extrasynaptic GABAA Receptors Suggest Differential Targeting of Receptor Subtypes. *J. Neurosci.* **19**, 2960–2973 (1999).

181. Söhl, G., Maxeiner, S. & Willecke, K. Expression and functions of neuronal gap junctions. *Nat. Rev. Neurosci.* **6**, 191–200 (2005).

182. Long, M. A., Landisman, C. E. & Connors, B. W. Small Clusters of Electrically Coupled Neurons Generate Synchronous Rhythms in the Thalamic Reticular Nucleus. *J. Neurosci.* **24**, 341–349 (2004).

183. Gareri, P. *et al.* Antiabsence effects of carbenoxolone in two genetic animal models of absence epilepsy (WAG/Rij rats and lh/lh mice). *Neuropharmacology* **49**, 551–563 (2005).

184. Proulx, É. *et al.* Functional contribution of specific brain areas to absence seizures: role of thalamic gap-junctional coupling. *Eur. J. Neurosci.* **23**, 489–496 (2006).

185. Kohmann, D., Lüttjohann, A., Seidenbecher, T., Coulon, P. & Pape, H.-C. Short-term depression of gap junctional coupling in reticular thalamic neurons of absence epileptic rats. *J. Physiol.* n/a-n/a (2016) doi:10.1113/JP271811.

186. Staley, K. J. & Proctor, W. R. Modulation of mammalian dendritic GABAA receptor function by the kinetics of Cl and HCO3 transport. *J. Physiol.* **519**, 693–712 (1999).

187. Mody, I. Distinguishing Between GABAA Receptors Responsible for Tonic and Phasic Conductances. *Neurochem. Res.* **26**, 907–913 (2001).

188. Pirker, S., Schwarzer, C., Wieselthaler, A., Sieghart, W. & Sperk, G. GABAA receptors:

immunocytochemical distribution of 13 subunits in the adult rat brain. *Neuroscience* **101**, 815–850 (2000).

189. Bazhenov, M., Timofeev, I., Steriade, M. & Sejnowski, T. J. Self–sustained rhythmic activity in the thalamic reticular nucleus mediated by depolarizing GABAA receptor potentials. *Nat. Neurosci.* **2**, 168–174 (1999).

190. Bal, T., von Krosigk, M. & McCormick, D. A. Role of the ferret perigeniculate nucleus in the generation of synchronized oscillations in vitro. *J. Physiol.* **483**, 665–685 (1995).

191. von Krosigk, M., Bal, T. & McCormick, D. A. Cellular mechanisms of a synchronized oscillation in the thalamus. *Science* **261**, 361–364 (1993).

192. Bal, T., von Krosigk, M. & McCormick, D. A. Synaptic and membrane mechanisms underlying synchronized oscillations in the ferret lateral geniculate nucleus in vitro. *J. Physiol.* **483**, 641–663 (1995).

193. Huguenard, J. R. & Prince, D. A. Clonazepam suppresses GABAB-mediated inhibition in thalamic relay neurons through effects in nucleus reticularis. *J. Neurophysiol.* **71**, 2576–2581 (1994).

194. Huntsman, M. M., Porcello, D. M., Homanics, G. E., DeLorey, T. M. & Huguenard, J. R. Reciprocal Inhibitory Connections and Network Synchrony in the Mammalian Thalamus. *Science* **283**, 541–543 (1999).

195. Sohal, V. S. & Huguenard, J. R. Inhibitory Interconnections Control Burst Pattern and Emergent Network Synchrony in Reticular Thalamus. *J. Neurosci.* **23**, 8978–8988 (2003).

196. Sohal, V. S., Keist, R., Rudolph, U. & Huguenard, J. R. Dynamic GABAA Receptor Subtype-Specific Modulation of the Synchrony and Duration of Thalamic Oscillations. *J. Neurosci.* **23**, 3649–3657 (2003).

197. Liu, Z., Vergnes, M., Depaulis, A. & Marescaux, C. Evidence for a critical role of GABAergic transmission within the thalamus in the genesis and control of absence seizures in the rat. *Brain Res.* **545**, 1–7 (1991).

198. Christian, C. A. *et al.* Endogenous Positive Allosteric Modulation of GABAA Receptors by Diazepam binding inhibitor. *Neuron* **78**, 1063–1074 (2013).

199. Christian, C. A. & Huguenard, J. R. Astrocytes potentiate GABAergic transmission in the thalamic reticular nucleus via endozepine signaling. *Proc. Natl. Acad. Sci.* **110**, 20278–20283 (2013).

200. Hornfeldt, C. S. & Larson, A. A. Seizures induced by fluoroacetic acid and fluorocitric acid may involve chelation of divalent cations in the spinal cord. *Eur. J. Pharmacol.* **179**, 307–313 (1990).

201. Jia, F. *et al.* An Extrasynaptic GABAA Receptor Mediates Tonic Inhibition in Thalamic

VB Neurons. *J. Neurophysiol.* **94**, 4491–4501 (2005).

202. Kulik, Á. *et al.* Distinct localization of GABAB receptors relative to synaptic sites in the rat cerebellum and ventrobasal thalamus. *Eur. J. Neurosci.* **15**, 291–307 (2002).

203. Beenhakker, M. P. & Huguenard, J. R. Astrocytes as Gatekeepers of GABAB Receptor Function. *J. Neurosci.* **30**, 15262–15276 (2010).

204. Somogyi, P., Fritschy, J. M., Benke, D., Roberts, J. D. & Sieghart, W. The gamma 2 subunit of the GABAA receptor is concentrated in synaptic junctions containing the alpha 1 and beta 2/3 subunits in hippocampus, cerebellum and globus pallidus. *Neuropharmacology* **35**, 1425–1444 (1996).

205. Rovó, Z. *et al.* Phasic, Nonsynaptic GABA-A Receptor-Mediated Inhibition Entrains Thalamocortical Oscillations. *J. Neurosci.* **34**, 7137–7147 (2014).

206. Nusser, Z., Sieghart, W. & Somogyi, P. Segregation of Different GABAA Receptors to Synaptic and Extrasynaptic Membranes of Cerebellar Granule Cells. *J. Neurosci.* **18**, 1693–1703 (1998).

207. Wei, W., Zhang, N., Peng, Z., Houser, C. R. & Mody, I. Perisynaptic Localization of δ Subunit-Containing GABAA Receptors and Their Activation by GABA Spillover in the Mouse Dentate Gyrus. *J. Neurosci.* **23**, 10650–10661 (2003).

208. Sassoè-Pognetto, M., Panzanelli, P., Sieghart, W. & Fritschy, J.-M. Colocalization of

multiple GABAA receptor subtypes with gephyrin at postsynaptic sites. *J. Comp. Neurol.* **420**, 481–498 (2000).

209. Saxena, N. C. & Macdonald, R. L. Assembly of GABAA receptor subunits: role of the delta subunit. *J. Neurosci.* **14**, 7077–7086 (1994).

210. Benke, D., Michel, C. & Mohler, H. GABAA Receptors Containing the α4-Subunit: Prevalence, Distribution, Pharmacology, and Subunit Architecture In Situ. *J. Neurochem.* **69**, 806–814 (1997).

211. Cope, D. W., Hughes, S. W. & Crunelli, V. GABAA Receptor-Mediated Tonic Inhibition in Thalamic Neurons. *J. Neurosci.* **25**, 11553–11563 (2005).

212. Herd, M. B., Brown, A. R., Lambert, J. J. & Belelli, D. Extrasynaptic GABAA Receptors Couple Presynaptic Activity to Postsynaptic Inhibition in the Somatosensory Thalamus. *J. Neurosci.* **33**, 14850–14868 (2013).

213. Bettler, B., Kaupmann, K., Mosbacher, J. & Gassmann, M. Molecular Structure and Physiological Functions of GABAB Receptors. *Physiol. Rev.* **84**, 835–867 (2004).

214. Fritschy, J.-M. *et al.* GABAB-receptor splice variants GB1a and GB1b in rat brain: developmental regulation, cellular distribution and extrasynaptic localization. *Eur. J. Neurosci.* **11**, 761–768 (1999).

215. Huguenard, J. R. & Prince, D. A. Intrathalamic rhythmicity studied in vitro: nominal

T-current modulation causes robust antioscillatory effects. *J. Neurosci.* **14**, 5485–5502 (1994).

216. Isaacson, J. S., Solis, J. M. & Nicoll, R. A. Local and diffuse synaptic actions of GABA in the hippocampus. *Neuron* **10**, 165–175 (1993).

217. Kim, U., Sanchez-Vives, M. V. & McCormick, D. A. Functional Dynamics of GABAergic Inhibition in the Thalamus. *Science* **278**, 130–134 (1997).

218. Scanziani, M. GABA Spillover Activates Postsynaptic GABAB Receptors to Control Rhythmic Hippocampal Activity. *Neuron* **25**, 673–681 (2000).

219. Sanchez-Vives, M. V. & McCormick, D. A. Functional Properties of Perigeniculate Inhibition of Dorsal Lateral Geniculate Nucleus Thalamocortical Neurons In Vitro. *J. Neurosci.* **17**, 8880–8893 (1997).

220. Beenhakker, M. P. & Huguenard, J. R. Astrocytes as Gatekeepers of GABAB Receptor Function. *J. Neurosci.* **30**, 15262–15276 (2010).

221. Jacobsen, R. B., Ulrich, D. & Huguenard, J. R. GABAB and NMDA Receptors Contribute to Spindle-Like Oscillations in Rat Thalamus In Vitro. *J. Neurophysiol.* **86**, 1365–1375 (2001).

222. Huguenard, J. R. & McCormick, D. A. Thalamic synchrony and dynamic regulation of global forebrain oscillations. *Trends Neurosci.* **30**, 350–356 (2007).

223. Liu, Z., Vergnes, M., Depaulis, A. & Marescaux, C. Involvement of intrathalamic GABAb neurotransmission in the control of absence seizures in the rat. *Neuroscience* **48**, 87–93 (1992).

224. Staak, R. & Pape, H.-C. Contribution of GABAA and GABAB Receptors to Thalamic Neuronal Activity during Spontaneous Absence Seizures in Rats. *J. Neurosci.* **21**, 1378–1384 (2001).

225. Castro-Alamancos, M. A. Neocortical Synchronized Oscillations Induced by Thalamic Disinhibition In Vivo. *J. Neurosci.* **19**, RC27–RC27 (1999).

226. Zhou, Y. & Danbolt, N. C. GABA and Glutamate Transporters in Brain. *Front. Endocrinol.* **4**, (2013).

227. De Biasi, S., Vitellaro-Zuccarello, L. & Brecha, N. C. Immunoreactivity for the GABA transporter-1 and GABA transporter-3 is restricted to astrocytes in the rat thalamus. A light and electron-microscopic immunolocalization. *Neuroscience* **83**, 815–828 (1998).

228. Vinton, A. *et al.* Tiagabine-induced generalised non convulsive status epilepticus in patients with lesional focal epilepsy. *J. Clin. Neurosci.* **12**, 128–133 (2005).

229. Ettinger, A. B. *et al.* Two Cases of Nonconvulsive Status Epilepticus in Association with Tiagabine Therapy. *Epilepsia* **40**, 1159–1162 (1999).

230. Karyakin, V. B., Vasil'ev, D. S., Zhuravin, I. A., Zaitsev, A. V. & Magazanik, L. G. Early

morphological and functional changes in the GABAergic system of hippocampus in the rat lithium-pilocarpine model of epilepsy. *Dokl. Biol. Sci. Proc. Acad. Sci. USSR Biol. Sci. Sect.* **472**, 4–7 (2017).

231. Coenen, A. M. L., Blezer, E. H. M. & van Luijtelaar, E. L. J. M. Effects of the GABA-uptake inhibitor tiagabine on electroencephalogram, spike-wave discharges and behaviour of rats. *Epilepsy Res.* **21**, 89–94 (1995).

232. Bryant, A. S., Li, B., Beenhakker, M. P. & Huguenard, J. R. Maintenance of Thalamic Epileptiform Activity Depends on the Astrocytic Glutamate-Glutamine Cycle. *J. Neurophysiol.* **102**, 2880–2888 (2009).

233. De Gennaro, L. & Ferrara, M. Sleep spindles: an overview. *Sleep Med. Rev.* **7**, 423–440 (2003).

234. Morison, R. S. & Bassett, D. L. Electrical Activity of the Thalamus and Basal Ganglia in Decorticate Cats. *J. Neurophysiol.* **8**, 309–314 (1945).

235. Contreras, D., Destexhe, A., Sejnowski, T. J. & Steriade, M. Control of Spatiotemporal Coherence of a Thalamic Oscillation by Corticothalamic Feedback. *Science* **274**, 771–774 (1996).

236. Andersson, S. A. & Manson, J. R. Rhythmic activity in the thalamus of the unanaesthetized decorticate cat. *Electroencephalogr. Clin. Neurophysiol.* **31**, 21–34 (1971).

237. Andersen, P., Andersson, S. A. & Lømo, T. Some factors involved in the thalamic control of spontaneous barbiturate spindles. *J. Physiol.* **192**, 257–281 (1967).

238. Steriade, M., Deschenes, M., Domich, L. & Mulle, C. Abolition of spindle oscillations in thalamic neurons disconnected from nucleus reticularis thalami. *J. Neurophysiol.* **54**, 1473–1497 (1985).

239. Halassa, M. M. *et al.* Selective optical drive of thalamic reticular nucleus generates thalamic bursts and cortical spindles. *Nat. Neurosci.* **14**, 1118–1120 (2011).

240. Warren, R. A., Agmon, A. & Jones, E. G. Oscillatory synaptic interactions between ventroposterior and reticular neurons in mouse thalamus in vitro. *J. Neurophysiol.* **72**, 1993–2003 (1994).

241. Kim, U., Bal, T. & McCormick, D. A. Spindle waves are propagating synchronized oscillations in the ferret LGNd in vitro. *J. Neurophysiol.* **74**, 1301–1323 (1995).

242. Contreras, D. & Steriade, M. Spindle oscillation in cats: the role of corticothalamic feedback in a thalamically generated rhythm. *J. Physiol.* **490**, 159–179 (1996).

243. Contreras, D., Destexhe, A., Sejnowski, T. J. & Steriade, M. Spatiotemporal Patterns of Spindle Oscillations in Cortex and Thalamus. *J. Neurosci.* **17**, 1179–1196 (1997).

244. Nir, Y. *et al.* Regional Slow Waves and Spindles in Human Sleep. *Neuron* **70**, 153–169 (2011).

245. Sarkisova, K. & van Luijtelaar, G. The WAG/Rij strain: A genetic animal model of absence epilepsy with comorbidity of depressiony. *Prog. Neuropsychopharmacol. Biol. Psychiatry* **35**, 854–876 (2011).

246. Leal, A. *et al.* Dynamics of epileptic activity in a peculiar case of childhood absence epilepsy and correlation with thalamic levels of GABA. *Epilepsy Behav. Case Rep.* **5**, 57–65 (2016).

247. Huguenard, J. R. & McCormick, D. A. Simulation of the currents involved in rhythmic oscillations in thalamic relay neurons. *J. Neurophysiol.* **68**, 1373–1383 (1992).

248. Coulter, D. A., Huguenard, J. R. & Prince, D. A. Calcium currents in rat thalamocortical relay neurones: kinetic properties of the transient, low-threshold current. *J. Physiol.* **414**, 587–604 (1989).

249. Santoro, B. & Tibbs, G. R. The HCN Gene Family: Molecular Basis of the Hyperpolarization-Activated Pacemaker Channels. *Ann. N. Y. Acad. Sci.* **868**, 741–764 (1999).

250. Amarillo, Y., Zagha, E., Mato, G., Rudy, B. & Nadal, M. S. The interplay of seven subthreshold conductances controls the resting membrane potential and the oscillatory behavior of thalamocortical neurons. *J. Neurophysiol.* **112**, 393–410 (2014).

251. Ulrich, D. & Huguenard, J. R. GABAB receptor-mediated responses in GABAergic projection neurones of rat nucleus reticularis thalami in vitro. *J. Physiol.* **493**, 845–854

(1996).

252. Destexhe, A. & Sejnowski, T. J. G protein activation kinetics and spillover of gamma-aminobutyric acid may account for differences between inhibitory responses in the hippocampus and thalamus. *Proc. Natl. Acad. Sci.* **92**, 9515–9519 (1995).

253. Destexhe, A., Contreras, D., Steriade, M., Sejnowski, T. J. & Huguenard, J. R. In vivo, in vitro, and computational analysis of dendritic calcium currents in thalamic reticular neurons. *J. Neurosci.* **16**, 169–185 (1996).

254. Destexhe, A., Neubig, M., Ulrich, D. & Huguenard, J. Dendritic Low-Threshold Calcium Currents in Thalamic Relay Cells. *J. Neurosci.* **18**, 3574–3588 (1998).

255. Munsch, T., Budde, T. & Pape, H.-C. Voltage-activated intracellular calcium transients in thalamic relay cells and interneurons. *NeuroReport* **8**, 2411–2418 (1997).

256. Zhou, Q., Godwin, D. W., O'Malley, D. M. & Adams, P. R. Visualization of Calcium Influx Through Channels That Shape the Burst and Tonic Firing Modes of Thalamic Relay Cells. *J. Neurophysiol.* **77**, 2816–2825 (1997).

257. Williams, S. R. & Stuart, G. J. Action Potential Backpropagation and Somato-dendritic Distribution of Ion Channels in Thalamocortical Neurons. *J. Neurosci.* **20**, 1307–1317 (2000).

258. Golomb, D., Wang, X. J. & Rinzel, J. Propagation of spindle waves in a thalamic slice

model. *J. Neurophysiol.* **75**, 750–769 (1996).

259. Sohal, V. S., Huntsman, M. M. & Huguenard, J. R. Reciprocal Inhibitory Connections Regulate the Spatiotemporal Properties of Intrathalamic Oscillations. *J. Neurosci.* **20**, 1735–1745 (2000).

260. Destexhe, A., Contreras, D. & Steriade, M. Mechanisms Underlying the Synchronizing Action of Corticothalamic Feedback Through Inhibition of Thalamic Relay Cells. *J. Neurophysiol.* **79**, 999–1016 (1998).

261. Destexhe, A. Spike-and-Wave Oscillations Based on the Properties of GABAB Receptors. *J. Neurosci.* **18**, 9099–9111 (1998).

262. Jahnsen, H. & Llinás, R. Electrophysiological properties of guinea-pig thalamic neurones: an in vitro study. *J. Physiol.* **349**, 205–226 (1984).

263. Gutierrez, C., Cox, C. L., Rinzel, J. & Sherman, S. M. Dynamics of Low-Threshold Spike Activation in Relay Neurons of the Cat Lateral Geniculate Nucleus. *J. Neurosci.* **21**, 1022–1032 (2001).

264. Getting, P. A. Emerging Principles Governing the Operation of Neural Networks. *Annu. Rev. Neurosci.* **12**, 185–204 (1989).

265. Marder, E. & Calabrese, R. L. Principles of rhythmic motor pattern generation. *Physiol. Rev.* **76**, 687–717 (1996).

266. Nusbaum, M. P. & Beenhakker, M. P. A small-systems approach to motor pattern generation. *Nature* **417**, 343–350 (2002).

267. Huguenard, J. R. & McCormick, D. A. Thalamic synchrony and dynamic regulation of global forebrain oscillations. *Trends Neurosci* **30**, 350–356 (2007).

268. David A McCormick & Diego Contreras. On The Cellular and Network Bases of Epileptic Seizures. *Annu. Rev. Physiol.* **63**, 815–846 (2001).

269. Kim, D. *et al.* Thalamic Control of Visceral Nociception Mediated by T-Type Ca2+ Channels. *Science* **302**, 117–119 (2003).

270. Shosaku, A. A comparison of receptive field properties of vibrissa neurons between the rat thalamic reticular and ventro-basal nuclei. *Brain Res.* **347**, 36–40 (1985).

271. Vergnes, M., Boehrer, A., Simler, S., Bernasconi, R. & Marescaux, C. Opposite effects of GABAB receptor antagonists on absences and convulsive seizures. *Eur. J. Pharmacol.* **332**, 245–255 (1997).

272. Bortolato, M. *et al.* GABAB receptor activation exacerbates spontaneous spike-and-wave discharges in DBA/2J mice. *Seizure* **19**, 226–231 (2010).

273. Blumenfeld, H. & McCormick, D. A. Corticothalamic Inputs Control the Pattern of Activity Generated in Thalamocortical Networks. *J. Neurosci.* **20**, 5153–5162 (2000).

274. Kleiman-Weiner, M., Beenhakker, M. P., Segal, W. A. & Huguenard, J. R. Synergistic

roles of GABAA receptors and SK channels in regulating thalamocortical oscillations. *J. Neurophysiol.* **102**, 203–213 (2009).

275. Sitte, H. H., Singer, E. A. & Scholze, P. Bi-directional transport of GABA in human embryonic kidney (HEK-293) cells stably expressing the rat GABA transporter GAT-1. *Br. J. Pharmacol.* **135**, 93–102 (2002).

276. Borden, L. A. *et al.* Cloning of the human homologue of the GABA transporter GAT-3 and identification of a novel inhibitor with selectivity for this site. *Receptors Channels* **2**, 207–213 (1994).

277. Knake, S., Hamer, H. M., Schomburg, U., Oertel, W. H. & Rosenow, F. Tiagabine-induced absence status in idiopathic generalized epilepsy. *Seizure* **8**, 314–317 (1999).

278. Sharp, A. A., O'Neil, M. B., Abbott, L. F. & Marder, E. Dynamic clamp: computer-generated conductances in real neurons. *J. Neurophysiol.* **69**, 992–995 (1993).

279. Ulrich, D. & Huguenard, J. R. γ-Aminobutyric acid type B receptor-dependent burst-firing in thalamic neurons: A dynamic clamp study. *Proc. Natl. Acad. Sci.* **93**, 13245–13249 (1996).

280. Johnston, D. & Wu, S. M. *Foundations of Cellular Neurophysiology*. (MIT press, 1994).

281. Rall, W. Electrophysiology of a Dendritic Neuron Model. *Biophys. J.* **2**, 145–167

(1962).

282. Pape, H. C., Budde, T., Mager, R. & Kisvárday, Z. F. Prevention of Ca(2+)-mediated action potentials in GABAergic local circuit neurones of rat thalamus by a transient K+ current. *J. Physiol.* **478**, 403–422 (1994).

283. Hodgkin, A. L. & Huxley, A. F. A quantitative description of membrane current and its application to conduction and excitation in nerve. *J. Physiol.* **117**, 500–544 (1952).

284. Klein, P. M. *et al.* Tenuous Inhibitory GABAergic Signaling in the Reticular Thalamus. *J. Neurosci. Off. J. Soc. Neurosci.* **38**, 1232–1248 (2018).

285. McCafferty, C. *et al.* Cortical drive and thalamic feed-forward inhibition control thalamic output synchrony during absence seizures. *Nat. Neurosci.* **21**, 744 (2018).

286. Sorokin, J. M. *et al.* Bidirectional Control of Generalized Epilepsy Networks via Rapid Real-Time Switching of Firing Mode. *Neuron* **93**, 194–210 (2017).

287. Huguenard, J. Current Controversy: Spikes, Bursts, and Synchrony in Generalized Absence Epilepsy: Unresolved Questions Regarding Thalamocortical Synchrony in Absence Epilepsy. *EPI Epilepsy Curr.* **19**, 105–111 (2019).

288. Charpier, S. *et al.* On the putative contribution of GABAB receptors to the electrical events occuring during spontaneous spike and wave discharges. *Neuropharmacology* **38**, 1699–1706 (1999).

289. Pape, H.-C. & McCormick, D. A. Electrophysiological and pharmacological properties of interneurons in the cat dorsal lateral geniculate nucleus. *Neuroscience* **68**, 1105–1125 (1995).

290. Nielsen, E. B. *et al.* Characterization of tiagabine (NO-328), a new potent and selective GABA uptake inhibitor. *Eur. J. Pharmacol.* **196**, 257–266 (1991).

291. Uthman, B. M. *et al.* Tiagabine for Complex Partial Seizures: A Randomized, Add-on, Dose-Response Trial. *Arch. Neurol.* **55**, 56–62 (1998).

292. Ting, J. T., Daigle, T. L., Chen, Q. & Feng, G. Acute Brain Slice Methods for Adult and Aging Animals: Application of Targeted Patch Clamp Analysis and Optogenetics. in *Patch-Clamp Methods and Protocols* (eds. Martina, M. & Taverna, S.) 221–242 (Springer New York, 2014). doi:10.1007/978-1-4939-1096-0_14.

293. Sohal, V. S., Pangratz-Fuehrer, S., Rudolph, U. & Huguenard, J. R. Intrinsic and Synaptic Dynamics Interact to Generate Emergent Patterns of Rhythmic Bursting in Thalamocortical Neurons. *J. Neurosci.* **26**, 4247–4255 (2006).

294. Otis, T. S., De Koninck, Y. & Mody, I. Characterization of synaptically elicited GABAB responses using patch-clamp recordings in rat hippocampal slices. *J. Physiol.* **463**, 391–407 (1993).

295. Chung, S., Li, X. & Nelson, S. B. Short-Term Depression at Thalamocortical Synapses

Contributes to Rapid Adaptation of Cortical Sensory Responses In Vivo. *Neuron* **34**, 437–446 (2002).

296. Carnevale, N. T. & Hines, M. L. *The NEURON Book*. (Cambridge University Press, 2009).

297. Druckmann, S. *et al.* A novel multiple objective optimization framework for constraining conductance-based neuron models by experimental data. *Front. Neurosci.* **1**, (2007).

298. Lagarias, J. C., Reeds, J. A., Wright, M. H. & Wright, P. E. Convergence Properties of the Nelder--Mead Simplex Method in Low Dimensions. *SIAM J. Optim.* **9**, 112–147 (1998).

299. Wendling, F., Benquet, P., Bartolomei, F. & Jirsa, V. Computational models of epileptiform activity. *J. Neurosci. Methods* **260**, 233–251 (2016).

300. Destexhe, A. Chapter 2 - Network Models of Absence Seizures. in *Neuronal Networks in Brain Function, CNS Disorders, and Therapeutics* (eds. Faingold, C. L. & Blumenfeld, H.) 11–35 (Academic Press, 2014). doi:10.1016/B978-0-12-415804-7.00002-2.

301. Sohal, V. S. & Huguenard, J. R. Long-Range Connections Synchronize Rather Than

Spread Intrathalamic Oscillations: Computational Modeling and In Vitro Electrophysiology. *J. Neurophysiol.* **80**, 1736–1751 (1998).

302. Voelkl, B. *et al.* Reproducibility of animal research in light of biological variation. *Nat. Rev. Neurosci.* **21**, 384–393 (2020).

303. Truccolo, W. *et al.* Neuronal Ensemble Synchrony during Human Focal Seizures. *J. Neurosci.* **34**, 9927–9944 (2014).

304. Drinkenburg, W. H. I. M., van Luijtelaar, E. L. J. M., van Schaijk, W. J. & Coenen, A. M. L. Aberrant transients in the EEG of epileptic rats: A spectral analytical approach. *Physiol. Behav.* **54**, 779–783 (1993).

305. Tangwiriyasakul, C. *et al.* Dynamic brain network states in human generalized spike-wave discharges. *Brain J. Neurol.* **141**, 2981–2994 (2018).

306. Grasse, D. W., Karunakaran, S. & Moxon, K. A. Neuronal synchrony and the transition to spontaneous seizures. *Exp. Neurol.* **248**, 72–84 (2013).

307. Liu, H. & Zhang, P. Phase Synchronization Dynamics of Neural Network during Seizures. *Computational and Mathematical Methods in Medicine* https://www.hindawi.com/journals/cmmm/2018/1354915/ (2018) doi:10.1155/2018/1354915.

308. Fries, P., Roelfsema, P. R., Engel, A. K., König, P. & Singer, W. Synchronization of oscillatory responses in visual cortex correlates with perception in interocular rivalry. *Proc. Natl. Acad. Sci.* **94**, 12699–12704 (1997).

309. Grasse, D. W. & Moxon, K. A. Correcting the Bias of Spike Field Coherence Estimators Due to a Finite Number of Spikes. *J. Neurophysiol.* **104**, 548–558 (2010).

310. Kuzum, D. *et al.* Transparent and flexible low noise graphene electrodes for simultaneous electrophysiology and neuroimaging. *Nat. Commun.* **5**, 1–10 (2014).

311. Liu, J. & Baraban, S. C. Network Properties Revealed during Multi-Scale Calcium Imaging of Seizure Activity in Zebrafish. *eNeuro* **6**, (2019).

312. Lu, A. C. & Beenhakker, M. Casting a Wide Net to Catch Seizures: *Epilepsy Curr.* (2019) doi:10.1177/1535759719854757.

313. Lüttjohann, A., Schoffelen, J.-M. & van Luijtelaar, G. Termination of ongoing spike-wave discharges investigated by cortico–thalamic network analyses. *Neurobiol. Dis.* **70**, 127–137 (2014).

314. Jiang, W. *et al.* Dynamic Neuromagnetic Network Changes of Seizure Termination in Absence Epilepsy: A Magnetoencephalography Study. *Front. Neurol.* **10**, 703 (2019).

315. Lüttjohann, A. & Pape, H.-C. Regional specificity of cortico-thalamic coupling strength and directionality during waxing and waning of spike and wave discharges.

Sci. Rep. **9**, 1–11 (2019).

316. Bonjean, M. *et al.* Corticothalamic Feedback Controls Sleep Spindle Duration In Vivo. *J. Neurosci.* **31**, 9124–9134 (2011).

317. Zhang, S. J., Huguenard, J. R. & Prince, D. A. GABAA Receptor-Mediated Cl Currents in Rat Thalamic Reticular and Relay Neurons. *J. Neurophysiol.* **78**, 2280–2286 (1997).

318. Barthó, P. *et al.* Ongoing Network State Controls the Length of Sleep Spindles via Inhibitory Activity. *Neuron* **82**, 1367–1379 (2014).

319. Kros, L. *et al.* Cerebellar output controls generalized spike-and-wave discharge occurrence. *Ann. Neurol.* **77**, 1027–1049 (2015).